



## **Deliverable 2.8:**

# **First results on the thermodynamic databases and reactive transport models for steel-cement interfaces at high temperature**

Work Package 2

The project leading to this application has received funding from the European Union's Horizon 2020 research and innovation programme under grant agreement No 847593.



## Document information

Project Acronym	<b>EURAD</b>
Project Title	<b>European Joint Programme on Radioactive Waste Management</b>
Project Type	<b>European Joint Programme (EJP)</b>
EC grant agreement No.	<b>847593</b>
Project starting / end date	<b>1<sup>st</sup> June 2019 – 30 May 2024</b>
Work Package No.	<b>2</b>
Work Package Title	<b><u>A</u>ssessment of <u>C</u>hemical <u>E</u>volution of ILW and HLW <u>D</u>isposal Cells</b>
Work Package Acronym	<b>ACED</b>
Deliverable No.	<b>D2.8</b>
Deliverable Title	<b>First results on the thermodynamic databases and reactive transport models for steel-cement interfaces at high temperature</b>
Lead Beneficiary	<b>IRSN</b>
Contractual Delivery Date	<b>August 2020</b>
Actual Delivery Date	<b>February 2020</b>
Type	<b>Report</b>
Dissemination level	<b>PU</b>
Authors	<b>Laurent De Windt (MINES ParisTech), George Dan Miron (PSI), Margit Fabian (MTA), Jules Goethals (Subatech, IMT Atlantique), Charles Wittebroodt (IRSN)</b>

### To be cited as:

De Windt L., Miron G. D., Fabian M., Goethals, J., Wittebroodt C. (2020): First results on the thermodynamic databases and reactive transport models for steel-cement interfaces at high temperature. Final version as of xx.xx.xxxx of deliverable D2.8 of the HORIZON 2020 project EURAD. EC Grant agreement no: 847593.

### Disclaimer

All information in this document is provided "as is" and no guarantee or warranty is given that the information is fit for any particular purpose. The user, therefore, uses the information at its sole risk and liability. For the avoidance of all doubts, the European Commission has no liability in respect of this document, which is merely representing the authors' view.

### Acknowledgement

This document is a deliverable of the European Joint Programme on Radioactive Waste Management (EURAD). EURAD has received funding from the European Union's Horizon 2020 research and innovation programme under grant agreement No 847593.

Status of deliverable		
	By	Date
Delivered (Lead Beneficiary)	Laurent De Windt (MINES Paris Tech) Dan Miron (PSI)	06/07/2020
Verified (WP Leader)	Diederik Jacques (SCK CEN)	26/07/2020
Reviewed (Reviewers)	SCK CEN	27/09/2020
Verified (PMO)	Bernd Grambow (IMT Atlantique)	08/11/2020
Approved (PMO)	Bernd Grambow (IMT Atlantique)	18/02/2021
Submitted to EC (Coordinator)	Andra	18/02/2021

## Executive Summary

The interface between carbon steel and cementitious materials is a key issue in the concepts of disposal cell for vitrified high-level waste (HLW) in argillaceous sedimentary formations for the Belgium, Dutch and French national programs. The first two programs rely upon supercontainers containing the HLW encased in prefabricated cylindrical concrete buffer material. The concrete is made from CEM I cement and limestone aggregates. The pH has to be kept at high values during the thermal phase, and much longer beyond, in order to keep the carbon steel overpack passivated, to limit corrosion and ultimately radionuclide release. In the French concept, the annular gap between a carbon steel sleeve and the host rock is filled with a bentonite/cement grout that imposes corrosion-limiting environmental condition during the thermal phase only. The alkalinity of the grout is moderate (pH ~ 11) and should have been neutralized readily afterwards to prevent the dissolution of the nuclear glass and radionuclide release under alkaline pH values. The different national concepts of disposal cell for intermediate level waste (ILW) present a wider diversity of configurations and materials compared to the HLW disposal concepts. However, in most concepts carbon steel is used for the containers of the ILW packages that are the immobilized in a concrete or steel container with a cement-based material.

The subtask 2.2 of the ACED WP is dedicated to identify and model the main reactive processes at the cement/steel interface and their consequences in terms of transfers and microstructures evolutions. All data (from modelling and experiments) have to describe geochemical behaviors in function to the environmental constraints, representative of conditions planned to be encountered in geological facilities.

The thermodynamics of Fe-containing cement phases represents the first main input of this report, based on a broad bibliographical review and first results. A second major issue is to investigate the kinetics of the steel/cement interactions in the geologic disposal, from a literature review and first results obtained in the BACUCE project. A last and third objective is to gather the chemical and physical properties of all the materials considered in Task 2.2 and to model their initial states.

The first part provides an overview on the thermodynamics of Fe-containing cement phases, corrosion products, and iron pore solution speciation. The use of non-ideal solid-solutions to model some of the cement hydrate phases is detailed, together with preliminary results on the iron uptake in C-S-H. These are essential for assessing the fate of iron that results from corrosion and serve as inputs and constraints for improving the reactive transport modelling at the interface and waste package level. CEMDATA18 database for cement phases was improved from Cemdata07 mainly with the extension of aluminum and iron containing phases as well as the changes in the C-S-H models concerning the volume and the alkali uptake. These changes can lead to considerably different modeling results between the two database versions. Thermodynam database contains data for modelling cement phases, iron corrosion products such as iron carbonates, oxyhydroxides, silicates and sulfides, these can be supplemented with data for iron corrosion products or clayey phases can be selected from ThermoChimie.

Fe-siliceous hydrogarnet is the most stable iron bearing cement hydrate phase from ambient to elevated temperatures. This is replaced by ferrihydrite in low pH cements. Generally, Fe(III)-bearing cement phases, Fe oxides and hydroxides have low solubility. Their stability increases with temperature increasing and this keeps the iron present in the pore solution at low concentrations. This and the uptake of iron in C-S-H, a main cement phase, will result in the retention of iron near the cement/metal interface. The most stable corrosion products in highly alkaline conditions (pH>11), maintained by the cement system, is magnetite and goethite under anoxic and oxic conditions, respectively. The formation of the stable iron oxides/hydroxides can be inhibited, depending on kinetics, temperature and local composition, resulting in the formation of different intermediate metastable phases such as amorphous oxide/hydroxide phases, hydroxychloride phases, green rust GR1(Cl<sup>-</sup>). These phases are more soluble, and their presence will enhance the mobility of iron. Because of the high pH, iron in the pore solution will be in its hydrolyzed form. The presence of chloride ions and other ligands could lead to an increased amount of dissolved iron and the stabilization soluble iron phases for instance green rust GR1(Cl<sup>-</sup>).

Some of the Fe containing cement phases like the (Al, Fe)-monosulfate and (Al, Fe)-ettringite are modeled as non-ideal solid solutions. For simplification in reactive transport codes, they can be treated ideal solid solutions. This simplification should produce results for the solid and aqueous composition within the experimental uncertainty and will be further investigated. In the case of C-S-H, a non-ideal mixing model is necessary to accurately describe the experimental data on the uptake of iron and other elements. Preliminary results show that the model can be successfully parameterized against experimental data for iron uptake in C-S-H. After additional estimates necessary for the iron in aluminum bearing C-S-H, the model will be used to investigate the impact on the iron at the cement/steel interface. For codes that do not use complex solid solution models, we investigate the possibility of using a smart discretization procedure, for producing the optimal number of discrete phases that satisfactorily approximate the non-ideal solid solution model.

In terms of material composition, low carbon or weakly alloyed steels are mostly made of metallic iron. They are never in equilibrium with water even under anoxic conditions and will be subjected to several types of corrosion processes, such as generalized (uniform) corrosion or localized corrosion (e.g. pitting corrosion). The present report will focus on the generalized corrosion of iron under anoxic and fully water saturated conditions: The effect of temperature, of water chemistry and pH (from neutral pH to highly alkaline pH) and of the configuration (steel in contact with aqueous solutions vs. close contact between solid materials). At 80°C and neutral pH in argillaceous media, the corrosion rate ranges from a few  $\mu\text{m}/\text{y}$  in synthetic clayey solution up to 30  $\mu\text{m}/\text{y}$  when steel is embedded in the argillaceous rock. The corrosion decreases exponentially with time over one year approximately. Layered zonation of corrosion products (oxyhydroxide, chukanovite and siderite, iron silicates) generally takes place in an embedded configuration. At 80°C and high-pH conditions, the long-term corrosion rates (beyond one year) is 0.1  $\mu\text{m}/\text{y}$  or lower due to passivation by the formation of compact magnetite film or layer uniformly over the whole surface of iron. The passivation of the steel by magnetite may become inactive when the alkaline pH decreases below 10.5. However, the corrosion rates under moderately alkaline pH (10.5 – 11.5) are not well characterized yet, and will be a major input of the Subtask 2.2. The very few papers indicate that corrosion rates one order of magnitude higher than in classical cement environment. The activation energy is commonly low for all the pH range and temperature increase slightly enhance corrosion in most cases.

The modeling of experiments in the Subtask 2.2 will be performed with reactive transport modeling (RTM), in particular HYTEC. The main mathematical features of RTM are presented with as special emphasis on temperature dependency for thermodynamics as well as kinetics and diffusion (Arrhenius-type laws). The possibility of chemical feedback on porosity and diffusion could be important for modeling the time evolution of the steel/ cement interface. HYTEC is interfaced with the Thermodem database and will benefit from the development of the thermodynamics of iron-cement phase performed in Subtask 2.2. The kinetics of the formation of the corrosion products is also introduced in the report.

The BACUCE experiments are taking place in the IRSN underground research laboratory located in an argillaceous formation of Toarcian argillite at Tournemire (France). The in-situ experimental set-up aims to characterize the interface between carbon steel and two cementitious buffers (a bentonite/cement grout and a CEM I paste) until three years of interaction at the ambient temperature of 15°C and at 80°C with a heating system. One specificity is to study the influence of imperfect contacts or voids that are filled with grout porewater solution mixed with the argillite one. Experiments at the laboratory are also conducted in support of the in situ experiments at 20°C. The first lab experiment concerns the porewater chemistry of the bentonite/cement grout. The second experiment assesses of the efficiency of the slightly alkaline conditions to protect the steel against corrosion. Complementary experiments at 80°C are under progress in Subtask 2.2. The third lab experiments are planned to assess the effect of mill scale on the corrosion rate of low carbon steel in similar conditions as the BACUCE experiments. These experiments will also allow to evaluate the synthetic porewater evolution in contact with the two buffer materials (CEM I/MREA) at 80°C, as well as the cement and steel corrosion products evolution.

The geochemical, mineralogical and transport parameters of all materials (CEM I paste, grout, argillite) have been compiled and adapted as HYTEC input files. The initial chemistry and mineral assembly have

been modeled, first at ambient temperature, and after a temperature increase up to 80°C. In hydrated CEM I cement pastes, temperature affects the balance between AFT/AFm phases, decreases pH (but the hydroxide content remains high) and rises the sulfate dissolved concentration. Compared to CEM I, the bentonite/cement grout is still poorly known. Modeling has been done on batch tests with hydrated grout and water at 20°C. The model has then been extrapolated to the porewater and mineralogy of the hydrated grout at 20°C and 80°C. Two sets of thermodynamic data have been tested, improving the description of the C-A-S-H phases. The implementation of a kinetic approach for the hydrations of slag and silica fume, especially at 20°C, will be done as an improvement of this preliminary model. Eventually, the modeling of steel corrosion is on-going (corrosion products and intrinsic rate constant).

An alternative set of lab experiments are also in progress in Subtask 2.2 to gain information on corrosion intensity at the interfaces between carbon steel and a CEM II/B -based concrete. A temperature of 80°C is also considered for the sake of consistency and comparison with the other experiments of Subtask 2.2. Synthetic groundwater of the Boda claystone is used for hydrating the cement and as boundary conditions. The physical and chemical properties of the concrete and the Boda water chemistry have been compiled to further define the initial states of the reactive transport model.

The report ends with a series of planned continuations and improvements. Subtask 2.2 will also pass information from its relatively isolated small-scale processes investigated on interface scale to more complex systems at waste package scale (task 3) and disposal scale (task 4).

## Table of content

Executive Summary.....	4
Table of content.....	7
List of figures .....	9
List of Tables .....	11
1. Introduction and context .....	12
1.1 Context, steel/cement interface in HLW and ILW disposal cells .....	12
1.2 Aims and structure of this deliverable .....	14
2. Thermodynamics of Fe-containing cement phases.....	16
2.1 Thermodynamic database evolutions for cement phases .....	16
2.1.1 CEMDATA18 database .....	16
2.1.2 PSI/Nagra database .....	17
2.1.3 Other databases (Thermoddem and Thermochimie) .....	18
2.2 Fe-containing phases and pore solution .....	18
2.2.1 Fe-containing cement phases .....	18
2.2.2 Fe-corrosion products.....	21
2.2.3 Fe speciation in cement pore solution .....	23
2.3 Non-ideal solid solution model.....	23
2.3.1 Multisite solid-solution model for cation uptake in C-S-H.....	23
2.3.2 Fe containing AFm (monosulfate) and AFt (trisulfate) solid solutions .....	25
2.3.3 Discretization of Fe solid solution data for reactive transport model.....	26
2.4 First results and discussion .....	27
2.4.1 Parameterization of Fe uptake in C-S-H.....	27
3. Literature data on the kinetic rates of steel corrosion.....	30
3.1 Main (electro)chemical processes .....	30
3.2 Fe-corrosion rate laws in neutral pH argillaceous media .....	30
3.3 Fe-corrosion rate laws under high-pH alkaline conditions .....	33
3.4 Fe-corrosion rate laws under low-pH alkaline conditions.....	35
3.5 Mill-scale effect on steel corrosion rate .....	36
4. Mathematical modeling and HYTEC code .....	37
4.1 Reactive transport equation.....	37
4.2 Thermodynamic equilibrium .....	38
4.2.1 The mass balance equation .....	38
4.2.2 Sorption by ion exchange and surface complexation.....	38
4.3 Kinetics controlled on solid phase reactivity.....	39

4.3.1	General chemical kinetic law .....	39
4.3.2	Application to metallic iron corrosion .....	40
4.4	Temperature dependencies.....	41
5.	In situ cement/steel interactions – BACUCE experiments .....	43
5.1	Set-up of the BACUCE experiments .....	43
5.1.1	In-situ tests on steel corrosion at 15°C and 80°C.....	43
5.1.2	Lab experiments on steel corrosion in grout water at 25°C .....	44
5.1.3	Lab experiment on the mill-scale effect on steel corrosion at 80°C .....	45
5.2	Properties and modeling of the hydrated CEM I paste.....	46
5.2.1	Bulk and mineralogical composition .....	46
5.2.2	Porewater chemistry .....	47
5.2.3	Porosity and diffusion properties .....	47
5.3	Properties and modeling of the bentonite/cement grout.....	49
5.3.1	Bulk and mineralogical composition .....	49
5.3.2	Modeling of hydrated grout/water batch tests .....	50
5.3.3	Modeling of the initial state of the hydrated bentonite/cement grout.....	53
5.3.4	Porosity and diffusion properties .....	53
5.4	Properties of the Toarcian argillite.....	54
5.4.1	Mineralogical composition .....	54
5.4.2	Cationic exchange and porewater chemistry .....	54
5.4.3	Porosity and diffusion properties .....	54
5.5	Synthetic porewaters for the experiments .....	55
6.	Lab experiment on steel/CEM IIB interactions .....	59
6.1	Experimental set-up.....	59
6.2	Properties of the CEM II/B concrete .....	59
6.3	Low-carbon steel .....	60
6.4	Synthetic Boda claystone porewater .....	60
7.	Conclusion and Way forward.....	62
7.1	Main conclusion .....	62
7.2	Planned continuation, improvements .....	63
7.3	Missing data or process.....	63
7.4	Information for Tasks 3 and 4.....	64
	References .....	65

## List of figures

Figure 1 – Cross-section of the HLW disposal cell in a clay host rock for the Belgian/Dutch supercontainer concept (top, Craeye et al. (2009) and the French sleeve concept (bottom, Andra, 2016a).....	13
Figure 2 – Representative ILW disposal cell (ACED work package). .....	14
Figure 3 – Volume of cement phases in equilibrium, per 100 g of completely hydrated CEM-I as a function of temperature (A), addition of Fe <sub>2</sub> O <sub>3</sub> (C) and of Fe <sub>3</sub> O <sub>4</sub> (D). Elemental concentration in the aqueous pore solution (B). Calculations done in GEM-Selektor using the CEMDATA18 database using the CEM I 52.5 N – Val d’Azergues composition (w/c 0.42). The CASHNK+ solid solution model used here does not yet contain the iron uptake. ....	20
Figure 4 – Uptake on Fe in C-S-H at different C/S ratios in C-S-H and pH values. Circles, experimental data from Mancini et al. (2020a) and lines, calculated values using the optimized properties of endmembers and values for the interaction parameters. ....	29
Figure 5 – Evolution of average generalized corrosion rate of carbon steels as a function of time in fairly reducing conditions in different types of clayey water chemistry at 80°C (Féron et al., 2008). ....	31
Figure 6 – Layered zonation of corrosion products around a metallic iron rod embedded in the Toarcian argillite of Tournemire after 400 days at 60°C (Chautard et al., 2013). ....	32
Figure 7 – Speciation of iron corrosion products calculated with the Thermoddem database at 60°C for (a) iron oxyhydroxides and carbonates and (b) iron oxyhydroxides and sulfides; Fe conc. = 10 <sup>-5</sup> M, act. HCO <sub>3</sub> <sup>-</sup> = 10 <sup>-3</sup> , SO <sub>4</sub> conc. = 10 <sup>-4</sup> M, excluding hematite; the dotted lines correspond to the stability limits of water. ....	32
Figure 8 – Effect of temperature on the initial anaerobic corrosion rate of carbon steel in various alkaline (basic) solutions. The anaerobic corrosion rate is plotted as a function of reciprocal temperature (adapted from Smart et al., 2004; see Deissmann et al. (2020) for all details).....	33
Figure 9 – Effect of temperature on the long term (t > 365 days) uniform corrosion rate of carbon steel exposed to alkaline and anoxic environments (see Deissmann et al., 2020 for all details). Closed symbols represent tests conducted in solutions; open symbols represent tests conducted in cement. ....	34
Figure 10 – Compilation of uniform corrosion rates (reported in the non-nuclear industrial and nuclear waste management literature) of carbon steel in anoxic and alkaline chloride-free solutions (pH 12 – 13.5); see Kursten et al. (2015) and Deissmann et al. (2020) for further details. ....	34
Figure 11 – Long-term corrosion rates of carbon steel under aerobic and anaerobic conditions selected for the reactive transport modeling in Task 4 of ACED; there is a gap in the data between neutral pH and high pH values. ....	35
Figure 12 – Corrosion current density evolution during the corrosion of carbon steel reinforcement in a low-pH cement mortar and in a OPC cement mortar as reference (García Calvo et al., 2013). ....	36
Figure 13 – Diagram of consecutive actions within one timestep as implemented by HYTEC. T denotes total concentrations, tilt T mobile concentrations, L transport operator (hydrology) and R reaction operator (chemistry). ....	38
Figure 14 – Schematic representation of the first BACUCE in-situ experimental set-up in the Tournemire URL at ambient temperature (15°C) (top) and zoom on the heterogeneous configuration of the reactive chamber (bottom). In the new experiments that will be conducted at 80°C, the borehole diameter is equal to 101 mm, and the tube diameter to 65 mm.....	44
Figure 15 – Schematic representation of the BACUCE experimental set-up at the laboratory (the green zones stand for the mechanical support of the steel “coupons”, not for the bentonite/grout cylinders). ....	45

Figure 16 – Schematic representation of the laboratory scale experiment simulating the BACUCE experiment. The prepared steel surface following the ASTM standard method are represented hatched. a) experiment with S235 steel and b) experiment with TU37b steel. .... 46

Figure 17 – (a) Calculated stability diagrams of Al-phases at 20°C and 70°C (act.  $Ca^{2+} = act. Al(OH)_4^- = 10^{-3}$ ,  $[HCO_3^-]_{total} = [H_4SiO_4]_{total} = 10^{-3}$  molal) considering katoite in the mineral assemblage. (b) modeling of the conversion of ettringite into monosulfoaluminate without considering katoite in the mineral assemblage. .... 49

Figure 18 – Steel/concrete experiment with the Boda clay: dimensions of the concrete cylinder in dark grey and steel cylinder in blue (left), and picture of the set-up (right). .... 59

## List of Tables

Table 1 – C-S-H model sites with their respective moieties (species), [mole amount], and constraints for generating discrete phases. ....	26
Table 2 – Example of discretized simple C-S-H solid solution into 18 discrete phases using a 0.5 compositional step size for Ca I, Si (S) and vacancy (v). ....	27
Table 3 – Iron bearing endmembers for Fe uptake in C-S-H. ....	28
Table 4 – Cement composition (CEM I 52.5 N – Lafarge). ....	48
Table 5 – Preliminary modeling of the mineralogy of the hydrated CEM I paste (Val d’Azergues) at 20°C and after a temperature increase to 80°C. ....	48
Table 6 – Preliminary modeling of the porewater chemistry of the hydrated CEM I paste (Val d’Azergues) at 20°C and after a temperature increase to 80°C. ....	48
Table 7 – Recipe and bulk composition of the bentonite/cement grout used in the modeling. ....	49
Table 8 – Preliminary modeling of the mineralogy of bentonite/cement grout derived from batch experiments made with demineralized water at 20°C and a L/S ratio = 1 (ST1-1-7j). ....	51
Table 9 – Selectivity constants of cationic exchange (Gaines-Thomas formalism, Tremosa et al., 2012) and constants of surface complexation reactions (non-electrostatic model, Marques et al., 2012) of montmorillonite considered in the modeling of the bentonite fraction of the grout as well as for the clayey phase of the argillite. ....	52
Table 10 – Preliminary modeling of the batch experiment, water chemistry: bentonite/cement grout in contact with demineralized water at 20°C, L/S ratio = 1 (ST1-1-7j). ....	52
Table 11 – Preliminary modeling of the mineralogy of the bentonite/cement grout at 80°C. ....	53
Table 12 – Preliminary modeling of porewater chemistry of the bentonite/cement grout at 80°C. ....	54
Table 13 – Mineralogical composition of Toarcian argillite at the URL depth (Tremosa et al., 2012). .	55
Table 14 – Cation exchange properties of reference for the Toarcian argillite at 20°C (Tremosa et al., 2012). ....	55
Table 15 – Composition of reference for the argillite porewater (Tremosa et al., 2012). ....	55
Table 16 – Possible recipe for the young CEM I synthetic water for the BACUCE experiment at 20°C. ....	56
Table 17 – Bulk recipe for the synthetic water of the bentonite/cement grout experiment at 20°C (i.e. for rehydrating the boreholes) without bacteria nutrients. ....	56
Table 18 – Composition of the synthetic water of the grout BACUCE experiment (i.e. for rehydrating the boreholes) at 20°C. ....	57
Table 19 – Saturation indices of the supersaturated phase for the grout-type synthetic water (BACUCE experiment). ....	57
Table 20 – Simplified composition of the CEM IIB concrete. ....	60
Table 21 – Bulk composition of the CEM IIB/S cement (Lubloy et al., 2016). ....	60
Table 22 – Composition of reference for the porewater of the Boda claystone at 20°C. ....	61

## 1. Introduction and context

*MINES ParisTech and PSI*

### 1.1 Context, steel/cement interface in HLW and ILW disposal cells

Understanding the evolution of the interface between steel and cement-based materials is essential for the integrity of the repository barrier system. Cement-based materials are used in many deep geological repository concepts and come in contact with various metallic materials that are part of the waste or that are part of the barrier system (i.e. containers).

The concepts of disposal cell for vitrified high-level waste (HLW) embedded in an argillaceous sedimentary formation for the Belgium, Dutch and French national programs as schematically shown in *Figure 1* (Andra, 2016a; Weetjens et al., 2012; Neeft et al., 2019). The first two programs share the same concept of the so-called supercontainer. In both concepts, the steel overpack encapsulates the waste canisters that contain the vitrified waste (Andra, 2016a; Deissmann et al., 2016).

The supercontainer diameter is about 2 m, and consists in a carbon steel overpack (7.5 cm thick) containing the HLW is encased in prefabricated cylindrical concrete buffer material. The concrete is made from ordinary Portland Cement (OPC or CEM I type) and limestone aggregates. The pH has to be kept at high values (pH around 12.5, i.e. buffered by portlandite) in order to keep the carbon steel overpack passivated, to limit corrosion and ultimately to minimize radionuclide release from the vitrified wastes. The lifetime of the overpack have to be at minimum longer than the thermal phase (the thermal phase corresponds to the decay of the larger part of the radionuclides). The temperature at the steel overpack decreases from 80°C to 40°C in less than 200 years for most nuclear glasses and in 1 000 years for the warmest wastes (Neeft *et al.*, 2019). Afterwards, the temperature continues to decrease to the natural background temperature (about 25°C) but more slowly.

The French concept (Andra, 2016a) significantly differs from the supercontainer concept by considering a 25 mm thick sleeve made of low-carbon steel in an indurated clay formation. The annular gap between the sleeve and the host rock is filled with a bentonite/cement grout that imposes corrosion-limiting environmental condition during the thermal phase only. The injection of the cement-bentonite grout is considered to counter the acidic pH transient (pH ~ 4.5) resulting from the host rock oxidation which may lead to high corrosion rates. The grout also passivates metallic surfaces. It also strongly reduces the diffusion of atmospheric O<sub>2</sub> to the steel due to its water saturated state and low effective diffusion coefficient. The alkalinity of the grout will be readily neutralized afterwards to prevent the dissolution of the nuclear glass under high pH values. Neutralization is driven by the interaction with the surrounding host rock, including hydrolysis and carbonation.

In both HLW concepts, the chemical evolution at the interface between the carbon steel and a cementitious material is critical issue to minimize steel corrosion. The effect of thermal phase from 80°C to 25°C on steel corrosion, both from a thermodynamic and kinetic points of view, is also an important common question. To better understand and quantify of the interaction between cement and steel at high temperature is the objective of the present subtask 2.2.

The different national concepts of disposal cell for intermediate level waste (ILW) present a wider diversity of configurations and materials (Neeft et al., 2019) compared to the HLW disposal concepts. *Figure 2* shows the schematic configuration of a disposal cell for intermediate level waste (ILW) of reference the ACED work package. However, in most concepts carbon steel is used for the containers of the ILW packages that are the immobilized in a concrete or steel container with a cement-based material. The Dutch concept may also rely upon the supercontainer concept of *Figure 1*, except that the waste inside the stainless canister is metallic waste instead of glass. The maximum temperature is lower for ILW than HLW, usually below 40 – 50°C.

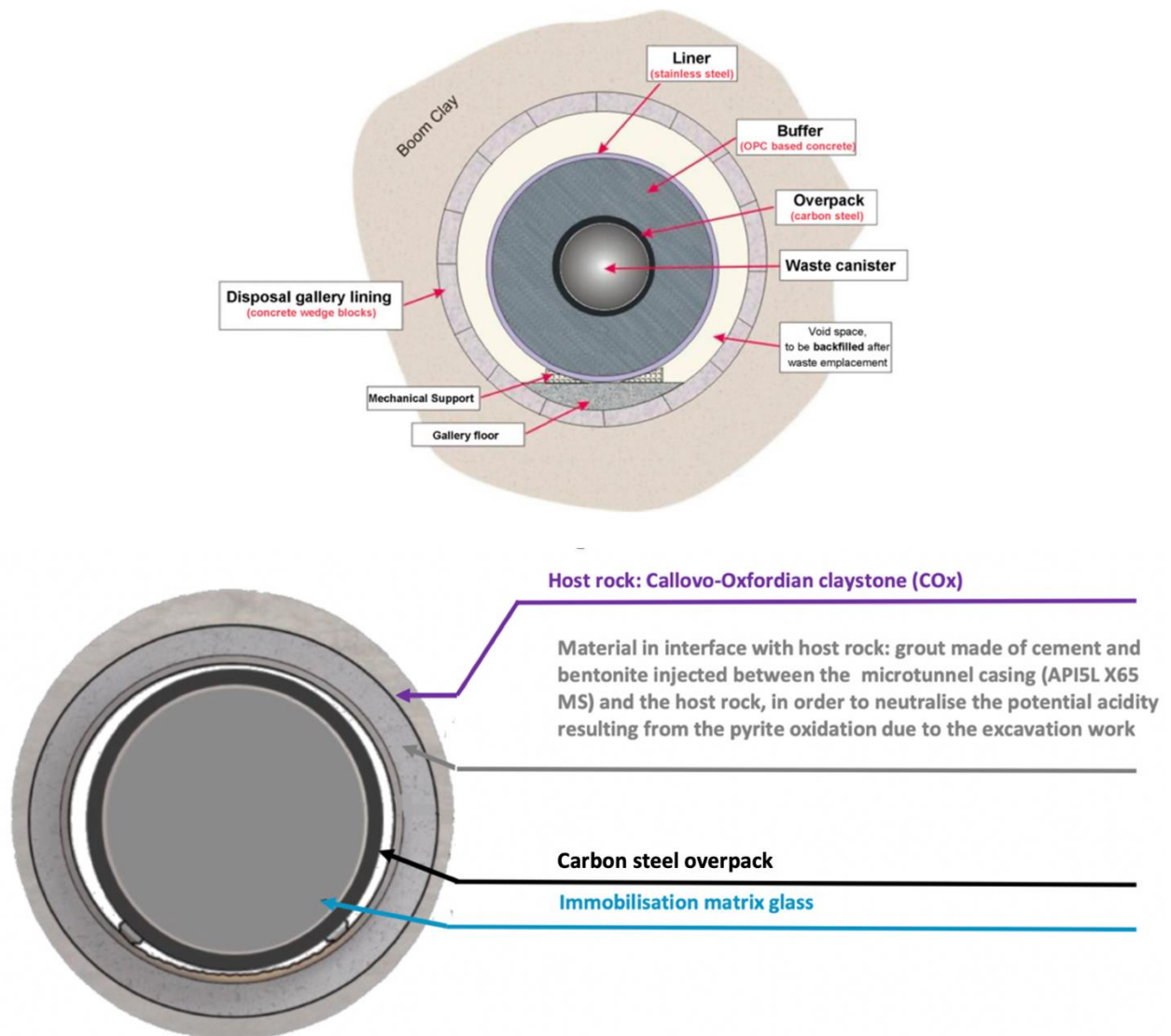


Figure 1 – Cross-section of the HLW disposal cell in a clay host rock for the Belgian/Dutch supercontainer concept (top, Craeye et al. (2009)) and the French sleeve concept (bottom, Andra, 2016a).

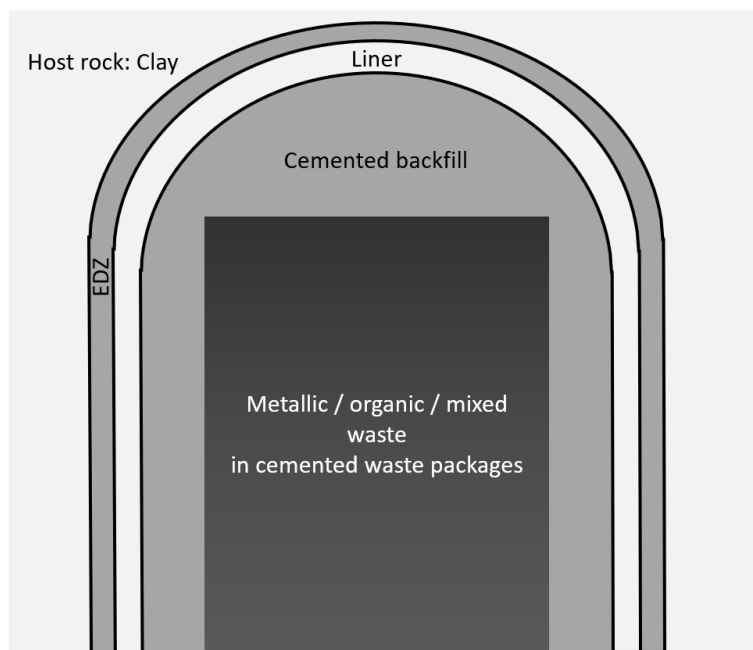


Figure 2 – Representative ILW disposal cell (ACED work package).

## 1.2 Aims and structure of this deliverable

Subtask 2.2 of the ACED work package of EURAD relies upon a combined modeling-experimental approach that can provide key information to geochemical and coupled reactive transport models for assessing chemical evolution at steel/cement material interfaces. This combined approach will provide the bases of the up-scaling to waste package (Task 3) and disposal cell (Task 4) modelling.

Iron is released due to the steel corrosion and diffuses into the cement leading to the formation of various solids and can also be incorporated in existing phases. The evolution of important chemical (redox, pH, ionic strength) and other variables (e.g., mineralogy, porosity) at the steel-cement interface is influenced by the mineralogical phases that form and their stability under the evolving conditions. Many of these phases are not pure but are present as a mixture of two or more components which must be modelled as solid solutions, or as discrete phases compositions. One such phase is C-S-H (calcium-silicate-hydrate), the main component of hydrated cement that has been shown to retain significantly more iron when compared to aluminum (Mancini et al., 2020a). Chapter 2 provides details on the thermodynamics of iron in cement phases and steel corrosion products as well as preliminary results on modeling the uptake of Fe(III) in C-S-H a major cement hydrate phase.

However, the metallic iron that forms the main component of low carbon or weakly alloyed steels is never under equilibrium in contact with aqueous solutions, both under oxic and anoxic redox conditions. It will be subjected to several types of corrosion processes, such as generalized (uniform) corrosion or localized corrosion (e.g. pitting corrosion). Steel corrosion in a low-pH environment is still poorly known. Chapter 3 gives a literature overview of steel generalized corrosion rates under the environment of low-pH and high-pH cementitious materials.

Reactive transport models (RTMs), by definition, can simulate the transport and chemical reactions of multiple solutes (and gases) and their chemical interaction within the multi-barrier system over various time and spatial scales (Bildstein et al., 2019). Reactive transport models have, therefore, become an invaluable component in assessing the potential performance of a repository, which requires an understanding how the various barriers evolve through space and time (De Windt and Spycher, 2019; Idiart et al., 2020). Reactive transport modeling is also capable of great generality and flexibility and can

be applied to a wide range of natural processes, as well as to engineering issues such as metal corrosion or bentonite alteration. Chapter 4 provides for the main features of the HYTEC code (van der Lee et al., 2003).

The in situ BACUCE project (led by IRSN) aim at studying the steel/cement interface under the most representative disposal conditions as possible, including carbon steel plus high-pH and low-pH cement materials embedded in a clayey host rock at low (15°C) and high (80°C) temperatures. It is one of the outstanding experiments of Task 2. The BACUCE experiments consists of (i) on-going in situ experiments with a steel-cement interface at 20°C, (ii) a number of existing data from laboratory experiments at 20°C on cement/bentonite grout and (iii) a new set of in situ and lab experiments on the steel/cement interface performed at 80°C with the grout as well as with a hydrated CEM I paste. The bentonite/cement grout is a new type of engineering material of which chemistry and hydration products are not well defined yet both at ambient and high temperatures. The in situ experiment takes place in a borehole drilled in the Toarcian argillite of the Tournemire underground research laboratory (URL). Chapter 5 presents in details the geometrical configuration of the experimental setups as well as the geochemical, mineralogical and diffusion properties of the cementitious and clayey materials. Preliminary geochemical modeling is then developed to define the initial state of the numerical HYTEC models that will be at the later stage of the ACED project compared with the measurements from the experiments.

Chapter 6 deals with the laboratory experiments (led by MTA) are also performed to gain information on the corrosion intensity of the S235JR carbon steel inserted in CEM IIB concrete (hydrated by synthetic water of the Boda claystone, materials that are presently considered in the Hungarian disposal concept. The temperature of reference is 80°C for the sake of consistency and comparison with the other experiments of Subtask 2.2.

Eventually, Chapter 7 examines the possible improvements and simplifications for modeling of processes at the cement/steel interface and relevant knowledge gaps and missing processes.

## 2. Thermodynamics of Fe-containing cement phases

PSI

This chapter provides a summary of relevant aspects related to the formation of iron bearing cement hydrates and corrosion products as well as preliminary results for modelling iron uptake by C-S-H. First, a summary on the recent development concerning thermodynamic databases for modelling cementitious systems (CEMDATA18, PSI/Nagra, Thermodem and Thermochimie) is presented. Details on the iron bearing cement phases, corrosion products and pore solution aqueous species are provided, with a focus on their relative stability and their prevalence due to possible changes in chemistry and redox conditions. Aspects on the non-ideal solid-solution modeling are then presented and its use for describing Fe-AFm (monosulfate), Fe-AFt (trisulfate), and Fe C-S-H phases. For modeling codes that cannot use non-ideal solid solutions the method of discretizing a solid solution model into discrete pure phases composition is proposed as an alternative. Finally, preliminary results on extending the newly developed C-S-H model accounting for the uptake of Fe(III) are shown.

All these points are essential for assessing the fate of iron that results from corrosion, which diffuses at the steel/cement interface into the cement material, and serve as inputs and constraints for improving the reactive transport modelling at the interface and waste package level.

### 2.1 Thermodynamic database evolutions for cement phases

#### 2.1.1 CEMDATA18 database

CEMDATA18 (Lothenbach et al., 2019) (<https://www.empa.ch/cemdata>) contains thermodynamic data for common cement hydrates such as C-S-H, AFm and AFt phases, hydrogarnet, hydrotalcite, zeolites, and M-S-H that are valid over temperatures ranging from 0 to at least 100°C and is currently available for GEM-Selektor (Kulik et al., 2012) and PHREEQC (Parkhurst and Appelo, 2013) modeling tools. The database also contains several ferric iron bearing AFm and AFt phases, hydrogarnet, and hydrotalcite phases. From the critical review of all available experimental data the solubility constants were calculated. Additional experiments were made for obtaining data for critical phases or to verify existing data (Lothenbach et al., 2019).

**When compared to Cemdata07 (published in 2008) the most significant differences are related to the improvements in the aluminum and iron containing phases, as well as the changes in the C-S-H models concerning the volume and the alkali uptake. These changes can lead to considerably different modeling results between the two database versions.**

The stability constants for the cement phases were obtained by recalculating the experimental data using the PSI/Nagra 12/07 (Hummel et al., 2002; Thoenen et al., 2014) as a source for the aqueous species, gas and other solid components participating in the reactions. This makes CEMDATA18 fully compatible with the PSI/Nagra 12/07 chemical thermodynamic database. For the GEM-Selektor geochemical modeling software, which uses the Gibbs energy of all species in phases to calculate equilibrium, the Gibbs energy of formation for all CEMDATA18 components were calculated based on their reported logK's (Lothenbach et al., 2019) and reactants from the PSI/Nagra 12/07. Some additional data for solid phases (e.g. carbonates, Al hydroxides, Fe oxides, hydroxides, sulfides, etc.) relevant for cementitious systems, distributed with CEMDATA18, are also from the the PSI/Nagra 12/07. Solid solution models (a solid solution is a solid phase that can be described as a mixture of two or more solid species (constituents, endmembers).) for AFm, AFt, C-S-H, and M-S-H are also included in the CEMDATA18 database GEM-Selektor [3] version. For C-S-H, several alternative solid solution models are available. Non-ideal binary Redlich-Kister (Guggenheim) (Glynn, 2019) solid solution models are used for: (Al, Fe)-ettringite, (Al, Fe)-monosulfate, (SO<sub>4</sub>, OH)-monosulfate, and (SO<sub>4</sub>, OH)-ettringite. (Al, Fe)-siliceous hydrogarnet, C-S-H, M-S-H, hydrotalcite-pyroaurite, (Mg, Al)-hydrotalcite, straetlingite and ettringite (for different water content) are treated as ideal solid solutions.

CEMDATA18 is also available in LMA (Law of Mass Action) setup that requires thermodynamic data in the form of log K values for both aqueous complexes and solids. The database has been recasted into PHREEQC “dat” format (Miron et al., 2018a). The PHREEQC version of the database contains all the reactions for the cementitious components and the related subset of general thermodynamic data (mainly aqueous species) from PSI-Nagra TDB need for the reactions. The PHREEQC version of the CEMDATA18 can also be used at elevated temperatures, 0 - 100 °C. The coefficients for the  $\log K = f(T)$  were calculated from the available data on the entropy and heat capacity effect of the reactions. To use solid solutions in PHREEQC, these must be defined by the user in the input script calculation file using the endmember names from the database.

When using the CEMDATA18 database for equilibrium calculations, based on their thermodynamic data alone, some phases are more stable than others, but they might not form during the timescale of the modeled process. For example, the Fe-containing AFm and AFt hydrates have a limited stability field due to the high stability of goethite (FeOOH) and hematite (Fe<sub>2</sub>O<sub>3</sub>). The latter should to be suppressed when doing calculations at ambient conditions in favor of: microcrystalline FeOOH (or microcrystalline or amorphous Fe(OH)<sub>3</sub>), but should be allowed to form at elevated temperatures (> 50°C) or when considering very long time scales. Similarly, the formation of gibbsite (Al(OH)<sub>3</sub>) and quartz (SiO<sub>2</sub>) should be suppressed in favor of microcrystalline or amorphous Al(OH)<sub>3</sub>, and amorphous SiO<sub>2</sub>.

### 2.1.2 PSI/Nagra database

The PSI/Nagra thermodynamic database contains data to support modeling geochemical processes related to low- and intermediate-level and to high-level radioactive waste (conditions in Switzerland). The initial database was issued in 1992 (Pearson et al., 1992; Pearson and Berner, 1991) and was later followed by two major updates, Nagra/PSI Chemical Thermodynamic Data Base 01/01 (TDB 01/01) (Hummel et al., 2002) and PSI/Nagra Chemical Thermodynamic Data Base 12/07 (TDB 12/07) (Thoenen et al., 2014). The data selection is based on detailed in-house reviews and on the OECD NEA’s book series on “Chemical Thermodynamics”. The current version of the PSI/Nagra Chemical Thermodynamic Data Base is 12/07 (TDB 12/07) (Thoenen et al., 2014). A new version of the database (PSI Chemical Thermodynamic Database 2020) with updated thermodynamic data is under development. The critically selected data is classified into core data, based on the CODATA key values (Cox et al., 1989), recommended application data, with well-characterized aqueous species, minerals, and gases, and supplemental data, with less well-characterized uncertain data suitable for scoping and qualitative calculations (for cases where omission of data even if uncertain would lead to unacceptable results).

The PSI/Nagra database is available both in GEM-Selektor (Kulik et al., 2013) and in PHREEQC (Parkhurst and Appelo, 2013) format. The PHREEQC version of the database contains data for reference temperature (25°C) and pressure (1 bar). In the GEM-Selektor version the data for aqueous species was augmented with parameters for the HKF (Helgeson-Kirkham-Flowers) equation of state (Tanger and Helgeson, 1988) taken from the SUPCRT slop98 database (Johnson et al., 1992). These allow the extrapolation of their properties at different temperatures and pressures. For solid phases additional data on the heat capacity temperature function is provided with coefficients collected from Robie and Hemingway (1995) and Helgeson et al. (1978). Some of the components are defined using reaction data, as reaction dependent components. In this case, depending on the available data on the entropy and heat capacity effects of reaction, the three-term, two-term or constant logK, extrapolation methods are used for calculating the logK values as a function of temperature.

The thermodynamic data for iron in the PSI/Nagra Chemical Thermodynamic Data Base 12/07 (TDB 12/07) were accepted from the section of Hummel et al. (2002), Nagra/PSI Chemical Thermodynamic Data Base 01/01 (TDB 01/01). Most of the iron data come from the original selection by Pearson, in the Nagra Thermochemical Data Base 05/92 (TDB 05/92). Pearson selected data from Wagman (1982) (properties of formation of the master species Fe<sup>2+</sup>) and from Nordstrom et al. (1990) and Baes and

Mesmer (1977) (inorganic complexes of iron and iron solids). The database was further enhanced with the addition of data for hematite, magnetite, pyrite, and troilite by Hummel et al. (2002).

A major revision on the data for iron is in progress (PSI Chemical Thermodynamic Database 2020). This revision concerns most of the iron aqueous species and iron bearing solid phases in the PSI/Nagra database. The new data selection is based mainly on the recent OECD NEA's volume on the thermodynamics of iron by Lemire et al. (Lemire et al., 2013).

### 2.1.3 Other databases (Thermoddem and ThermoChimie)

Thermoddem is a database for the thermodynamic properties of interest for hazardous and radioactive wastes, as well as the geochemistry of natural environments (Blanc et al., 2012). The database is developed by the French geological survey (<https://thermoddem.brgm.fr>). The last qualified version of Thermoddem (V1.10, 2017) is formatted for several reactive transport models including CRUNCH, HYTEC, PHREEQC or THOUGHREACT. An update version (V1.10, 2019) is under progress.

Thermoddem is applicable to the full pH range, including the high-pH alkaline domain, from 0 to 100°C. The database includes a large set of zeolites and cementitious phases with a broad composition range with respect to concrete formulae such as CEM I and low-pH cements. The C-A-S-H, C-S-H and M-S-H phases are introduced as discrete elements. A few iron-bearing cement phases are present such Fe-AFm and Fe-AFt. Thermoddem is also suitable for modelling iron corrosion products such as iron carbonates, oxyhydroxides, silicates and sulfides.

Additional data for iron corrosion products or clay phases can be selected from ThermoChimie, which is the thermodynamic database developed by ANDRA, ONDRAF and RWM for the performance assessment of the geologic disposal of radioactive waste (Giffaut et al., 2014, <https://www.thermochimie-tdb.com>). ThermoChimie provides formation constants (at temperatures  $\leq 80^\circ\text{C}$ ) for a wide range of radionuclides and the mineral component of multi-barrier systems, including host-rock solid phases, bentonites, cements, steel, and their evolving secondary phases. The database is formatted for several reactive transport models including HYTEC.

## 2.2 Fe-containing phases and pore solution

### 2.2.1 Fe-containing cement phases

The main hydrated phases of ordinary Portland cement are portlandite, calcium silicate hydrates (C-S-H), AFt, e.g. ettringite (calcium-alumina hydroxide trisulfate) and/or AFm phases, e.g. calcium-alumina hydroxide monosulfate/monocarbonate (Lothenbach and Winnefeld, 2006). Several iron bearing cement phases have been reported (depending on the amount of calcium, sulfate or carbonate): Fe-ettringite, Fe-monosulphate, Fe-hemicarbonate, and Fe-monocarbonate (Dilnesa et al., 2012, 2011; Möschner et al., 2008, 2009), other Fe-containing phases are Al-Fe hydrotalcite and hydrogarnet (Dilnesa et al., 2014b, 2014a; Vespa et al., 2015). In the presence of silica Al- and Fe-containing siliceous hydrogarnets forms as a stable phase while Fe-hydroxides form in the absence of silica (Dilnesa et al., 2014b). Because of their similarity to the Al-containing analogues (overlapping signals), Fe-containing phases are difficult to analyze with standard techniques such as XRD, TGA, SEM. Synchrotron-based X-ray absorption spectroscopy (XAS) is a well suited powerful technique for studying Fe speciation in cementitious systems (Dilnesa et al., 2014b; Vespa et al., 2015).

Initial iron in ordinary Portland cement comes from the ferrite clinker phase  $\text{C}_2(\text{A},\text{F})$ . In contact with water, ferrite and the other clinker phases dissolve and lead to the formation of hydrated cement phases. Experimental studies and thermodynamic modeling show that the most stable Fe-bearing hydrated cement phase is the Fe-siliceous hydrogarnet (mixed Fe-Al solid solution). The Fe bearing siliceous hydrogarnet is  $\sim 7$  log units more stable than its Al counterpart suggesting that in the presence of Fe this

phase is always preferred (Dilnesa et al., 2014a). By contrast, other Fe-containing hydrates (AFm, Aft) have very similar stabilities as compared to their Al-containing analogues, being only slightly more stable (Lothenbach et al., 2019). The presence of Fe-siliceous hydrogarnet was identified in cement paste hydrated for 10 and 50 years (Dilnesa et al., 2014b; Vespa et al., 2015) using XRD, SEM/EDX, XAS and EXAFS, and in different cement compositions like ordinary Portland cement (OPC) (Dilnesa et al., 2014b), ferrite-rich cement (Elakneswaran et al., 2019), and sulfate resistant cement (HS) (Dilnesa et al., 2014b).

Ferric iron is substituting structural Al from the Al-bearing Aft, AFm, hydrotalcite, and hydrogarnet. Experimental studies have identified the formation of solid solutions forming in the case of ettringite, siliceous hydrogarnet, monosulfate, hydrotalcite and Friedel's salt (Lothenbach et al., 2019) (see section 2.3.2). No solid solution has been identified for the Fe/Al monocarbonate pair (Lothenbach et al., 2019). In the absence of silica and calcite Fe/Al monosulfate (ettringite) will dominate, with the addition of calcite Al-ettringite, Al-monocarbonate and Fe-monocarbonate are expected to be stable (Fe-ettringite is stable only at high  $\text{SO}_3/(\text{Al,Fe})_2\text{O}_3$  ratios) (Dilnesa et al., 2012, 2011). If silica is present the Fe strongly prefers the Al/Fe siliceous hydrogarnet, while in case of the AFm and Aft phases, their Al-bearing analogues are preferred.

The Fe hydrates are more stable than the Al hydrates with Fe-monocarbonate, Fe-monosulfate, Fe-Friedel's salt and Fe-siliceous hydrogarnet readily but slowly forming at 20°C (Dilnesa, 2012). Fe-containing AFm and Aft hydrates are destabilized with increasing temperature and are replaced by goethite ( $\text{FeOOH}$ ) and hematite ( $\text{Fe}_2\text{O}_3$ ) within days at 80 °C and within months at 50°C (Lothenbach et al., 2019). The iron-containing Friedel's salt ( $\text{C}_4\text{FC}_{12}\text{H}_{10}$ ) is only stable up to 50°C, while Fe-siliceous hydrogarnet was identified also at higher temperatures (110 °C (Dilnesa et al., 2014a)). The values of the stability constant for the Fe-containing hydrates do not vary significantly with temperature (20 - 80°C). At ambient temperatures, the presence of Fe stabilizes the Fe-siliceous hydrogarnet that readily forms at these conditions as poorly crystallized phase (Lothenbach et al., 2019). Crystalline siliceous hydrogarnet was only identified at elevated temperatures or in hydrated cement samples older than 20 years (Dilnesa et al., 2014a).

Iron containing phases such as Fe-ettringite and ferrihydrite form only in the early stages of hydration. Fe-ettringite is later replaced by the more stable Al-ettringite (Elakneswaran et al., 2019; Lothenbach et al., 2008) while ferrihydrite becomes undersaturated as the pH of the pore solution increases above 13 and Fe-siliceous hydrogarnet forms instead (Dilnesa et al., 2014b). This suggests that in a low pH cement the hydrogarnet will be replaced by ferrihydrite as the most stable iron phase. Depending on the pH and with the decrease in Eh ferrihydrite can transform into goethite, hematite and magnetite (Cudennec and Lecerf, 2006; Aeppli et al., 2019).

In the presence of Mg (e.g. addition of granulated blast furnace slag) layered double hydroxides (LDH) hydrotalcite phases can form (Kayali et al., 2012; Mäder et al., 2017) with Al being exchanged by Fe in the hydrotalcite-pyroaurite solid solution (Rozov et al., 2011). These phases can bind anions such as chloride due to their anion exchange property. The presence of chloride in solution will be reduced by the possible formation of Friedel's salt and the uptake by hydrotalcite which can act as a protection against chloride induced corrosion (Kayali et al., 2012).

The uptake of iron in C-S-H has been previously considered (Faucon et al., 1996; Labhasetwar et al., 1991). First experimental data, recently available, shows that ferric iron bonds strongly to C-S-H (Mancini et al., 2020a). This has an important effect on the iron mobility and signifies that the iron which results from corrosion can be retarded by the cement and will be retained close to the cement/metal interface. A competition for the incorporation into C-S-H between iron and other cations in solution such as radionuclides will exist (Mancini et al., 2020a).

To support accurate modeling of Fe-containing phases and porewater composition in hydrated (blended) cementitious materials, the thermodynamic properties on the stability of these phases are necessary. Phase stability data were retrieved from synthesis, spectroscopy, thermogravimetric and solubility experiments (all papers) and are available in the CEMDATA18 database (Lothenbach et al.,

2019). There is no thermodynamic data available for the iron uptake in C-S-H or the effect of ferrous iron on cement phases. Information on ferrous iron-containing phases is available for corrosion products (see section 2.2.2). New available experimental data (Mancini et al., 2020 a/b) will be used to parametrize a solid-solution model for the incorporation of iron in C-S-H (see section 2.4.1).

Take away:

Fe(III)-bearing cement phases generally have low solubility with Fe-siliceous hydrogarnet being the most stable hydrate from ambient to elevated temperatures (Figure 3), while in low pH cements ferrihydrite will be stable and based on Eh can transform into goethite, hematite and magnetite. The low solubility of the iron-containing cement phases, Fe oxides and hydroxides and the uptake of it in C-S-H can lead to the containment of iron close to the cement/metal interface. The stability of Fe oxides and hydroxides phases increases with temperature leading to lower iron concentrations in the aqueous solution.

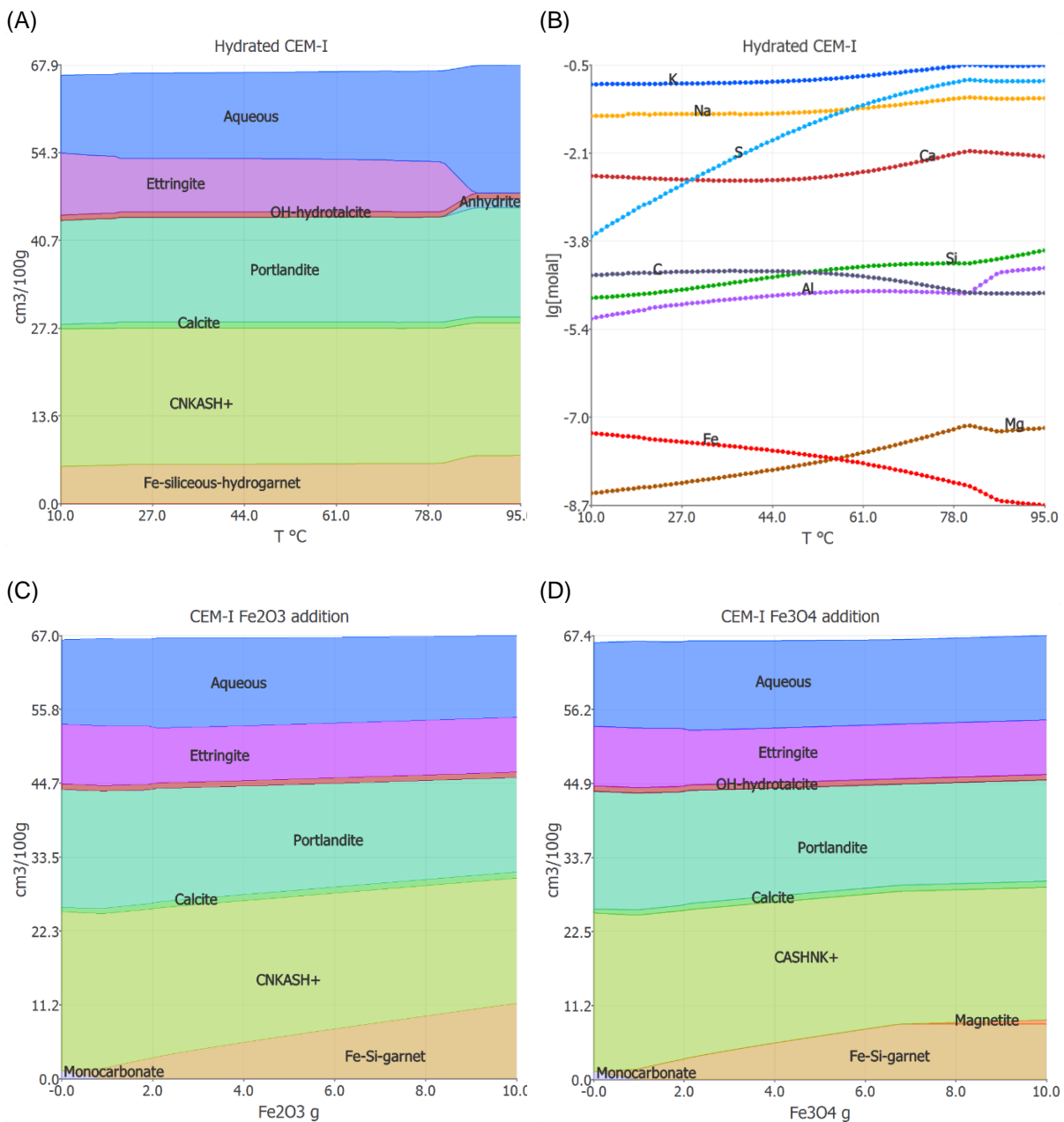


Figure 3 – Volume of cement phases in equilibrium, per 100 g of completely hydrated CEM-I as a function of temperature (A), addition of Fe<sub>2</sub>O<sub>3</sub> (C) and of Fe<sub>3</sub>O<sub>4</sub> (D). Elemental concentration in the aqueous pore solution (B). Calculations done in GEM-Selektor using the CEMDATA18 database using

*the CEM I 52.5 N – Val d’Azergues composition (w/c 0.42). The CASHNK+ solid solution model used here does not yet contain the iron uptake.*

### 2.2.2 Fe-corrosion products

Overall, the redox conditions in the waste repositories will evolve from oxidizing to very reducing conditions (Diomidis, 2014; Duro et al., 2014; Diomidis et al., 2016). In some parts due to clogging during the operational period the atmosphere could stay rich in oxygen for a longer period due to the absence of resaturation and connections to other parts of the system. Metals such as stainless and carbon steel will undergo corrosion processes. In the first short phase aerobic corrosion will occur in a deep geological repository, characterized by the formation of Fe(III) rich corrosion products. For most of the repository lifetime anaerobic metal corrosion will prevail, leading to the formation of Fe(II,III) bearing corrosion products (e.g. magnetite) and the reduction of Fe(III) rich phases from the previous phase.

Under oxic conditions, the common steel corrosion products identified are Fe(III) oxyhydroxides and oxides such as lepidocrocite ( $\gamma$ -FeOOH), goethite ( $\alpha$ -FeOOH). These two can later crystallize to maghemite ( $\gamma$ -Fe<sub>2</sub>O<sub>3</sub>) and hematite ( $\alpha$ -Fe<sub>2</sub>O<sub>3</sub>), also present are ferrihydrite (Fe<sub>2</sub>O<sub>3</sub>·0.5H<sub>2</sub>O) and Fe(III)/Fe(II)-containing magnetite (Fe<sub>3</sub>O<sub>4</sub>) (Poursaee, 2016; Saheb et al., 2014; Zhao and Jin, 2016).

In chloride-bearing environments akaganeite ( $\beta$ -FeO(OH,Cl)) and hibbingite ( $\gamma$ -Fe<sub>2</sub>(OH)<sub>3</sub>Cl) were identified (Réguer et al., 2015; Rémazeilles and Refait, 2007; Saheb et al., 2008). Other intermediary products (complex mixture of different crystalline and amorphous phases of the oxides and hydroxides) can form as a function of the solution composition, water saturation, and kinetics (Landolt, 2007). If the pore water contains chloride, sulfate, and carbonate ions, phases such as green rusts (GR1-Cl, GR2-SO<sub>4</sub><sup>2-</sup>) can form (Chaves, 2005; Nemer et al., 2011; Refait et al., 2003; Sagoe-Crentsil and Glasser, 1993; Smart, 2009). Overall, with increasing exposure time, relevant for the long periods of waste disposal systems, the most stable phases are goethite, hematite (oxidizing) and magnetite (oxidizing and reduced conditions) (Zhao and Jin, 2016).

Under anoxic conditions relevant for the waste disposal the most predominant corrosion product is magnetite (Fe<sub>3</sub>O<sub>4</sub>) (Diomidis, 2014). Initially, Fe(III) from phases formed during oxic corrosion is electrochemically reduced to Fe(II), while Fe(0) is oxidized to Fe(II)



Fe(0) from the steel is oxidized leading to the formation of Fe(II)-bearing corrosion products mainly magnetite and ferrous hydroxide (Fe(OH)<sub>2</sub>). Ferrous hydroxide is then transformed into magnetite via the “Schikorr reaction”:



The Schikorr reaction is favored by increasing temperature (magnetite is more stable) and by the presence of some impurities (e.g. nickel, copper, cobalt) (Smart et al., 2004), while others can inhibit it (e.g. magnesium) (Kursten et al., 2004). In more recent experimental studies done in conditions relevant to deep geological repositories, magnetite was identified as the sole corrosion product in neutral and alkaline systems under anoxic conditions and ambient temperatures (Diomidis, 2014; Smart, 2009; Smart et al., 2017, 2006, 2004).

An important characteristic of the cement that influences the corrosion process is that it maintains a high pH chemical system (10.5 to 13.5) (Diomidis, 2014; Kosakowski et al., 2014; Kursten et al., 2004). The pH of the pore solution is controlled by the cement constituents. Initially very alkaline pH (~13.5) is set by the presence of dissolved NaOH and KOH. With the ingress of external fluids, the pH control by the alkalis will be reduced and the pH will decrease to 12.5 set by equilibrium with portlandite. When all the portlandite is dissolved, C-S-H phases start dissolving. The non-stoichiometric dissolution of C-S-H, the main cement constituent, controls the pH in the range below 12.5. The final product of this degradation

process are C-S-H phases with a low Ca:Si ratio, which will keep the pH ~11. Simulations have shown that a pH > 12 is expected to last more than 100,000 years, while a drop below 10.5 should not happen before 1-5 million years, depending on groundwater ingress from the host rock (Kurstien et al., 2004). Relevant simulations and experimental studies on steel corrosion and cement steel interface are the ones done in alkaline solutions at pH  $\geq 11$  (mainly in anoxic conditions expected for most of the repository lifetime).

The nature of the corrosion products is also influenced by the presence of other elements in solution. For example, carbon and sulfur, can lead to the formation of iron carbonates and iron sulfides. Iron carbonates such as  $\text{FeCO}_3$ , and  $\text{Fe}_2(\text{OH})_2\text{CO}_3$  and  $\text{Fe}_6(\text{OH})_{12}\text{CO}_3$ , or the ferrous hydroxysalt chukanovite  $\text{Fe}_2(\text{OH})_2\text{CO}_3$  have been reported (King, 2008; Odorowski et al., 2017; Papillon et al., 2003; Saheb et al., 2014; Taniguchi et al., 2010).

Carbon/carbonate originate from the degradation of the organic matter or can come from the dissolution of the main carbon-containing minerals (e.g. calcite) and cement hydrates (monocarbonates and hemicarbonates). Sulfur is present in the AFt (e.g. ettringite) and monosulfate hydrate cement phases in its oxidized sulfate form, and can come from oxidation of sulfide phases in the host rock. Under alkaline and reducing conditions hydrogen sulfide ( $\text{HS}^-$ ) is the stable sulfur species, but the reduction of sulfate to sulfide is extremely slow at  $<150^\circ\text{C}$  and will not proceed unless it is mediated by microbial activity (Truche et al., 2009). Sulfate reducing bacteria have been identified in the host rocks of the deep geological repositories (Bagnoud et al., 2016; Boylan et al., 2019; Leupin et al., 2017). Experimental investigations of Fe(0)-containing slag cement showed the presence of reduced aqueous S species in the pore solution, e.g. sulfite ( $\text{SO}_3^{2-}$ ), thiosulphate ( $\text{S}_2\text{O}_3^{2-}$ ) and sulfide ( $\text{HS}^-$ ) (S(-II)) from the slag reaction in addition to  $\text{SO}_4^{2-}$  (S(VI)) from Portland cement (Gruskovniak et al., 2008; Lothenbach et al., 2007). This suggest that strongly reducing conditions prevail in Fe(0)-containing slag cements, which results in the abiotic reduction of sulfur and precipitation of iron as iron sulfide.

There is no data available on possible microbial activity developing in the near field around the cement surrounding the canisters. Most of the activity is expected to be close to the host rock, for example around the emplacement tunnel lining that can be made from reinforced concrete. Common iron sulfides that can form under repository conditions are FeS-mackinawite and  $\text{FeS}_2$ -pyrite. Troilite (FeS), pyrrhotite ( $\text{Fe}_{1-x}\text{S}$ ) and marcasite ( $\text{FeS}_2$ ) are more common at increasing temperatures (Cloet et al., 2017). Experiments have shown that in the presence of  $\text{H}_2(\text{g})$  (corrosion product), pyrite is reduced to pyrrhotite (Betelu et al., 2012; Truche et al., 2013, 2010). This reaction is favored by increasing temperature, alkalinity, and hydrogen partial pressure. The highly alkaline conditions of the cement pore water make this reaction possible at ambient temperature (Truche et al., 2013).

In the presence of Cl<sup>-</sup> in the pore solution hydroxychloride phases can form on the metal surface. The ferric hydroxide  $\beta\text{-FeO}(\text{OH},\text{Cl})$  akageneite forms under oxic conditions while hibbingite,  $\gamma\text{-Fe}_2(\text{OH})_3\text{Cl}$ , ferrous compound forms under anoxic conditions (Nemer et al., 2011; Refait et al., 2003; Réguer et al., 2015; Rémazeilles and Refait, 2007). The formation of hibbingite from ferrous hydroxide in the presence of chloride require metastable intermediates (GRs) and is a slow process and  $\text{Fe}(\text{OH})_2$  is favored with increasing pH, while the hydroxychloride phases form in neutral to slightly alkaline environments (Nemer et al., 2011; Rémazeilles and Refait, 2007). On long time scales,  $\text{Fe}_2(\text{OH})_3\text{Cl}$  transforms into magnetite (Réguer et al., 2015).

Important intermediate phases that form during partial oxidation of Fe(II) or partial reduction of Fe(III) are green rusts (GR, mixed valence layered iron(II)-iron(III)-hydroxides) (Shabalin et al., 2019). Depending on the degree of oxidation and composition of the GR, in oxidizing environment they are converted into maghemite, goethite, lepidocrocite, ferrihydrite, and akageneite, while in reducing conditions the final products are mainly magnetite, ferrous hydroxide ("white rust") (Erbs, 2004). GRs generally form in anoxic, neutral to slightly alkaline systems in the presence of anions such as carbonate, sulfate, or chloride (Sagoe-Crentsil and Glasser, 1993). Cement phases keep ligands such as carbonate and sulfate generally low in solution (e.g. carbonate would react with portlandite to form calcite) and the high pH of the pore water decreases the stability of GRs. Sagoe-Crentsil and Glasser (1993) have shown

that in the presence of high chloride concentrations in solution the stability field of the chloride green rust GR1(Cl<sup>-</sup>) extends at higher pH values (12 and above). Chloride ions can be bound in Friedel's salt or can be incorporated into hydrotalcite phases and thus reducing their concentration and possibly decreasing the stability field of GR1(Cl<sup>-</sup>).

In the presence of oxygen the ferrous corrosion products will be destabilized and depending on the solution properties GRs will be intermediate products before being transformed into stable oxide (magnetite) or oxyhydroxide (goethite, akageneite, lepidocrocite) phases (Réguer et al., 2015).

#### Take away

In the long run, under anoxic, alkaline (pH >11) conditions, at the cement/steel interface the most common and stable corrosion product is magnetite, while under oxic conditions these are goethite and magnetite. Depending on kinetics, temperature and local composition different intermediate phases can form (e.g. amorphous oxide/hydroxide phases, hydroxychloride phases, GR1(Cl<sup>-</sup>)) and the formation of the stable iron oxides/hydroxides can be inhibited.

### 2.2.3 Fe speciation in cement pore solution

The cement pores solution is characterized by a high pH. Depending on the stable phases a pH >11 exists. Under these conditions the concentrations of Fe<sup>2+</sup> and Fe<sup>+3</sup> ions (depending on the redox conditions) are very low with most of the iron is hydrolyzed in the form of Fe(OH)<sub>3</sub><sup>-</sup> and FeO<sub>2</sub><sup>-</sup> (or represented as Fe(OH)<sub>4</sub><sup>-</sup>) species, respectively. The amount of iron dissolved in the pore solution is fixed by the solubility of the Fe-bearing phases. The most stable being the Fe-siliceous hydrogarnet keeps the iron <10<sup>-8</sup> mol/kg, the next most stable being the microcrystalline ferrihydrite, the Fe-monocarbonate, -monosulfate, and hemcarbonate (dissolved iron <10<sup>-5</sup> mol/kg), with amorphous ferrihydrite being the most soluble. The presence of different ligands such as chloride, sulfate or carbonate could lead to the formation of complexes with iron, depending on their aqueous concentrations. Iron chloride species can have an important role during the GR1(Cl<sup>-</sup>) formation, enhancing the solubility and transport of iron (Sagoe-Crentsil and Glasser, 1993). In addition, iron could make complexes with silicate (e.g. FeHSiO<sub>3</sub><sup>2+</sup>). Due to the relatively low solubility of the iron phases, the competition with the other cations for ligands (e.g. formation of NaCl<sub>(aq)</sub>, CaCl<sub>2</sub>, CaSiO<sub>3(aq)</sub>, CaSO<sub>4(aq)</sub>, CaCO<sub>3(aq)</sub>) and the high pH, it is expected that the iron hydrolysis complexes dominate the pore solution.

#### Take away:

In the high pH of the cement pore water iron hydrolysis complexes will dominate the pore solution. The presence of chloride ions could enhance the solubility and transport of iron.

## 2.3 Non-ideal solid solution model

### 2.3.1 Multisite solid-solution model for cation uptake in C-S-H

Calcium silicate hydrate (C-S-H) of variable composition is a major constituent of hydrated cements and concretes, determining their most relevant properties and durability. Furthermore, it is a main sorbent of cations and anions. C-S-H can incorporate Na, K, Al cations, Zn, as well as some actinides/analogs An (Th(IV), U(VI) [3]; Cm(III), Eu(III)) and fission products FP (Sr, Ba, Ra) relevant to radioactive waste disposal (Kulik and Kersten, 2001; Lothenbach and Nonat, 2015; Missana et al., 2018; Tits et al., 2014, 2003). Several C-S-H models have been developed mostly as simple ideal solid solution models (Bullard et al., 2016; Kulik, 2011; Myers et al., 2014). These simplified models describe the uptake of a few major cations, while they do not account properly for cations binding onto different specific structural sites, they are not incremental (i.e. adding new end-member(s) lead to re-parameterization of the whole model) and they do not describe accurately the uptake isotherms measured at different Ca/Si ratios (Kulik, 2011).

A new rigorous sublattice non-ideal solid solution model for C-S-H is being developed (CNKASH+), taking advantage of recent structural and atomistic views of C-S-H (Kunhi Mohamed et al., 2020, 2018). This model allows for accurate modeling of equilibrium solid- and pore-water composition in hydrated (blended) cement materials. The model is structurally consistent as it reproduces the impact of Ca/Si and alkali uptake on MCL (mean silicate chain length).

The model is based on a defect-tobermorite structure with 4 sublattice sites defined in the crystal structure: BT – bridging tetrahedral; IC – interlayer cation; IW – interlayer water; DU – dimeric unit / tobermorite). Based on the current knowledge on the C-S-H structure (Kunhi Mohamed et al., 2020, 2018) simultaneous substitutions of ion moieties (chemical species) or vacancies are allowed in the IC and BT sites. This makes it possible to describe the variable C-S-H composition and the uptake of different elements. The model is composed from several endmembers (charge neutral). Each end member contains one DU (fixed), IW (fixed), BT (exchange site) and IC (exchange site). The endmembers are constructed by considering possible combinations of elements being exchanged in the BT, and IC sites (with DU, and IW always having the same composition). For example, for the base C-S-H model (system Ca-Si-O-H) we allow Ca, Si and vacancy to be exchanged in the BT site and Ca and vacancy to be exchanged in the IC site. Considering all possible exchange combinations 6 endmembers can be constructed. For example,  $(\text{CaSiO}_3)_2\text{H}_2\text{O}]^0:\{\text{SiO}_2\text{OH}^-\}:\{\text{CaH}(\text{OH})_2^+\}:\{\text{H}_2\text{O}\}$  (DU:BT:IC:IW - template) is one of the five endmembers that has Si (represented by  $\{\text{SiO}_2\text{OH}^-\}$ , species with negative charge) in the BT site and Ca (represented by  $\{\text{CaH}(\text{OH})_2^+\}$ , species with positive charge) in the IC site. The composition (chemical formula) of the chemical species (moieties) is chosen such to yield a realistic non-gel water content at various Ca/Si ratios.

After generating all possible endmembers, initial thermodynamic properties are estimated from reactions with previous solid solution endmembers by assuming zero effect of reaction. The resulted initial estimates are in the range of  $\pm 50$  kJ/mol from the final values. The relative stability of different endmembers at given conditions (i.e. temperature, pressure, composition) defines the bulk properties of the modelled C-S-H phase. Besides the stability of each endmember the model takes into account possible non-ideal intra site interactions using the approach for non-ideal interactions of Berman (Berman, 1990; Berman and Brown, 1984). Regular binary interaction parameters can be set for each pair of elements substituting on one site. For example, an interaction parameter is set for Ca and Si substituting on the BT site. If this parameter has a large negative value (J/mol), this means that depending on the composition the presence of mixed endmembers with Ca and Si on the BT site in the C-S-H phase is more favorable than just based on their standard stability constants. Considering all possible interactions for all pairs of exchanging elements on each site, we get 4 possible interaction parameters for the base C-S-H model.

After constructing the model, the next step is the optimization of the endmember stabilities and the interaction parameters against critically selected experimental datasets covering wide range of system chemical composition. This is done using the GEMSFITS multi-parameter multi-property optimization tool (Miron et al., 2015). The parameters are generally optimized against reported aqueous and solid measured compositions. For the base C-S-H model, the reported mean silicate chain length (structural data) was also used. The model was subsequently extended with endmembers and interaction parameters for Na, K and Al. Based on spectroscopic and atomistic data, the model was extended such that alkalis can only substitute on the IC site, while Al can only be present on the BT site. The model can reproduce very well the experimental data for the uptake of alkalis and aluminum at different Ca/Si ratios and shows promising results for modeling the uptake of actinides and fission products (Kulik et al., 2018; Miron et al., 2018b).

The extension of the model can be done incrementally. The previous fitted parameters do not need to be reoptimized but can be taken as such from the previous step. The incrementality of the model paves the way for the efficient use of available sorption isotherms for further extensions of the CNKASH+ model to cover disposal-relevant applications of thermodynamic modelling of waste-cement interactions. One model will be able to describe the uptake of many cations and anions in a comparable manner with other complex phase solutions (e.g. aqueous phase).

The uptake of ferric iron was recently studied by Mancini et al. (2020a) using wet chemistry and spectroscopic techniques. Measured at different Ca/Si ratios of C-S-H and pH the uptake of iron showed a linear trend with no significant differences within the experimental scatter. Based on the spectroscopic data, at Ca/Si ratios of 1.2 and 1.5, iron was found to replace Ca in the interlayer of the C-S-H phase, while at Ca/Si ratio of 0.8 a secondary phase on the surface of C-S-H was assumed to be forming. Compared with the uptake of Al(III) at the same metal concentrations the uptake of Fe(III) is shown to be significantly stronger (~0.9 log units). In the scope of this project, the C-S-H model will be extended for the uptake of Fe(III) and Fe(II), using newly acquired experimental data at PSI (Mancini et al., 2020a/b).

To be able to use the newly developed CNKASH+ model in geochemical calculations, the modeling software needs to be able to handle multisite solid-solution models with Berman type regular non-ideal interaction parameters. Currently, the model works and is only available through the GEM-Selektor geochemical modeling suite (Kulik et al., 2013; Wagner et al., 2012). Simplifications such as model discretization should be investigated for using it in other codes (see section 2.3.3).

### 2.3.2 Fe containing AFm (monosulfate) and AFt (trisulfate) solid solutions

In the absence of silica, Ca-Al-Fe-OH system, depending on the presence of sulfate and/or carbonate, the ferrite (C2(A,F)) clinker phase will react to form Fe(III)-containing ettringite, monosulfate or monocarbonate. Experimental data have shown that solid-solutions where Al(III) is substituted by Fe(III) are forming for ettringite, monosulfate, and hemicarbonate (Dilnesa, 2012; Dilnesa et al., 2012, 2011; Möschner et al., 2009, 2008). In the case of Al/Fe-monosulfate and Al/Fe-trisulfate (ettringite) solid solutions miscibility gaps were observed, with two phases coexisting depending on the Al/Fe composition. To have a description of the miscibility gap and an accurate representation of the solid and aqueous composition, the solid solutions can be treated as non-ideal binary mixtures using the Redlich-Kister (Guggenheim) mixing model (Glynn, 2019):

$$G_{ex} = RT \sum_i X_i \ln \gamma_i = RT(X_1 \ln \gamma_1 + X_2 \ln \gamma_2) \quad (2-3)$$

with  $\ln \gamma_1 = X_2^2(a_0 + a_1(4X_1 - 1))$  and  $\ln \gamma_2 = X_1^2(a_0 - a_1(4X_2 - 1))$ .

The term  $G_{ex}$  is the excess Gibbs energy,  $X_i$  is the mole fraction and  $\gamma$  is the activity coefficient of endmember  $i$ ,  $R$  is the universal gas constant,  $T$  is the temperature and  $a_0$  and  $a_1$  are the dimensionless Guggenheim parameters.

The solid-solution between Al- and Fe-ettringite was experimentally investigated by Möschner et al. (2009). They synthesized samples from 0 to 1 Al/(Al + Fe) molar ratio and analysed the solid-solution as well as the aqueous composition. Additional calcite and iron hydroxide phases were formed during the experiments. The XRD analysis showed the existence of a miscibility gap between 0.3 and 0.6 molar ratio. This was finally modelled assuming a nonideal solid solution with a miscibility gap ( $a_0 = 2.10$  and  $a_1 = -0.169$ ).

The Al/Fe-monosulfate solid solution was experimentally studied by Dilnesa et al. (2012). Samples were synthesized by varying the Al/(Al + Fe) ratio from 0 to 1. From 0 to 0.45 a single solid-solution phase was observed while for 0.45 to 0.95 the presence of two (Al,Fe)-monosulfate solid solution phases was detected. Their experimental data could be modelled assuming a nonideal solid solution with a miscibility gap ( $a_0 = 1.26$  and  $a_1 = 1.57$ ). In all experiments portlandite and iron-hydroxide were identified. Fe-monosulfate was found to be stable up to 80 °C after which it destabilizes with respect to portlandite and Fe-oxide/hydroxide. In the presence of gypsum Fe-ettringite was identified to be more stable than Fe-monosulfate, up to 40 °C, while above 40 °C in the presence of gypsum Fe-monosulfate was identified to be more stable.

Although miscibility gaps were clearly identified by XRD analysis, considering the scatter in the measured solubility of (Al, Fe)-monosulfate and -ettringite solid solutions the use of ideal solid solutions

for simplification of the modelling process seems reasonable and well within the experimental uncertainty. The impact of using ideal or non-ideal solid solutions on the modelled aqueous and solid composition will be further investigated.

### 2.3.3 Discretization of Fe solid solution data for reactive transport model

Incorporation of complex non-ideal solid solutions in reactive transport modeling is not very wide spread, in part due to the lack of implemented solid solution models in the coupled chemical equilibrium calculation codes, the numerical stability and robustness of the calculations and the increase in the computational time. Rather than having the actual solid solution model implementation and the full spectrum of the continuously variable composition, a discrete set of stoichiometric solids over a selected compositional space can be used instead. The solids will form depending on the system composition as discrete pure phases. The number of discrete phases determines how accurate are the properties of the solid solution approximated and should depend on the degree of change in the properties with the change in composition. Lichtner and Carey (Lichtner and Carey, 2006) propose a methodology of discretizing solid solution for being incorporated into reactive transport models. This is applied as an example by Carey and Lichtner (2007) who discretized the C-S-H solid solution into 100 (arbitrary) discrete phases. In other cases, only a small number of discrete compositions were used. Walker et al. (2016) derive a discrete solid phase (DSP) C-S-H model from a binary non-ideal solid solution model. The discrete phases were generated by Ca/Si ratio increments of 0.05 from 0.55 to 1.65, having a total of 12 C-S-H phases and their stability constants were derived from the binary non ideal solid solution model. The DSP model can satisfactorily describe the experimental data (system Ca-Si-H<sub>2</sub>O), with a stepped appearance (depends on the discretization increments) but does not account for the uptake of other elements.

A new structurally consistent multisite non-ideal solid solution model has been proposed that is incrementally extended to considered the uptake of different cations (e.g. alkalis, aluminum, iron, etc.) (Kulik et al., 2018; Miron et al., 2018b) (see section 2.3.1). This model could be used to derive a discrete phase C-S-H model starting from the same structural and compositional considerations that were used in the non-ideal solid solution model. Discrete phases can be derived by considering intermediate composition from the existing endmembers of the solid-solution model. The model contains 4 sites (DU – dimeric unit, BT – bridging tetrahedral, IC – interlayer cation, IW – interlayer water) and it is assumed that the exchange of elements can happen only in the BT and IC sites. The stoichiometric factor for each site is constrained to 1. Considering changes in the stoichiometry of a moiety in each site from 0 to 1, the discrete phases of intermediate composition can be generated as shown in

Table 1.

Table 1 – C-S-H model sites with their respective moieties (species), [mole amount], and constraints for generating discrete phases.

**DU** : T (CaSiO<sub>3</sub>)<sub>2</sub>H<sub>2</sub>O = 1 (fixed)

**IW**: h H<sub>2</sub>O = 1 (fixed)

**BT**:

S (SiO<sub>2</sub>OH<sup>-</sup>) = [0,1]

C (CaOOH<sup>-</sup>) = [0,1]

A (Al(OH)<sub>4</sub><sup>-</sup>) = [0,1]

... (other elements)

**IC**:

C (CaH(OH)<sub>2</sub><sup>+</sup>) = [0,1]

N (NaH(OH)<sup>+</sup>) = [0,1]

K (KH(OH)<sup>+</sup>) = [0,1]

F (Fe(OH)<sub>2</sub><sup>+</sup>) = [0,1]

... (other elements)

constraints

v (OH<sup>-</sup>) = 1-C-S-A- ...

v (H<sup>+</sup>) = 1-C-N-K-F ...

$$0 \leq S+C+A+\dots \leq 1$$

$$0 \leq C+N+K+F\dots \leq 1$$

Formulas in parenthesis represent moieties (species) that can be exchanged in the given sites, and the square brackets defines the interval (mole) for generating the intermediate composition for the discrete phases. For each new discrete phase, we can calculate the stability constant from the chemical potential of the of the non-ideal solid solution phases with the same composition.

For example, in the system Ca-Si-OH, we allow C, S, and vacancy (v) to be exchanged in the BT site and C, and vacancy (v) to be exchanged in the IC site. Taking into account changes in the amount of C, S, and v from 0 to 1 (in IC, and BT) with a chosen step size of 0.25, 75 discrete compositions are generated, while for a step size of 0.5 only 18 discrete phases are necessary having a composition as follows (in bold font are the original endmembers) in Table 2.

Table 2 – Example of discretized simple C-S-H solid solution into 18 discreet phases using a 0.5 compositional step size for Ca I, Si (S) and vacancy (v).

**T:v<sub>1</sub>:v<sub>1</sub>:h**

T:v<sub>1</sub>:C<sub>0.5</sub>, v<sub>0.5</sub>:h

**T:v<sub>1</sub>:C<sub>1</sub>:h**

T:C<sub>0.5</sub>, v<sub>0.5</sub>:v<sub>1</sub>:h

T:C<sub>0.5</sub>, v<sub>0.5</sub>:C<sub>0.5</sub>, v<sub>0.5</sub>:h

T:C<sub>0.5</sub>, v<sub>0.5</sub>:C<sub>1</sub>:h

**T:C<sub>1</sub>:v<sub>1</sub>:h**

T:C<sub>1</sub>:C<sub>0.5</sub>, v<sub>0.5</sub>:h

**T:C<sub>1</sub>:C<sub>1</sub>:h**

T:S<sub>0.5</sub>, v<sub>0.5</sub>:v<sub>1</sub>:h

T:S<sub>0.5</sub>, v<sub>0.5</sub>:C<sub>0.5</sub>, v<sub>0.5</sub>:h

T:S<sub>0.5</sub>, v<sub>0.5</sub>:C<sub>1</sub>:h

T:S<sub>0.5</sub>, C<sub>0.5</sub>:v<sub>1</sub>:h

T:S<sub>0.5</sub>, C<sub>0.5</sub>:C<sub>0.5</sub>, v<sub>0.5</sub>:h

T:S<sub>0.5</sub>, C<sub>0.5</sub>:C<sub>1</sub>:h

**T:S<sub>1</sub>:v<sub>1</sub>:h**

T:S<sub>1</sub>:C<sub>0.5</sub>, v<sub>0.5</sub>:h

**T:S<sub>1</sub>:C<sub>1</sub>:h**

Adding additional elements and having a small step size will dramatically increase the number of discrete compositions. It is expected that the step size does not have to be the same for all elements and for all composition intervals. A smart discretization procedure is necessary for producing the optimal number of discrete phases that satisfactorily approximate the non-ideal solid solution model.

## 2.4 First results and discussion

### 2.4.1 Parameterization of Fe uptake in C-S-H

The new C-S-H non-ideal solid solution model (CNKASH+) is currently being extended for the uptake of ferric iron. Here, we present preliminary results on the parametrization of the model against the experimental data of Mancini et al. (2020a). Synchrotron-based investigations presented in Mancini et

al. (2020a) suggest that the preferred structural position of iron in C-S-H is the interlayer for the high C/S ratio while at low C/S ratio a separate phase is considered. We extend the CNK(A)SH+ model by assuming that iron can only be exchanged in the IC sites. Three iron bearing endmembers are defined using the  $\text{Fe}(\text{OH})_2^+$  (F) moiety (species) in the IC site, as detailed in *Table 3*.

*Table 3 – Iron bearing endmembers for Fe uptake in C-S-H.*

	endmember code				chemical formula
	DU:	BT:	IC:	IW	
1	T:	S:	F:	h	$(\text{CaSiO}_3)_2\text{H}_2\text{O}:\text{SiO}_2\text{OH}:\text{Fe}(\text{OH})_2^+:\text{H}_2\text{O}$
2	T:	C:	F:	h	$(\text{CaSiO}_3)_2\text{H}_2\text{O}:\text{CaOOH}:\text{Fe}(\text{OH})_2^+:\text{H}_2\text{O}$
3	T:	v:	F:	h	$(\text{CaSiO}_3)_2\text{H}_2\text{O}:\text{OH}:\text{Fe}(\text{OH})_2^+:\text{H}_2\text{O}$
4	T:	A:	F:	h	$(\text{CaSiO}_3)_2\text{H}_2\text{O}:\text{Al}(\text{OH})_4^-:\text{Fe}(\text{OH})_2^+:\text{H}_2\text{O}$

Initial estimates for the stabilities (Gibbs energy of formation) of these endmembers are computed from reactions with existing C-S-H endmembers of the base CSH model by replacing vacancy with iron in the IC site. For example, initial estimates for TSFh are calculated from:

$\text{TSvh} + \text{goethite} (\text{FeOOH}) = \text{TSFh}$ , assuming that all the reaction effects are zero. The resulted estimate should be around  $\pm 50$  kJ from the final value.

In addition to the defined endmembers, the model considers 4 interaction parameters. These are for the possible non ideal interactions on the interlayer site between Fe and Ca, Fe and vacancy, Fe and Na, and between Fe and K.

The stabilities of endmembers and the interaction parameters are then optimized against the measured equilibrium iron composition of the aqueous and solid C-S-H phase reported by Mancini et al. (2020a). Because the experiments were done in the system Ca-Si-Na-OH-Fe (no aluminum), only the properties of the first three endmembers and the first three interaction parameters can be retrieved.

Preliminary fits to the experimental data show that the model can describe very well the experimental data (Figure 4) at different C/S and pH (different NaOH solution concentration). The model can incorporate the uptake of iron both at low and at high C/S ratios, without the need to define a separate phase.

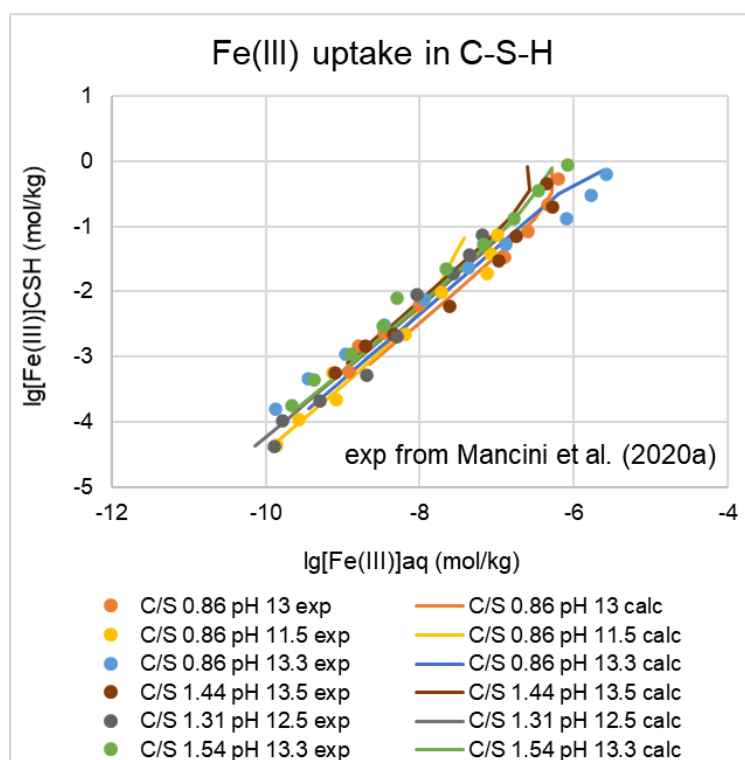


Figure 4 – Uptake on Fe in C-S-H at different C/S ratios in C-S-H and pH values. Circles, experimental data from Mancini et al. (2020a) and lines, calculated values using the optimized properties of endmembers and values for the interaction parameters.

For the model to be complete one additional endmember (in the presence of aluminum) and the value for the interaction parameter between Fe and K are necessary. From previous experience when fitting the alkali uptake, the values of Na and K interacting with other elements in the IC site are remarkably similar. Therefore, we can assume that the value for interaction parameter between Fe and K is equal to that of the interaction parameter between Fe and Na.

For the additional endmember when aluminum is exchanged in the BT site and iron is being exchanged in the IC site (TAFh), experimental data for the uptake of iron in the presence of aluminum would be needed. Ways of estimating the stability of endmembers to avoid the need of additional experiments are being investigated.

### 3. Literature data on the kinetic rates of steel corrosion

*MINES ParisTech, IRSN and Subatech*

The second chapter has provided an overview of relevant aspects related to the thermodynamics of formation of iron bearing cement as well as the nature of the corrosion products under disposal conditions, with an emphasis on cementitious materials. However, the metallic iron in low carbon or weakly alloyed steels is never under equilibrium in contact with aqueous solutions, both under oxic and anoxic redox conditions. It will be subjected to several types of corrosion processes, such as generalized (uniform) corrosion or localized corrosion (e.g. pitting corrosion). Therefore, the correct modeling of generalized iron corrosion requires to implement a kinetic control on corrosion. The experimental characterization of such steel corrosion rates for the binary iron/cement system is a main objective of the Subtask 2.2.

The objective of this chapter is to give an overview of steel generalized corrosion rate under conditions of interest for the experiments performed in Subtask 2.2. That is to say in the environment of low-pH and high-pH cementitious materials. The corrosion in clay media is also given in a first section for comparison and since it may be applicable to some extent to the in situ experiment of cement/bentonite grout in the Tournemire claystone (e.g. Fe-silicates precipitates).

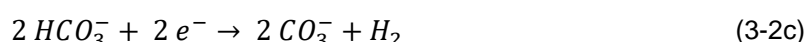
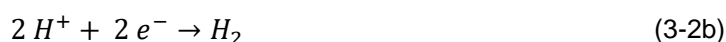
#### 3.1 Main (electro)chemical processes

The present report will focus on the generalized corrosion of iron under anoxic and fully water saturated conditions. The process usually corresponds to the development of a dense product corrosion layer, resulting into a passive corrosion stage in which the dissolution rate of this dense layer is equal to the corrosion rate. Such corrosion can be influenced by a number of factors as temperature, saturation and radiation gradients, presence of corrosion-aggressive species (chloride, sulphate, thiosulphate), and presence of microbes.

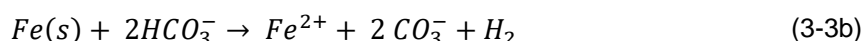
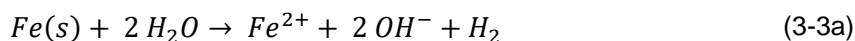
Metallic iron is never in equilibrium with water under anoxic conditions. The anodic reaction writes as:



whereas several cathodic reactions can co-exist:



These reactions lead to the flowing mass balance equations:



that are both controlled by kinetics.

#### 3.2 Fe-corrosion rate laws in neutral pH argillaceous media

Using published data and data generated by CEA and EDF in representative repository conditions, two empirical rate laws have been determined for the iron corrosion under anoxic conditions with respect to the temperature (*Féron et al., 2008*). The first relation is representative for the rather short time (as found in the BACUCE experiment) between 0.5 and 15 years (T in K):

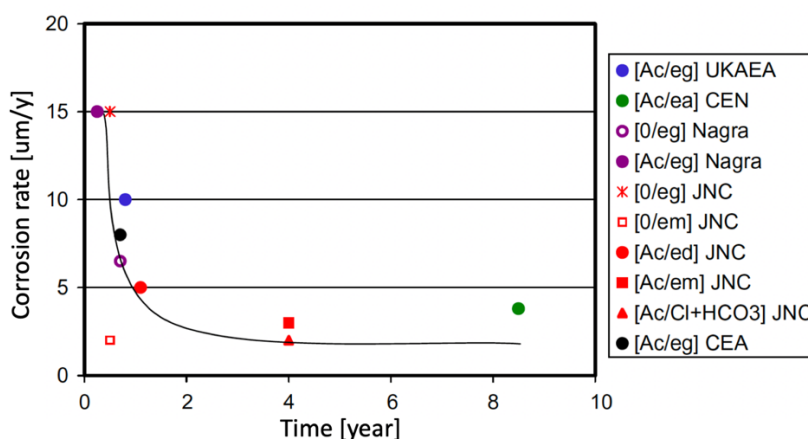


Figure 5– Evolution of average generalized corrosion rate of carbon steels as a function of time in fairly reducing conditions in different types of clayey water chemistry at 80°C (Féron et al., 2008).

$$\text{rate (mm.y}^{-1}\text{)} = 0.364 e^{-1300/T} \quad (3-4a)$$

whereas the second law accounts for the time frames beyond 10 years:

$$\text{rate (mm.y}^{-1}\text{)} = 0.162 e^{-1300/T} \quad (3-4b)$$

At 80°C, the temperature of reference for Subtask 2.2, these two rates are 9 µm/y and 4 µm/y, respectively. Such rate values are in good agreement with another compilation of data reported in Féron et al. (2008) on the evolution of average generalized corrosion rate of carbon steels as a function of time in fairly reducing conditions in different types of clayey water chemistry at 80°C (Figure 5). One notes on Figure 5 the exponential type decrease over the first years.

After 400 days at 60°C Chautard (2013) found a rate of 1 µm/y for iron in contact with the synthetic water of the Toarcian argillite from the Tournemire URL and 10 – 15 µm/y when the iron material was embedded in the argillite. As shown in Figure 6, there was a layered zonation of corrosion products around the metallic iron rod embedded in the argillite with Fe-carbonate corrosion products (chukanovite and siderite). Iron silicate corrosion products (as greenalite) were also identified but in a low content, whereas iron-sulfide (mackinawite) only after inoculation of bacteria in the system. Preliminary HYTEC modeling showed the coupled effects of OH<sup>-</sup> source due to Fe corrosion close to the iron rod and carbonate diffusion from the argillite. The location and thicknesses of the corrosion product layers were strongly dependent on the value assigned to the effective diffusion coefficient  $D_e$  inside these corroded layers. The domain of relative stability of these secondary products are reported in the Pourbaix diagrams of Figure 7. Magnetite can exist over a rather wide range of pH, contrarily to siderite than is more localized (at least under the Toarcian argillite geochemical conditions). The left-hand side of the diagrams corresponds to the corrosion domain where Fe(II) and Fe(III) are soluble, magnetite typically corresponds the passivation domain, whereas immunity is gained at very low reducing conditions (which are, however, below the water stability limit; i.e. iron is not stable in water).

At 90°C, de Combarieu et al. (2007, 2011) found a similar tendency with the Callovo-Oxfordian claystone leading to a corrosion rate of 1.5 µm/y in batch and 15 – 30 µm/y in an integrated experiment (where the iron foil was in close contact with the claystone). The occurrence of slightly higher rates at 90°C than 70°C is in agreement with an activation energy of iron corrosion that is relatively low, about 15 kJ.mol<sup>-1</sup> (Ferron et al., 2008).

Necib et al. (2016) performed an in situ experiment of steel corrosion under anoxic conditions at 85°C in the Bure URL. In a test chamber drilled in the Callovo-Oxfordian clayey rock, carbon steel samples were exposed to the clayey porewater. Two different regimes of corrosion were measured, an active behavior (200 µm/y) and passive behavior (< 30 µm/y). The higher rate could be explained by the presence of an acidic pH transient (pH ~ 4.5) that lasted for 200 days. The transient state led to the precipitation of Fe-hydroxychloride at the interface with the metal, which prevented any efficient passivation. The experiment of Necib et al. (2016) is worth to be mentioned in the context of the ACED task 2 since the French HLW repository concept had been modified by adding a cement-bentonite based grout between the host rock and steel liner. This is expected to neutralize the potential acidity and bring the C-steel surface to the passivity domain.

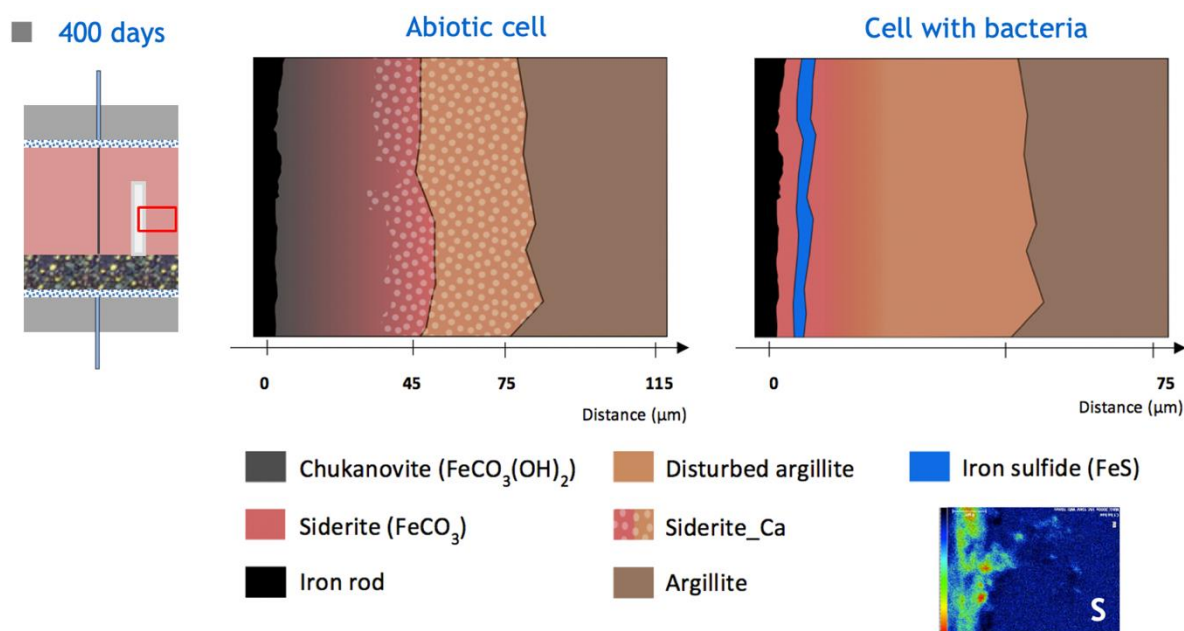


Figure 6 – Layered zonation of corrosion products around a metallic iron rod embedded in the Toarcian argillite of Tournemire after 400 days at 60°C (Chautard et al., 2013).

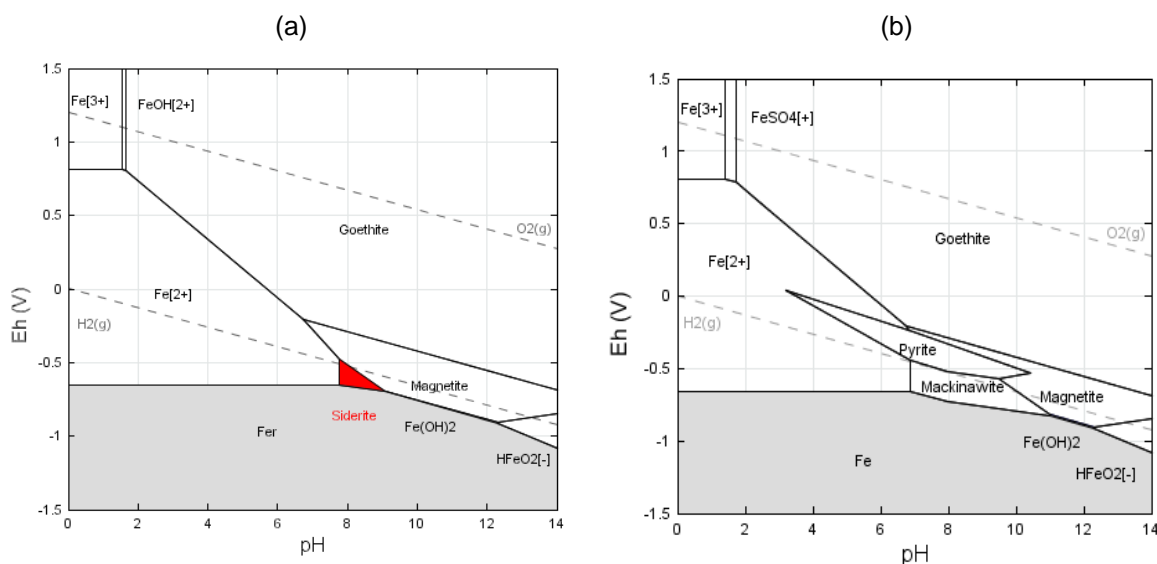


Figure 7 – Speciation of iron corrosion products calculated with the Thermoddem database at 60°C for (a) iron oxyhydroxides and carbonates and (b) iron oxyhydroxides and sulfides; Fe conc. = 10<sup>-5</sup> M, act. HCO<sub>3</sub><sup>-</sup> = 10<sup>-3</sup>, SO<sub>4</sub> conc. = 10<sup>-4</sup> M, excluding hematite; the dotted lines correspond to the stability limits of water.

### 3.3 Fe-corrosion rate laws under high-pH alkaline conditions

In a cement-based geological disposal concept, the followed strategy is usually to demonstrate that localized corrosion phenomena cannot occur in highly alkaline disposal conditions (Deissmann et al., 2020). The corrosion rates of low carbon steel under high pH value found in CEM I chemical and anoxic environment are very low (about 0.1  $\mu\text{m}/\text{y}$ ) due to passivation by the formation of compact magnetite film or layer uniformly over the whole surface of iron (Yu et al., 2012; Kursten et al., 2015; Swanton et al., 2015; Smart et al., 2017b). This protective nature of the passive state is associated to a marked decrease in the ionic conduction in the film (ion barrier) from a electrochemical point of view.

The report of Deissmann et al. (2020) provides for a compilation of uniform corrosion rate of low alloyed steels in anoxic, highly alkaline and chloride-free solutions. That is to say relevant conditions for most of the materials experimentally studied in Subtask 2.2. The corrosion rate increases weakly to moderately as temperature increases according to the Arrhenius relationship. At high pH values, this temperature dependency is clearly relevant for the initial corrosion rate of carbon steel (Figure 8), but it seems to be inoperative for the long-term corrosion rates (Figure 9).

Figure 10 shows a decreasing tendency of the corrosion rate with increasing time of exposure towards a constant and very low value. Long-term corrosion rates (beyond one year) in the range of 0.1  $\mu\text{m}/\text{y}$  or lower have been reported for temperatures up to 80°C.

The passive state is maintained in reinforced concrete structures for a very long time, but may be lost when chloride ions reach the steel. Chloride-induced depassivation has been associated with a change of the oxidation state of the inner part of the passive film leading to breakdown of the film (Angst et al., 2017).

The report of Neeft et al., (2020) also points out that negatively charged dissolved iron under high pH conditions can be sorbed on cement minerals which are positively charged at a pH between 12 and 13. Consequently, cement phases can reduce the dissolved iron concentration and thereby increasing generalized corrosion rates of carbon steels.

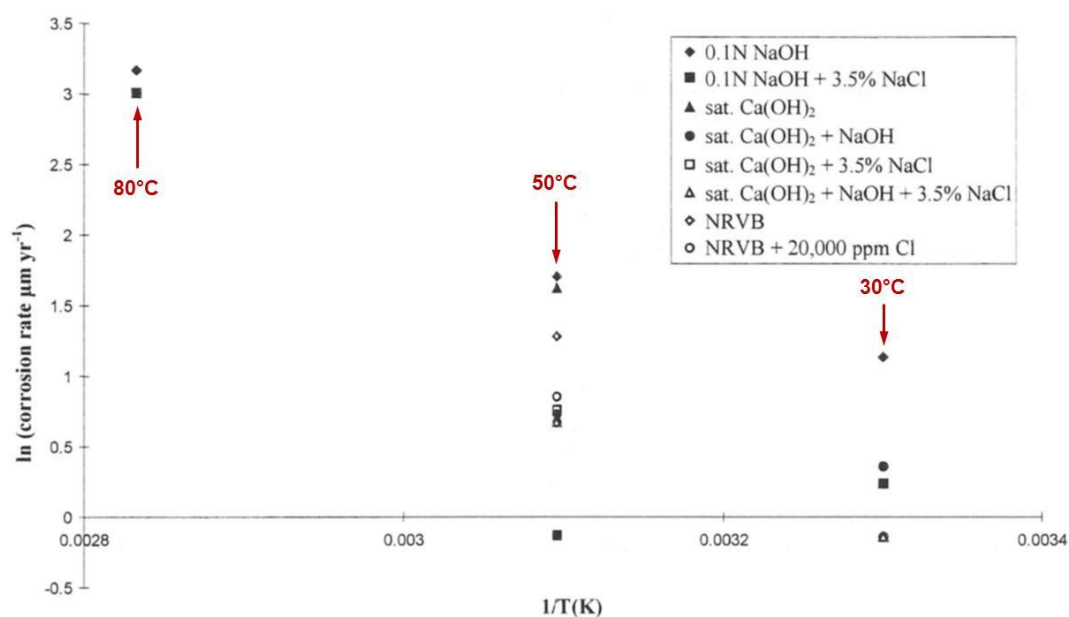


Figure 8– Effect of temperature on the initial anaerobic corrosion rate of carbon steel in various alkaline (basic) solutions. The anaerobic corrosion rate is plotted as a function of reciprocal temperature (adapted from Smart et al., 2004; see Deissmann et al. (2020) for all details).

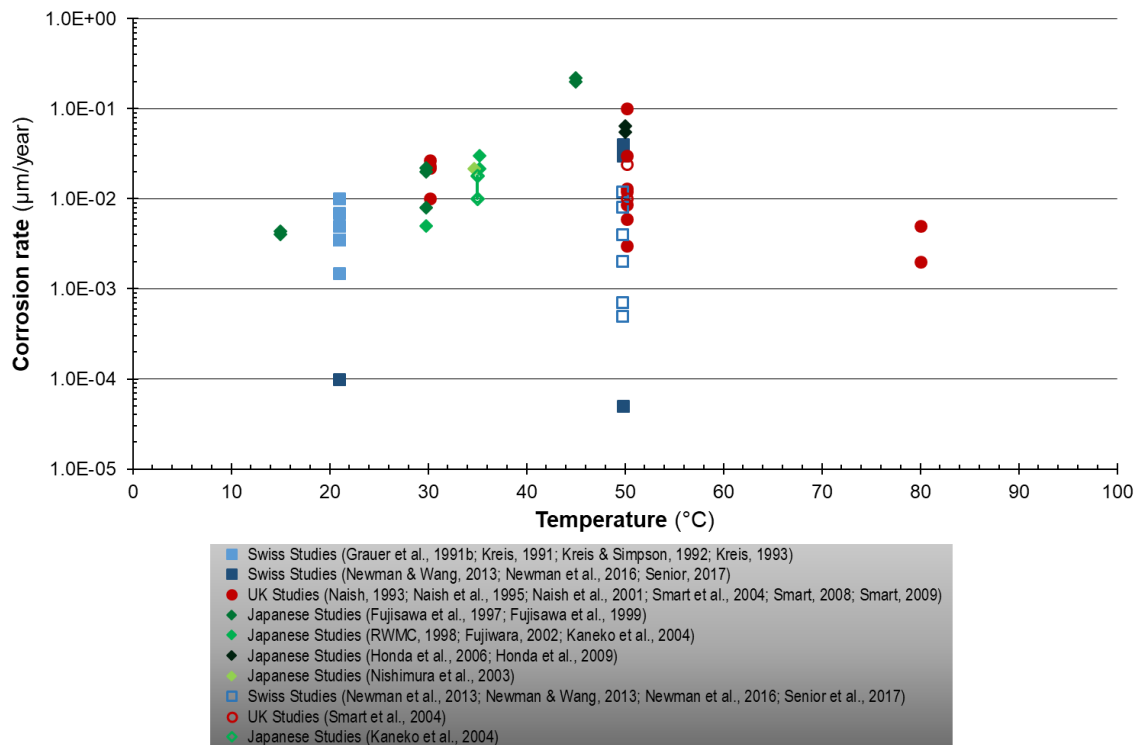


Figure 9 – Effect of temperature on the long term ( $t > 365$  days) uniform corrosion rate of carbon steel exposed to alkaline and anoxic environments (see Deissmann et al., 2020 for all details). Closed symbols represent tests conducted in solutions; open symbols represent tests conducted in cement.

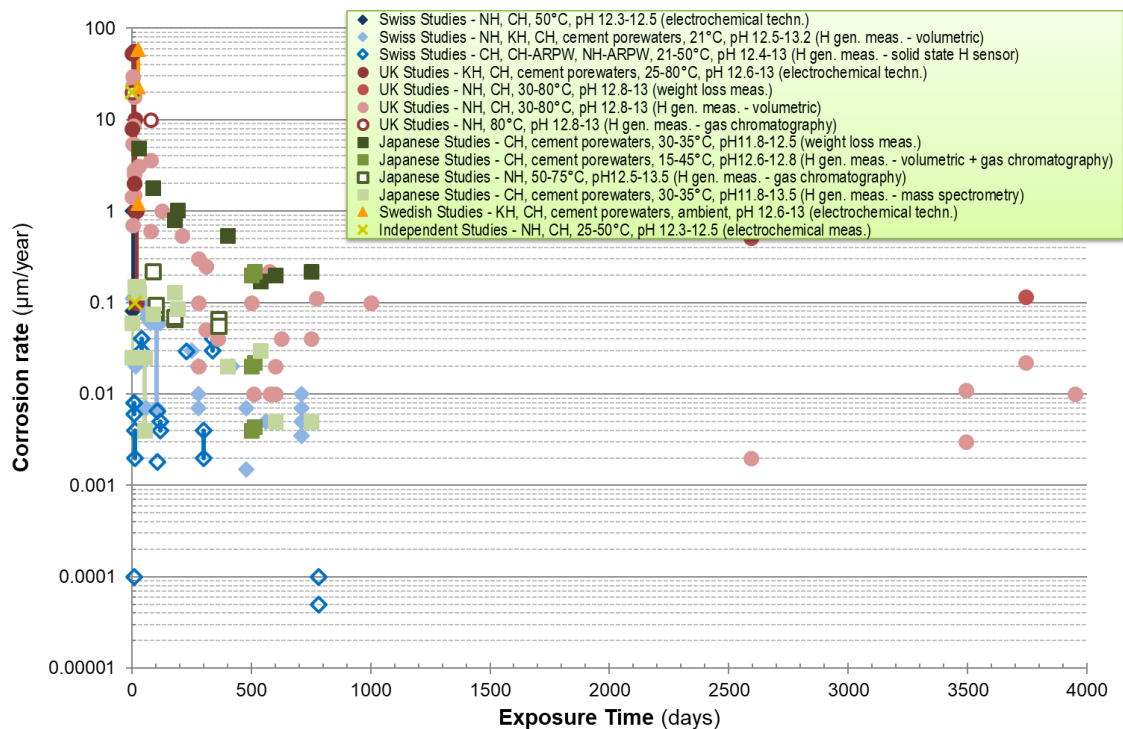


Figure 10 – Compilation of uniform corrosion rates (reported in the non-nuclear industrial and nuclear waste management literature) of carbon steel in anoxic and alkaline chloride-free solutions (pH 12 – 13.5); see Kursten et al. (2015) and Deissmann et al. (2020) for further details.

### 3.4 Fe-corrosion rate laws under low-pH alkaline conditions

The passivation of the steel by magnetite may become inactive when the alkaline pH decreases below 10.5 and the corrosion rate increase by a factor of 50 (about 5  $\mu\text{m}/\text{y}$ ). However, the corrosion rates under moderately alkaline pH (10.5 – 11.5) are not well characterized yet. Only a very few studies are available in the literature (Bodén and Pettersson, 2011; García Calvo et al., 2013). The Subtask 2.2 of ACED will bring some new insights on corrosion in contact with the chemical environment of low-pH cement (Figure 11), useful for the Task 4 long-term modeling.

Bodén and Pettersson (2011) studied the corrosion of steel in low-pH concrete ( $\text{pH} \leq 11$  in the leachate) in the ESDRED project for the development of rock bolt grout and shotcrete for rock support in underground disposals. Their corrosion investigations did not indicate any significantly increased corrosion rates in low-pH concrete in chloride free solutions. The steel bars in untreated specimens, concrete with no chlorides, had an average corrosion rate of 12.0  $\mu\text{m}/\text{year}$  for low-pH concrete and 12.5  $\mu\text{m}/\text{year}$  for CEM I concrete. However, it is worth noting that such corrosion rates are much higher than usually reported for CEM I concrete (corrosion rate about 0.1  $\mu\text{m}/\text{year}$ , see previous section), which requires to be cautious about the findings of this pioneering study on steel corrosion in low-pH cement.

García Calvo et al. (2013) investigated the corrosion of carbon steel reinforcement in low-pH cement mortars based on OPC plus silica fume and/or fly ashes. A second mortar made of OPC cement only was also studied as a reference. The low pH pore solution had a clear detrimental influence on the corrosion of steel reinforcement. Low values of corrosion current density with decreasing tendency were registered, indicating the formation of a passive layer in both mortar mixes (Figure 12). However, in the case of the low pH mortar, a significant increase of corrosion current by one order of magnitude was detected after 25 days of exposure, when the pore water pH was lower than 11.8 (Figure 12). After this time, the current was maintained above the limit considered for passivation. This fact is associated with the initiation of an active corrosion process with periods of passivity and reactivation, probably because the pH is at the limit between the active/passive states.

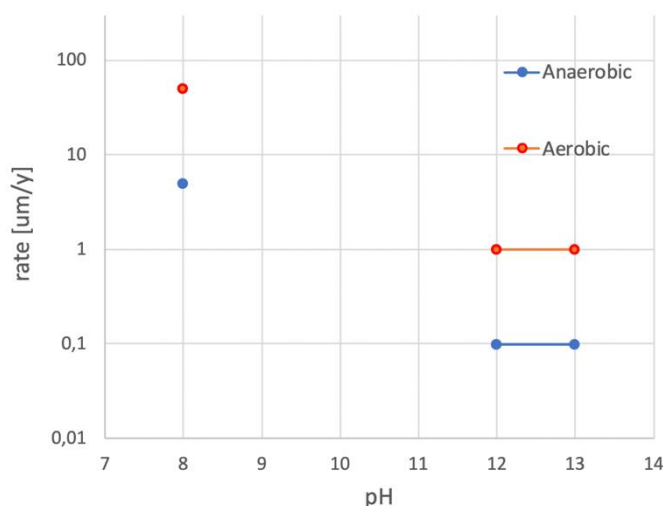


Figure 11 – Long-term corrosion rates of carbon steel under aerobic and anaerobic conditions selected for the reactive transport modeling in Task 4 of ACED; there is a gap in the data between neutral pH and high pH values.

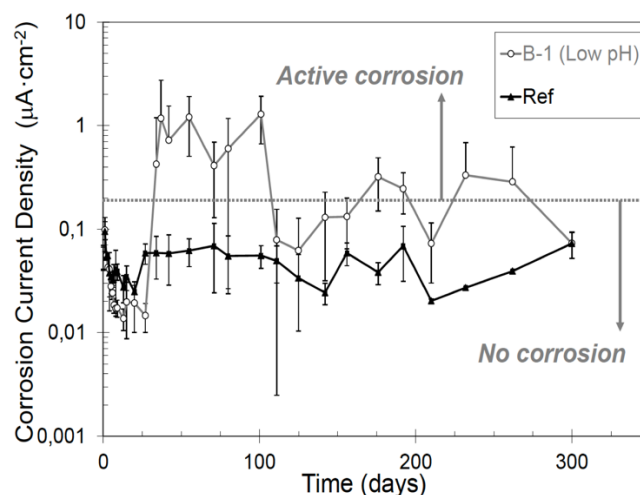


Figure 12 – Corrosion current density evolution during the corrosion of carbon steel reinforcement in a low-pH cement mortar and in a OPC cement mortar as reference (García Calvo et al., 2013).

### 3.5 Mill-scale effect on steel corrosion rate

The surface of manufactured steel is generally covered with an oxide layer called mill-scale that forms at high temperature (above 570°C) during the hot rolling process of the steel. This layer is principally composed of wüstite (FeO) and can also contain magnetite (Fe<sub>3</sub>O<sub>4</sub>), hematite (α - Fe<sub>2</sub>O<sub>3</sub>) and maghemite (γ - Fe<sub>2</sub>O<sub>3</sub>) (Angst et al., 2017). Due to the presence of crevices and cracks in the structure of this layer, it offers far less protection against corrosion (Angst et al., 2017). In fact, this surface can enhance the corrosion rate due to its detrimental influence on the formation of a passivating film at the surface of the steel (Mahallati and Saremi, 2006).

Generally, corrosion experiments are conducted on prepared samples (polished and/or pickled), on which this mill scale layer is removed to avoid any effect of this layer on the corrosion rate measurements. But it will not be the case neither in the BACUCE experiment, nor in a real disposal site. In addition, it is worth mentioning that the surface finish of steel has also an influence on its resistance to corrosion and in fine the corrosion rate. For example, Mammoliti et al. (1996) demonstrated that the steel surface finish (as received and degreased, grounded and degreased or polished and degreased) as a major influence on the [Cl<sup>-</sup>] threshold to initiate corrosion. “Scalping” a steel tube leads to a rough surface that can enhance corrosion rate.

These mill-scale effects will be characterized in the environment of CEM I cement and the bentonite/cement grout at 80 °C (see Sec. 5.1.3).

#### Take away:

The anoxic generalized corrosion rates of carbon steel under high pH condition as in CEM I concrete are well known and very low (< 0.1 µm/y). The rates are slightly increased while temperature shifts from 20°C to 80°C. The anoxic generalized corrosion rates of carbon steel in the weakly to moderate alkaline pH domain (pH 9.5 – 11) are still poorly know, especially at high temperature (e.g. 80°C). They could be in the range of corrosion in clay media, i.e. 10 µm/y or more.

## 4. Mathematical modeling and HYTEC code

*MINES ParisTech*

The modeling of the in situ and lab experiments of Subtask 2.2 (see Chapters 5 and 6) will be performed with the reactive transport code HYTEC (van der Lee et al., 2003). This section gives the main chemical and physical mathematical laws that have been implemented in HYTEC, whereas some key information on the numerical approaches and databases are provided in a subsequent section.

### 4.1 Reactive transport equation

The HYTEC formulation of the multicomponent reactive transport equation under water saturated conditions considering only diffusion is:

$$\frac{\partial \varepsilon C_i}{\partial t} = \nabla \cdot (D_e \nabla C_i) - \frac{\partial \varepsilon \bar{C}_i}{\partial t} \quad (4-1)$$

where  $C_i$  and  $\bar{C}_i$  are respectively the mobile and immobile concentrations of an element  $i$  per unit volume of solution [mol/L],  $\varepsilon$  is the porosity of the material. The partial derivative term  $-\frac{\partial \varepsilon \bar{C}_i}{\partial t}$  is driven by chemical reactions whereas the other terms represent transport processes. The term  $D_e$  [m<sup>2</sup>/s] is the effective diffusion coefficient ( $D_e = \varepsilon D_p$  where  $D_p$  is the pore diffusion coefficient).

Actually, the porosity is subjected to change in time and space due to geochemical processes such as dissolution or precipitation (opening and clogging of the pore space). The change in porosity can be calculated by HYTEC from the evolution of the mineral concentrations in the system, knowing their molal volume or density. The empirical Archie's law is easy to implement in reactive transport models and applicable to a wide range of materials:

$$D_e = D_e(\omega_0) \left( \frac{\omega - \omega_c}{\omega_0 - \omega_c} \right)^m \quad (4-2)$$

where  $\omega_0$  is the initial porosity,  $\omega_c$  is a critical porosity threshold under which diffusion stops and  $m$  is an empirical Archie's coefficient.

The full set of non-linear equations of thermodynamic equilibrium is numerically solved according to the basis component approach and its matrix-algebra, using an improved Newton-Raphson scheme. The transport module is based on the representative elementary volume (REV) approach with finite volume calculation. HYTEC handles 1D – 3D grids in cartesian coordinates as well as 1D in radial and 2D in cylindrical (axis symmetric) coordinates

HYTEC searches for an accurate solution to the multicomponent transport problem using an iterative, sequential, so-called strong coupling scheme. Strong coupling permits variable hydrodynamic parameters as a function of the local chemistry (*Figure 13*). For example, the porosity of a porous medium decreases after massive precipitation of newly formed mineral phases, which modifies the water flow paths and transport parameters, e.g., diffusion coefficients.

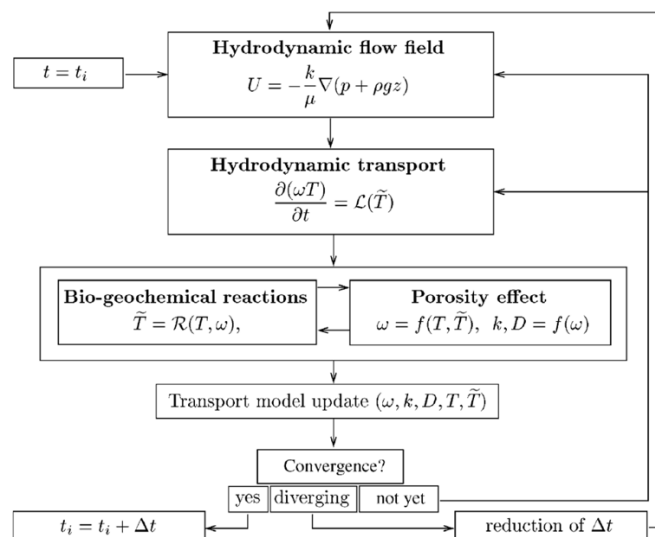


Figure 13 – Diagram of consecutive actions within one timestep as implemented by HYTEC.  $T$  denotes total concentrations,  $\tilde{T}$  mobile concentrations,  $L$  transport operator (hydrology) and  $R$  reaction operator (chemistry).

## 4.2 Thermodynamic equilibrium

The geochemical module of HYTEC simulates the chemical equilibrium state of complex aqueous systems, including minerals, organics, colloids and gases. Chemical processes as aqueous speciation, precipitation/dissolution of solid phases, and sorption (surface complexation with electrostatic correction, ion exchange) are accounted for. The aqueous chemistry includes acid/base reactions, oxidation and reduction (redox) processes and aqueous complexation by organic and inorganic ligands. HYTEC uses a mixed kinetic-thermodynamic equilibrium approach.

### 4.2.1 The mass balance equation

The thermodynamic equilibrium state of the chemical system is calculated according to the usual mass action equation:



$$K_i(T) = \frac{(C)^{n_C} (D)^{n_D}}{(A)^{n_A} (B)^{n_B}} = \exp\left(\frac{-\Delta_R G^0}{RT}\right) \quad (4-4)$$

where  $n_i$  is the stoichiometric coefficient,  $K$  is the thermodynamic equilibrium constant of formation,  $G_0$  is the Gibbs free energy of the reaction,  $R$  is the perfect gas constant and  $T$  is the absolute temperature [K]. HYTEC uses equilibrium constants, not Gibbs free energy data.

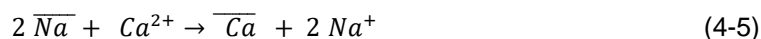
The empirical formula of the truncated Davies model derived from the Debye-Huckel model of activity corrections of dissolved ions was used for this study. The model is applicable for low to moderately mineralized solutions (i.e. ionic strength  $\leq 0.5$  mol/kg). The B-dot model and specific ion theory (SIT) are also implemented in HYTEC to calculate activity corrections at higher ionic strengths.

HYTEC is interfaced with the databases EQ3/6, ThermoChimie and Thermoddem.

### 4.2.2 Sorption by ion exchange and surface complexation

HYTEC simulates cation exchange by a solid exchanger (montmorillonite, zeolite, etc.) whereby ions in the interlayer space or channels of the crystal structure can be moved into solution to be exchanged for

other ions from the solution keeping electroneutrality. For instance, Na<sup>+</sup> substitution by Ca<sup>2+</sup> cations present in solution writes as:



where the upper bar stands for a cation within the solid. The distribution of the cations between the solution and the exchanger is given by a relation derived from the law of mass action and the Gaines-Thomas (GT) formalism:

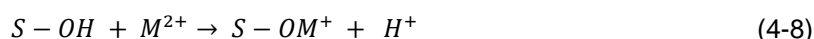
$$K_{GT}(\overline{Na}/\overline{Ca}) = \frac{f_{\overline{Ca}} (Na^+)^2}{f_{\overline{Na}}^2 (Ca^{2+})} \quad (4-6)$$

assuming that the activity of the exchangeable cations can be modeled by an equivalent fraction

$$f_{\overline{Ca}} = \frac{[\overline{Ca}]}{\sum_i [\overline{C}_i]} = \frac{[\overline{Ca}]}{CEC} \quad (4-7)$$

where the bracket stands for the exchangeable cation concentration, usually given as meq/100g of exchanger, and CEC (cation exchange capacity) is the sum of all the exchangeable cation concentrations.

HYTEC can also simulate the (ad)sorption processes of elements from the solution occurring at the surface of a given solid (magnetite, montmorillonite...). That is to say true complexation reaction at interface between the solution and hydroxyl sites S-OH present at the solid surface, such as for instance:



as well as acid–base reactions, for instance:



that can be modeled as a mass action law:

$$K = \frac{(S - OH)}{(S - O^-)(H^+)} \quad (4-10)$$

considering an additional electrostatic term through the double layer model or not.

## 4.3 Kinetics controlled on solid phase reactivity

### 4.3.1 General chemical kinetic law

HYTEC can also model the kinetics of different types of reactions, such as redox reactions in solution or dissolution/precipitation of minerals. The rate of dissolution or precipitation of a mineral M<sub>i</sub> can be modeled by the following rate law:

$$\frac{d[M_i]}{dt} = k_i A_{v,i} \prod_i (E)^{p_i} \left( \left( \frac{Q_i}{K_s} \right)^m - 1 \right) \quad (4-11)$$

The variation of the mineral concentration is proportional to the intrinsic kinetic constant of the reaction,  $k_i$  [mol/m<sup>2</sup>/s] and to the mineral surface area per unit volume,  $A_v$  [m<sup>2</sup>/L]. The term  $(Q/K_s)^m - 1$  is dependent on the deviation from thermodynamic equilibrium and related to the concept of the saturation index ( $Q_i$  stands for the ion activity product and  $K_s$  is the “solubility product”, i.e. the inverse of thermodynamic formation constant used in the HYTEC database). Precipitation (oversaturation state)

takes place if  $Q > K_s$ , otherwise dissolution (undersaturation state). The exponent  $m$  is an empirical parameter.

The product term  $\Pi_i$  describes the dependence of the reaction rate with respect to the chemistry of solution. The species act as catalysts if the exponent is positive, or as inhibitors if the exponent is negative. The term  $(E_i)$  is the activity (or concentration) of a dissolved species (e.g. hydroxyl ion OH<sup>-</sup>) and  $p_i$  is a power-constant, mechanistically-based or fitted to experimental data.

A summation of several kinetics laws similar to Eq. 3-11 can be set for a same mineral, typically to take into account specific pH-dependencies for acidic, neutral or alkaline conditions, as well as redox-dependency with specific laws under oxic and reducing conditions.

The dissolution and precipitation of the minerals constitutive of the clay host rock have to be modeled under kinetics controlled (De Windt et al., 2008; Marty et al., 2015), according to Eq. 4-11.

In a first step, the cement phase evolution will be modeled in Subtask 2.2 under thermodynamic equilibrium due to the high reactive surfaces of the mineral phases (C-S-H, etc.). This seems reasonable for the CEM I based materials. This is clearly a simplification for the hydration of the CEM III, and to a lesser extent the silica fume, used in the bentonite/cement grout (see Chapter 5). These components are kinetically controlled due to the resistance of blast furnace to aqueous hydrolysis reaction. The higher the temperature, the faster the reaction and the closer to equilibrium state. Therefore, the approximation is stronger at 20°C than at 80°C. However, kinetics of anhydrate dissolution will be implemented if required to better fit the experimental data with the bentonite grout.

#### 4.3.2 Application to metallic iron corrosion

The carbon-steel overpack is chemically considered as Fe(0) in the HYTEC modeling. Under anoxic conditions, the kinetics law of the initial corrosion rate may be simple and only considers the reactive surface of the metallic iron materials and the intrinsic rate constant  $k_{anox}$ :

$$\frac{d[Fe(s)]}{dt} = -k_{anox} A_v \quad (4-12)$$

The corrosion rate constant  $k$  of in Eq 3-14 is usually in mol/m<sup>2</sup>/s units. There is no distinction of the anodic reaction (oxidation of metallic iron) and cathodic reaction (reduction of water) and as an electrochemical approach. This follows a global mass balance approach that at the basis of most reactive transport codes.

Hydrogen generation by corrosion and migration in water is calculated as a tracer without any effect of the gas on the water saturation degree and the redox chemistry (De Windt et al., 2014).

Under the anoxic conditions assumed in ILW and HLW disposal cells, the most stable corrosion product of metallic iron is magnetite (Fe<sub>3</sub>O<sub>4</sub>) at basic pH, but iron carbonates such as siderite (FeCO<sub>3</sub>) or chukanovite (Fe<sub>2</sub>(OH)<sub>2</sub>CO<sub>3</sub>) are also likely as soon as the pH decreases (Chapter 2). The HYTEC modeling can take into account magnetite and carbonate iron phases, but also Fe(II)-silicates (e.g. greenalite Fe<sub>3</sub>(Si<sub>2</sub>O<sub>5</sub>)(OH)<sub>4</sub> or cronstedtite). Temperature should enhance the kinetics of formation of iron silicates. The forthcoming results of the BACUCE experiment will help to fix the most representative corrosion products. Iron sulfides (e.g. mackinawite) also form when corrosion is driven by bacteria activity. This microbial process is not considered in the present study.

In a first approach, the precipitation of the corrosion products will be modeled assuming thermodynamic equilibrium. If it does not fit with the experimental data (e.g. magnetite superstability), a kinetic control will be implemented in the modeling. The formation constants of all these corrosion products are included in the Thermoddem and ThermoChimie databases.

The models only describe the film growth of an iron oxide layer on iron in alkaline conditions. The coupled corrosion of iron and the evolution of a dense oxide layer taking into account moving interfaces can be simulated by the numerical code CALIPSO (Bataillon et al., 2012). Most, if not all, generic

reactive transport model such HYTEC cannot simulate the electrochemical processes. But they might simulate to some extents the diffusive transfer between different layers of corrosion products at the submicron scale with a diffusive barrier effect. It is not obvious to attribute an effective diffusion coefficient  $D_e$  to the corrosion product layer. A  $D_e$  value of  $10^{-11}$  m<sup>2</sup>/s will be first considered in the present calculations. The porosity can be arbitrarily set to 20 % or less. Corrosion of steel and its evolution with time will be implemented in HYTEC by implementing an inhibitive feedback with the increase of a given mineral (e.g. magnetite) such it has been done, for instance, with GRAAL model for glass dissolution (Frugier et al., 2008).

#### 4.4 Temperature dependencies

Chemical thermodynamics, kinetic rates and diffusion processes are temperature dependent in HYTEC. Heat-transfer by conduction and convection can also be modeled with HYTEC but will not be considered in task 2 where temperature is locally constant and the temperature gradient flat. The diffusion coefficient increases with temperature according to the Stokes-Einstein law in liquid or to an Arrhenius law in porous media. In the present modeling the increase of the diffusion coefficients will be manually calculated by an Arrhenius law and automatically by HYTEC.

The thermodynamic formation constants are calculated over a wide range of temperature by using a polynomial interpolation of the constants reported at fixed temperatures in the databases available with HYTEC (e.g. 0, 25, 60, 100, 150 and 200°C). The water dissociation constant ( $K_w$ ) with temperature increases with temperature, leading to a shift of the pH scale towards the more acidic boundary.

The accelerating effect of temperature on the kinetic rate constant  $k_i$  (Eq. 3-11) is implemented in the form of an Arrhenius law, according to the following equation:

$$k = k_0 e^{\frac{E_a}{R} \left( \frac{1}{T_0} - \frac{1}{T} \right)} \quad (4-13)$$

where  $E_a$  is the activation energy [kJ.mol<sup>-1</sup>],  $R$  the perfect gas constant [J.mol<sup>-1</sup>.K<sup>-1</sup>] and  $T$  the temperature [°K].

Kinetics can also be expressed as inhibitive thresholds. For example, temperature increase up to 80°C favors the formation of zeolites (Lalan et al., 2016) and crystalline C-S-H such as tobermorite (Lalan et al., 2019) at the interface between cement and argillite, phases whose precipitation is inhibited at a temperature of 20°C.

Diffusion coefficients also increase with temperature. This effect can be implemented according to an Arrhenius law:

$$D = D_0 e^{\frac{E_a}{R} \left( \frac{1}{T_0} - \frac{1}{T} \right)} \quad (4-14)$$

or be fixed in the input file under isothermal conditions. For example, to account for the temperature increase from 20 to 70°C, the effective diffusion coefficient was multiplied by a factor 3 for the argillite, as found both for the Callovian-Oxfordian clay (Savoye et al., 2011) and the Opalinus clay (Van Loon et al., 2005), and by a factor 10 for the OPC paste in agreement with Page et al. (1981).

#### Take away:

Usual reactive transport model as HYTEC can be applied to the modeling of the generalized corrosion of carbon steel at the interface with cement. They cannot simulate the electrochemical processes. But they might simulate to some extents the diffusive transfer between different layers of corrosion products at the submicron scale with a diffusive barrier effect. Kinetics is essential for simulating the corrosion

rates but thermodynamics is powerful for defining the nature of the corrosion products. Temperature effect is implemented both on chemical processes (kinetics and thermodynamics) and diffusion.

## 5. In situ cement/steel interactions – BACUCE experiments

*MINES ParisTech, IRSN and Subatech*

The in situ BACUCE experiments aim at studying the steel/cement interface under the most representative disposal conditions as possible, including carbon steel plus high-pH and low-pH cement materials embedded in a clayey host rock at low (15°C) and high (80°C) temperatures. It is one of the outstanding experiments of Task 2. A set of complementary tests are also conducted at the laboratory in the BACUCE project to bring more specific information and to support the interpretation of the in situ results. The aim of this chapter is to gather all the geometric and boundary conditions of the experimental set-ups as well as all the transport and chemical properties of the materials that are required to develop a highly representative reactive transport model of the experimental results once available. Whenever possible, preliminary geochemical modeling of the initial state of the materials are also presented in this chapter. In particular, the bentonite/cement grout is a new type of engineering material of which chemistry and hydration products are not well defined yet both at ambient and high temperatures.

The first section is devoted to the main features of the experimental set-ups (Sec. 5.1). It is followed by a focus on CEM I at 80°C (Sec. 2), then the bentonite/cement grout (Sec. 3). A short section deals with the host rock (Sec. 4). The results obtained so far gives then input to Sec. 5.5 to define the synthetic water that will be used in the BACUCE experiment.

### 5.1 Set-up of the BACUCE experiments

#### 5.1.1 In-situ tests on steel corrosion at 15°C and 80°C

The BACUCE experiments are taking place in the IRSN underground research laboratory (URL). The URL is located in a tunnel that crosses a 250 m thick argillaceous formation of Toarcian and Domerian ages at Tournemire (Aveyron, France). *Figure 14* gives a schematic representation of the BACUCE in-situ experimental set-up to characterize the interface between carbon steel and two cementitious buffers (a bentonite/cement grout and a CEM I cement paste) until three years of interaction. The experiments are conducted at the ambient temperature of 15°C and at 80°C with a heating system. The cementitious buffer is injected in the annular gap between the steel cylindrical tube and the wall of the borehole drilled into the argillite formation. Then, the retrieval of a PTFE rod initially placed in contact with the metallic tube allows the creation of a void space mimicking a heterogeneity of filling by the cementitious material (bentonite/cement grout and CEM I). Then, an external reservoir helps to saturate this heterogeneity with adapted synthetic porewater (either 75% of hydrated bentonite/grout porewater + 25% of Toarcian porewater or young CEM I synthetic porewater). The external reservoir also helps to hydrate the grout and cement and afterwards to maintain a water saturation degree of 100 %. One specificity is to study the influence of imperfect contacts or voids that are filled with grout porewater solution mixed with the argillite one.

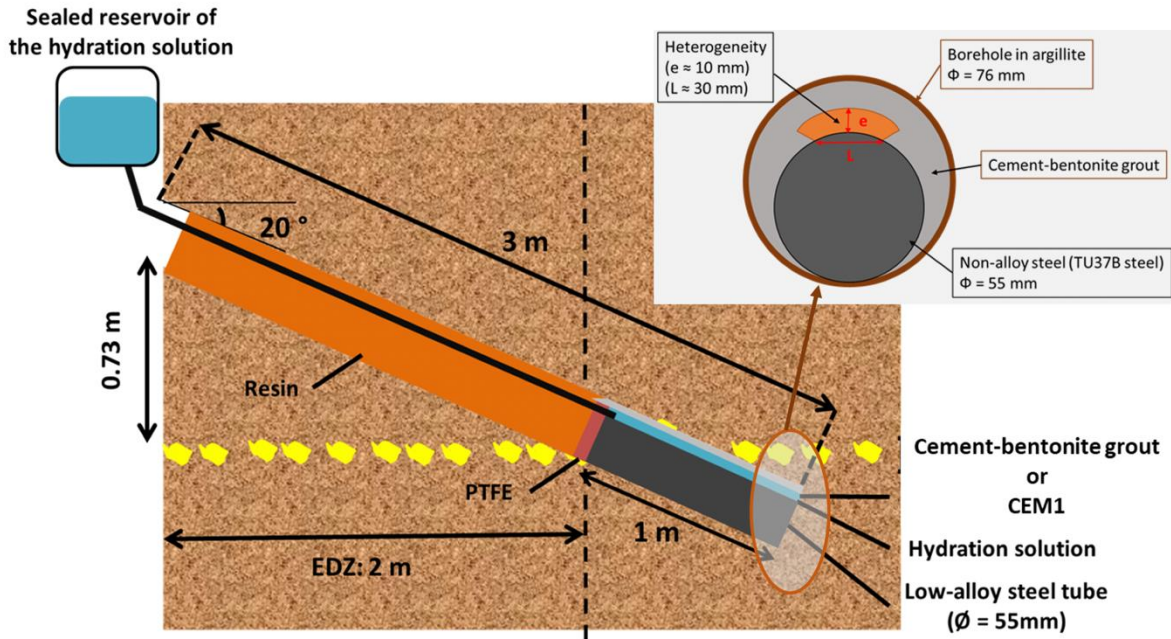


Figure 14–Schematic representation of the first BACUCE in-situ experimental set-up in the Tournemire URL at ambient temperature (15°C) (top) and zoom on the heterogeneous configuration of the reactive chamber (bottom). In the new experiments that will be conducted at 80°C, the borehole diameter is equal to 101 mm, and the tube diameter to 65 mm.

### 5.1.2 Lab experiments on steel corrosion in grout water at 25°C

Grousset et al., (2018, 2019) also performed two types of experiments at the laboratory in support of the in situ experiments. The first experiment is devoted to the estimation of the porewater chemistry of the bentonite/cement grout. A set of batch experiments put in contact powdered grout and distilled water for decreasing Liquid on Solid weight ratios (L/S from 9 to 1). The kinetics of interactions is studied by measuring the evolution of the chemistry (main cations and anions, pH, TIC, TOC) at 1, 3 and 7 days.

The second type of experiment is depicted in Figure 15. Corrosion tests at 25°C are conducted under both anoxic and abiotic conditions to assess of the efficiency of the chemical slightly alkaline conditions, created by the cement-bentonite grout porewater, to protect the carbon steel liner against corrosion. S235 carbon steel parallelepipedic blocks or “coupons” (30 x 30 x 2 mm<sup>3</sup>) were immersed in 325 mL of solution for 285 days under deaerated conditions (Figure 15). Several mixing ratios of synthetic argillite water and synthetic grout water were considered.

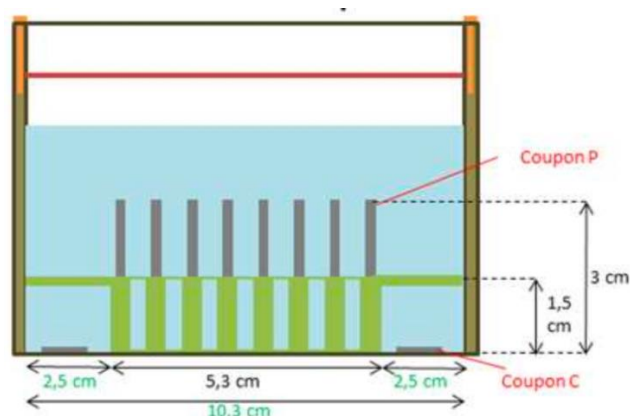


Figure 15 – Schematic representation of the BACUCE experimental set-up at the laboratory (the green zones stand for the mechanical support of the steel “coupons”, not for the bentonite/grout cylinders).

### 5.1.3 Lab experiment on the mill-scale effect on steel corrosion at 80°C

Additional laboratory experiments are planned to assess the effect of mill scale on the corrosion rate of low carbon steel in similar conditions as the BACUCE experiments. These experiments will also allow to evaluate the synthetic porewater evolution in contact with the two buffer materials (CEM I/MREA) at 80°C, as well as the cement and steel corrosion products evolution.

In a first set of experiments, S235 steel parallelepipedic blocks embedded in CEM I (Lafarge, Val d’Azergues) cylinders are placed in PTFE containers in contact with a synthetic young CEM I porewater. In a second set, steel (S235) parallelepipedic blocks embedded in bentonite grout (MREA) cylinders are placed in PTFE containers in contact with a synthetic porewater made of 75 % bentonite grout porewater + 25 % Toarcian argillite porewater. For each steel block, two faces are prepared following an ASTM standard method to evaluate the corrosion rate of the low carbon steel itself. On the four other faces, the mill scale is conserved to detect an eventual protective/aggressive effect of this coating on the corrosion rate (*Figure 16a*). The PTFE containers are placed in an oven at 80°C under anoxic conditions (argon atmosphere). For each kind of buffer material (CEM I/MREA), 6 containers are placed in the oven. The containers are retrieved periodically (every 2 weeks for the first two and then every 2 months) to determine the corrosion rate, the evolution of water chemistry and the mineralogical evolution of the buffer materials. In parallel, blank experiments with only synthetic porewater are conducted to follow the pH and the water chemistry evolution with time at 80°C.

As the mill scale is different in the parallelepipedic blocks S235 and on the TU37b tubes used in BACUCE experiments, similar experiment with TU37b steel tubes embedded in MREA will be conducted (not possible with CEM I due to lack of steel tube), as shown in *Figure 16b*.

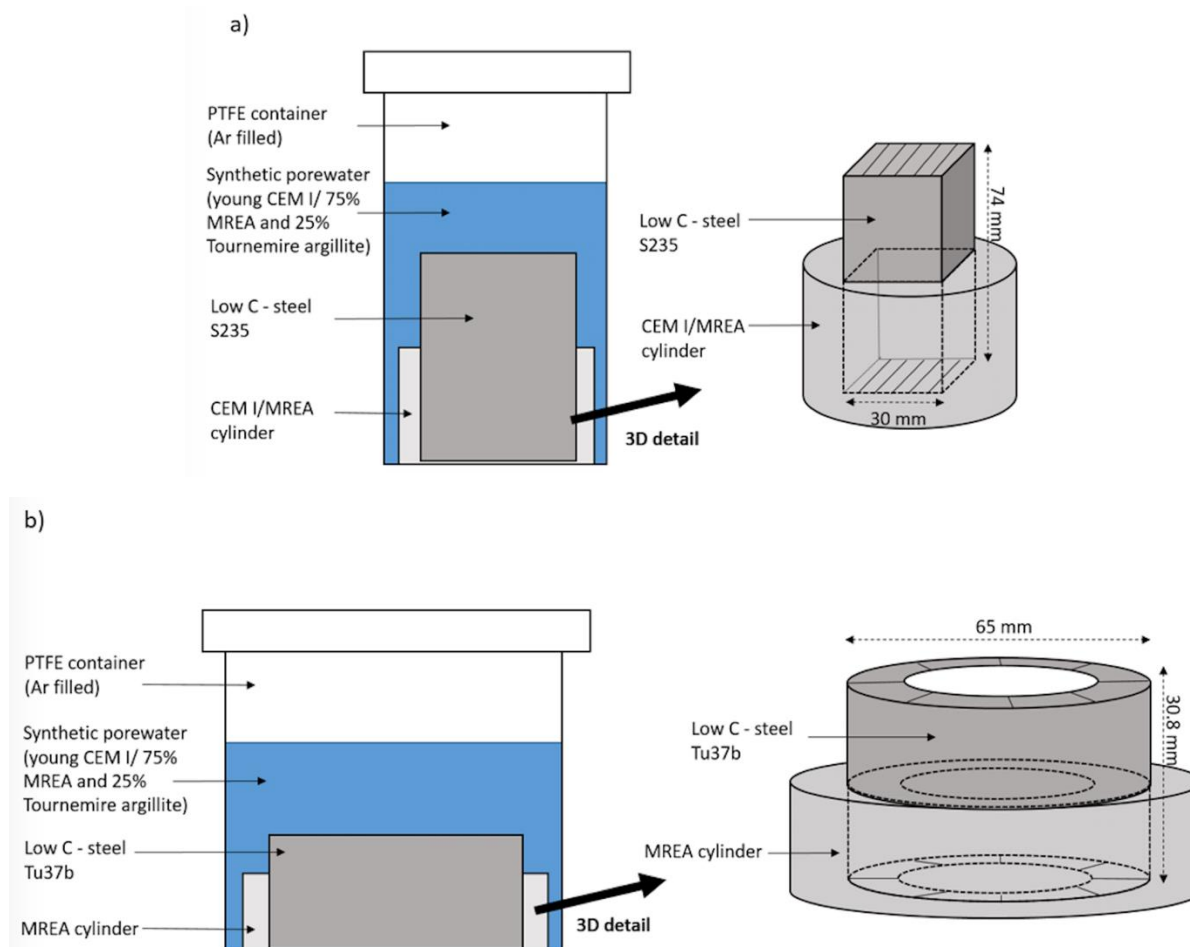


Figure 16 – Schematic representation of the laboratory scale experiment simulating the BACUCE experiment. The prepared steel surface following the ASTM standard method are represented hatched. a) experiment with S235 steel and b) experiment with TU37b steel.

## 5.2 Properties and modeling of the hydrated CEM I paste

The geochemical, mineralogical and diffusive properties of the materials have to be compiled in a consistent manner to develop a representative reactive transport model of the forthcoming results. This section focusses on the properties of the CEM I cement used in the BACUCE experiment with a specific attention paid to the effect of temperature while increasing from 20°C to 80°C. A model of the initial state of the cement (hydrated cement phases, pore water chemistry) is then built. This model will be integrated in the actual reactive transport modeling of the experimental results one available.

### 5.2.1 Bulk and mineralogical composition

The selected CEM I cement is a sulfate resisting Portland cement from Val d’Azergues (CEM I 52.5 N), provided by the French company Lafarge. Hydration was performed with a water/cement mass ratio of 0.42. Cement paste characterization by XRD confirmed the presence of portlandite, C-S-H, Si-katoite ( $\text{Ca}_3\text{Al}_2\text{SiO}_4(\text{OH})_8$ ), ettringite, traces of calcite and anhydrous species. More details on the characterization are given in Lalan et al. (2016). Katoite is part of a solid series between two endmembers, grossular ( $\text{Ca}_3\text{Al}_2\text{Si}_3\text{O}_{12}$ ) and synthetic phase ( $\text{Ca}_3\text{Al}_2(\text{OH})_{12}$ ), also known as hydrogarnet. Table 4 summarizes the bulk chemical and mineralogical composition of the cement before hydration. The water to cement ratio (W/C) is 0.42 at both 20°C and 80°C.

The preliminary modeling of the hydrated cement paste was made at thermodynamic equilibrium based on the bulk composition of the composite material. The Thermoddem thermodynamic database (Blanc et al., 2012; version 1.07) was used. Sorption of Na<sup>+</sup> and SO<sub>4</sub> on C-S-H is not considered. After hydration, the calculated mineralogy is usual for a CEM I hydrated paste with portlandite, C-S-H of high C/S ratio and ettringite (Table 5). The presence of katoite (confirmed by XRD analysis) is uncommon and related to the Val d’Azergues CEM I.

Katoite stabilizes ettringite that should be partly or totally dissolved at 80°C. According to the literature, when ettringite dissolves, the sulfate content is distributed among the porewater solution, sorption onto the C-S-H phases, and as a new mineral, monosulfoaluminate.

As shown in Table 5, a partial transformation of ettringite into katoite when the temperature increased from 20°C to 80°C was noticed. The dissolution corresponds to a re-arrangement of the katoite/ettringite equilibrium with temperature. This difference in the cement paste may be explained by the relatively high amount of C4AF compared to C3A in the OPC used for the present experiment. *Figure 17* provides for the domain of relative stability between the Al-phases ettringite-katoite-Afm-C3AH6 at 20 °C and 70°C (also representative of 80°C). *Figure 17* also indicate that the usual conversion of ettringite into monosulfoaluminate will take place after 60°C if one does not consider katoite in the mineral assemblage. The stability of katoite seems to be specific to the Val d’Azergues cement. It will be questioned again in BACUCE during the postmortem analysis of the samples.

### 5.2.2 Porewater chemistry

Table 6 gives the preliminary modeling results of the porewater chemistry at 20°C and 80°C. At 80°C, the pH scale changes compare to the usual standard temperature due to the increase of the water decomposition product  $K_w$  with temperature. The activity (or total content) of the solution in OH<sup>-</sup> species is a better parameter of the “alkaline loading”.

At 20°C, the porewater corresponds to a classical fresh (young) porewater enriched in NaOH and KOH with a pH larger than 13. The calculated pH of 13.6 is slightly overestimated because a fraction of the Na-K-OH loading could be decreased by sorption onto the C-S-H phases.

Heating of this young state to 80°C does not change significantly the chemistry, excepted the important increase in sulfate anions from 1 to 110 mmol/L. This increase was validated by indirect analysis that showed that the sulfate content was at least higher than 65 mmol/L at 70°C (Lalan, 2016). Half of the sulphates are adsorbed on the C-S-H. A high C/S ratio, as is the case in a sound OPC, and a high temperature favor sulphate adsorption by C-S-H, (Barbarulo, et al., 2007; Divet et al., 1998). Assuming monosulfoaluminate instead of ettringite in the model increases the SO<sub>4</sub> ratio from 140 to 200 mmol/l approximately.

A second modification is the decrease in OH<sup>-</sup> content at 80°C, which is divided by a factor 2.5. This is this content in hydroxyl OH<sup>-</sup> that represents the alkaline aggressivity of the porewater. But, globally, the basicity remains very high (125 mmol/L of OH<sup>-</sup> lead to a pH of 13.3 at 20°C, and a pH of 11.5 at 80°C).

### 5.2.3 Porosity and diffusion properties

The mass transport is only driven by diffusion when fully hydrated since hydrated cement pastes (and argillite in the in situ experiment) have low hydraulic conductivities and the cells are not subjected to any pressure gradients. The theoretical connected porosity (Hg measurement) assumed for the mineralogy of Table 5 is 25 %. The true connected porosity could be slightly higher in the range 30 – 35 % (Lalan et al., 2019). The effective diffusion is approximately  $6 \times 10^{-12}$  m<sup>2</sup>/s at 20°C and  $5.8 \times 10^{-11}$  m<sup>2</sup>/s at 70°C (Lalan et al., 2019). The effective diffusion coefficient is thus multiplied by a factor 10 for the OPC paste in agreement with Page et al. (1981).

Table 4 – Cement composition (CEM I 52.5 N – Lafarge).

Global bulk chemistry (wt.%)		Mineralogical composition (g/100g)	
CaO	64.6	Clinker	93.2
SiO <sub>2</sub>	20.7	including Alite (C3S)	65.3
Al <sub>2</sub> O <sub>3</sub>	3.2	Belite (C2S)	13.5
Fe <sub>2</sub> O <sub>3</sub>	4.5	Aluminate	0.9
CaO (free)	1.8	(C3A)	13.5
MgO	0.6	Ferrite (C4AF)	
K <sub>2</sub> O	0.6	Gypsum	3.9
Na <sub>2</sub> O	0.1	Filler	2.9
CO <sub>2</sub>	1.1		
SO <sub>3</sub>	2.8		

Table 5 – Preliminary modeling of the mineralogy of the hydrated CEM I paste (Val d’Azergues) at 20°C and after a temperature increase to 80°C.

Mineral (mol/L of cement paste)	20°C	80°C
Portlandite	6.30	6.35
C-S-H 1.6	4.40	4.39
Ettringite <sup>(1)</sup>	0.13	0.12
Katoite	0.68 <sup>(2)</sup>	0.69 <sup>(2)</sup>
Calcite	0.39	0.39

(1) Ettringite is stable when katoite is present in the modeling; sorption of SO<sub>4</sub> on C-S-H is not considered; (2) assuming thermodynamic equilibrium, probably overestimated.

Table 6 – Preliminary modeling of the porewater chemistry of the hydrated CEM I paste (Val d’Azergues) at 20°C and after a temperature increase to 80°C.

Aqueous species (mmol.L <sup>-1</sup> )	20°C	80°C
pH	13.6 <sup>(1)</sup>	11.5 <sup>(1)</sup>
(OH <sup>-</sup> activity)	(0.26)	(0.07 <sup>(2)</sup> )
K <sup>+</sup>	350 <sup>(1)</sup>	350 <sup>(1)</sup>
Na <sup>+</sup>	65 <sup>(1)</sup>	100 <sup>(1)</sup>
Ca <sup>2+</sup>	0.9	4.0
Al <sup>3+</sup>	0.2	0.13
H <sub>4</sub> SiO <sub>4</sub>	0.05	0.19
HCO <sub>3</sub> <sup>-</sup>	0.2	0.1
Cl <sup>-</sup>	15 <sup>(2)</sup>	50 <sup>(2)</sup>
SO <sub>4</sub> <sup>2-</sup>	1.1	144 (200) <sup>(3)</sup>

(1) Slightly overestimated due to the lack of sorption of alkali onto C-S-H; (2) Estimated and entered as NaCl in the model; (3) Assuming equilibrium with monosulfoaluminate, not with ettringite.

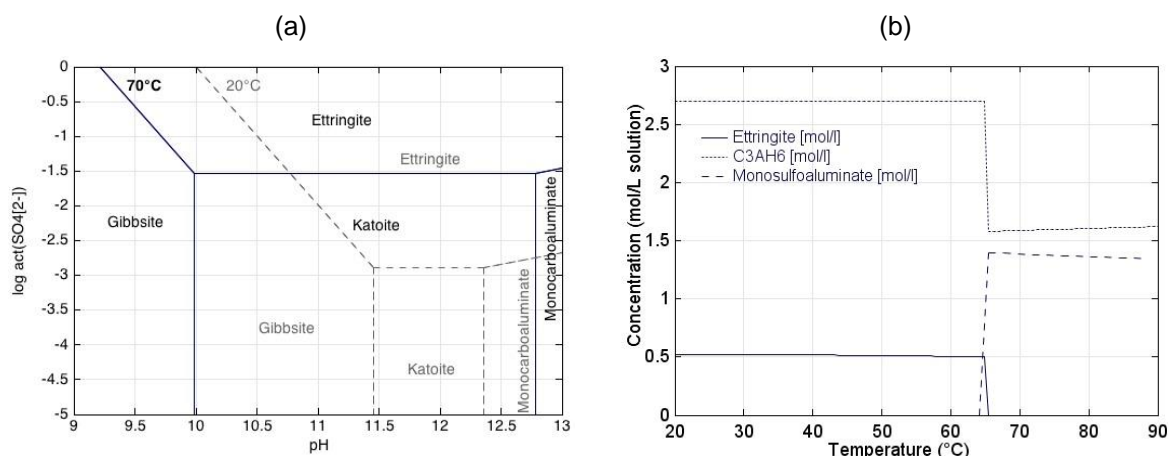


Figure 17 – (a) Calculated stability diagrams of Al-phases at 20°C and 70°C ( $act. Ca^{2+} = act. Al(OH)_4^- = 10^{-3}$ ,  $[HCO_3^-]_{total} = [H_4SiO_4]_{total} = 10^{-3}$  molal) considering katoite in the mineral assemblage. (b) modeling of the conversion of ettringite into monosulfoaluminate without considering katoite in the mineral assemblage.

## 5.3 Properties and modeling of the bentonite/cement grout

### 5.3.1 Bulk and mineralogical composition

The actual composition of the bentonite/cement grout of reference for the French concept is not fixed yet, but the nature of the components is known (Michau and Bourbon, 2016). Table 7 summarizes the bulk chemical and mineralogical composition of the bentonite/cement grout before hydration. The water to cement ratio is much higher than for classical cements, W/C = 2 instead of W/C around 0.5. The bulk composition used in the modeling includes the cement phase (and its gypsum additive) and the silica fume, which will be hydrated partly once in contact with water. The bentonite does not account for the bulk composition, it is introduced directly as a mineral in the model with cationic exchangeable properties of montmorillonite (Bradbury and Baeyens, 2002)

Eventually, the initial hydrotalcite content is not considered due to its weak percentage and because hydrotalcite is readily generated during the hydration process in the modeling.

Table 7 – Recipe and bulk composition of the bentonite/cement grout used in the modeling.

Global bulk chemistry for hydration of CEM III + silica fume (kg)		Composition (kg)	
CaO	0.30	CEM III Rombas (35% clinker/gypsum + 65% blast-furnace slag)	0.600
SiO <sub>2</sub>	0.75		
Al <sub>2</sub> O <sub>3</sub>	0.055		
MgO	0.03		
K <sub>2</sub> O	0.0042		
Na <sub>2</sub> O	0.0024	Silica fume	0.600
		Bentonite (Montmor <sup>(1)</sup> )	0.160 (0.145)
		Hydrotalcite	0.04
CaSO <sub>4</sub>	0.025	Water	2.400
CaCl <sub>2</sub> ·2H <sub>2</sub> O	0.0037		

(1) Na-montmorillonite, exchangeable fraction = 100 % Na<sup>+</sup>.

### 5.3.2 Modeling of hydrated grout/water batch tests

A set of batch tests of decreasing water/hydrated grout ratio (L/S from 9 to 1) has been performed in the first stage of the BACUCE project at room temperature. The grout was first hydrated and cured and the added water consisted in demineralized water. The cement-bentonite suspension is obtained by mixing ultrapure water with crushed cement-bentonite paste samples previously cured for one month in a sealed bag at room temperature (liquid/solid = 9 ml/g and 24h stirring). Only the smallest ratio is taken into account in this note, the full modeling will be done later. The porewater is approximately divided by a factor 3 at this L/S = 1.

Modelling of the hydration products is done by two different models by using the Thermoddem database (Blanc et al., 2012; version 1.7 for model 1 and version 1.10 for model 2). Model 1 is based on a simpler approach with proxy minerals for C-A-S-H phases whereas model 2 takes into account the very recent data acquired on the C-A-S-H phases, as shown in *Table 8*. The C-S-H phase has a lower Ca/Si ratio (C/S = 0.8) than in CEM I (C/S = 1.6) in direct relation with the bulk grout composition that has a smaller relative amount of CaO compared to CEM I (or similarly the silica component is higher in the grout due to the significant SiO<sub>2</sub> input of the silica fume). The CEM III also brings more aluminum in the system than CEM I, which leads to the formation of CAH (model 1) or C-A-S-H (model 2) phases. XRD analyses were done on the hydrated grout. They showed the presence of quartz, C-S-H, and montmorillonite (i.e. the stability of the montmorillonite) in agreement with the model, but also the occurrence of portlandite and gypsum (and not ettringite) which were not predicted by the models. The C-A-S-H phases are not easy to be identified by XRD. The presence of portlandite is not in agreement with the data on the batch tests discussed in the next paragraph. The literature on the hydration of CEM III at low temperature reports the possibility of hydrotalcite, ettringite, C-S-H/straetlingite (or C-A-S-H depending on the papers); the C-S-H being of low C/S ratio. There is, therefore, a good qualitative agreement with the results of the present model with respect to the mineralogy.

It is worth mentioning that the hydration of the CaO oxide strongly modifies the cationic exchange composition of montmorillonite in the model, since one evolves from a pure Na-clay phase to a dominant Ca-clay phase (*Table 8*). Literature reports the occurrence of such processes during the hydration of lime/clay system, but it is not clear how far this process takes place in the present system. *Table 9* gives the constants of cationic exchange and surface complexation reactions used in this preliminary modeling. Furthermore, it is not yet clear how far the montmorillonite reacts as a pozzolanic reactivity or remained stable (XRD analysis on the grout indicated some occurrence of montmorillonite at 20°C).

*Table 10* indicates a reasonably good agreement between the modelled and the experimental data. Model 1, despite its simplicity, is in average a better operational model than model 2. The main discrepancies with the experimental results are related to the pH, K and SO<sub>4</sub> contents. The modelled pH is lower; the models consider a full hydration of the oxides, which is relevant for most clinker phases but not realistic for the blast furnace slag component. It is worth noting that portlandite would have buffered the pH at a value of 12.3; which is clearly not the case (the portlandite identified by XRD is maybe not accessible to the water due to coating, etc.). The input of Al into the system is overestimated by the model for the same reason.

There is not batch data at 80°C yet. The literature indicates that the hydrations of slag and silica fume are relatively slow at 20°C (about 1 year or more). A kinetic approach is more relevant but also much trickier to implement. It is also assumed that this modeling artefact maybe less important at 80°C than at 20°C since the rate constants (i.e. the slag hydration) increases with temperature. Under these lines, it is expected that a model based on kinetically driven hydration of the slag will increase the drop of pH from 20 to 80°C compared to this simplified model that assumes thermodynamic equilibrium.

Along the same lines, the full modeling of the grout porewater is still in progress since the analysis of the hydrated grout in its initial state and after interaction with the argillite are not available yet.

*Table 8 – Preliminary modeling of the mineralogy of bentonite/cement grout derived from batch experiments made with demineralized water at 20°C and a L/S ratio = 1 (ST1-1-7j).*

Mineral (wt.%)	Model 1 20°C	Model 2 20°C
C-S-H 0.8	48.5	-
straetlingite (cryst. C-A-H)	7	-
C <sub>0.8</sub> S-H	-	11
C <sub>0.7</sub> -A <sub>0.05</sub> -S-H	-	49.5
ettringite	6	4
gypsum	0	0
hydrotalcite	5	5.5
quartz	24.5	21
Montmorillonite	9	9
exchangeable	Ca <sup>2+</sup> 85%	90
equiv. fraction	Na <sup>+</sup> 15%	10

(1) As a first approximation since montmorillonite dissolution by pozzolanic reactivity may occur at 20°C on the long term.

Table 9 – Selectivity constants of cationic exchange (Gaines-Thomas formalism, Tremosa et al., 2012) and constants of surface complexation reactions (non-electrostatic model, Marques et al., 2012) of montmorillonite considered in the modeling of the bentonite fraction of the grout as well as for the clayey phase of the argillite.

Reaction	Log K <sub>ex</sub> (25°C)
Cation exchange (whole exchanger)	
$\overline{\text{Na}} + \text{K}^+ \rightarrow \overline{\text{K}} + \text{Na}^+$	0.9
$2 \overline{\text{Na}} + \text{Ca}^{2+} \rightarrow \overline{\text{Ca}} + 2 \text{Na}^+$	0.6
$2 \overline{\text{Na}} + \text{Mg}^{2+} \rightarrow \overline{\text{Mg}} + 2 \text{Na}^+$	0.6
$2 \overline{\text{Na}} + \text{Fe}^{2+} \rightarrow \overline{\text{Fe}} + 2 \text{Na}^+$	0.7
Surface complexation <sup>(2)</sup>	
$\text{S}_1\text{-OH} + \text{H}^+ \rightarrow \text{S}_1\text{-OH}_2^+$	4.5
$\text{S}_1\text{-OH} \rightarrow \text{S}_1\text{-O}^- + \text{H}^+$	-7.9
$\text{S}_2\text{-OH} + \text{H}^+ \rightarrow \text{S}_2\text{-OH}_2^+$	4.5
$\text{S}_2\text{-OH} \rightarrow \text{S}_2\text{-O}^- + \text{H}^+$	-7.9
Site density S <sub>1</sub> -OH	1 μmol/m <sup>2</sup>
S <sub>2</sub> -OH	0.05 μmol/m <sup>2</sup>

(1) LogK (Fe) = logK (Ca) + 0.1 (Idiart & Iavina, 2019); (2) Optional for pH buffering.

Table 10 – Preliminary modeling of the batch experiment, water chemistry: bentonite/cement grout in contact with demineralized water at 20°C, L/S ratio = 1 (ST1-1-7j).

Total concentration (mmol.L <sup>-1</sup> )	Experimental data 20°C	Model 1 20°C	Model 2 20°C
pH	11.3	10.7	10.4
(OH <sup>-</sup> activity)	-	(0.41×10 <sup>-3</sup> )	(0.16×10 <sup>-3</sup> )
K <sup>+</sup>	3	15	15
Na <sup>+</sup>	12	15	15
Mg <sup>2+</sup>	0.0	0.0	0.0
Ca <sup>2+</sup>	3	5	10
Al <sup>3+</sup>	0.01	0.1	0.08
H <sub>4</sub> SiO <sub>4</sub>	1.5	1.6	0.8
Cl <sup>-</sup>	7	8.5	8.5
SO <sub>4</sub> <sup>2-</sup>	3	15	21

### 5.3.3 Modeling of the initial state of the hydrated bentonite/cement grout

Models 1 and 2 have been run to estimate the mineralogy and the porewater of the hydrated bentonite/cement grout (considering the water used in the recipe only without addition as in the batch tests), as detailed in *Table 11*. The final liquid on solid (L/S) ratio in the hydrated grout is close to 0.4 (for a porosity of 50 % and a weight mass of 2.7 kg/dm<sup>3</sup>). The mineralogy is globally not modified. The main difference is the destabilization of ettringite to produce gypsum and an increase of the Al-phases. Destabilization of ettringite with temperature is possible according to the literature, especially without katoite. Whatsoever, the amount of SO<sub>4</sub> phases is relatively low in the grout.

The main effect when moving from L/S = 1 to the porewater of *Table 12* is the increase in the concentration of whose elements that are mostly dissolved in the porewater and not controlled by the solubility of the solid phases: Na – K – Cl. This leads to a slight increase (factor 2) in the OH<sup>-</sup> content. The raise in the SO<sub>4</sub> concentration is linked to the destabilization of ettringite, not a concentration effect by removing the total amount of water in the system. If true, a common effect of temperature increase on CEM I and grout would be the increase of the SO<sub>4</sub> loading in the porewater.

It is worth emphasizing that the porewater of the bentonite/cement grout is much less aggressive and concentrated than the CEM I porewater.

### 5.3.4 Porosity and diffusion properties

The porosity and effective diffusion properties of the grout used in Subtask 2.2 have not been experimentally measured yet. One can estimate a porosity in the range 35 – 50 % and an effective coefficient D<sub>e</sub> around 10<sup>-10</sup> m<sup>2</sup>/s in the HYTEC modeling.

*Table 11 – Preliminary modeling of the mineralogy of the bentonite/cement grout at 80°C.*

Mineral (wt.%)	Model 1 80°C	Model 2 80°C
C <sub>0.8</sub> -S-H	50.5	-
straetlingite (cryst. C-A-H)	9	-
C <sub>0.8</sub> S-H	-	5.0
C <sub>0.7</sub> -A <sub>0.05</sub> -S-H	-	59
ettringite	0	0
anhydrite	2.5	2.0
hydrotalcite	5	5.5
quartz	24	19.5
Montmorillonite	9 <sup>(1)</sup>	9 <sup>(1)</sup>
exchangeable	Ca <sup>2+</sup> 45 %	45 %
equiv. fraction	Na <sup>+</sup> 55 %	55 %

(1) As a first approximation since montmorillonite dissolution by pozzolanic reactivity is likely at 80°C.

Table 12 – Preliminary modeling of porewater chemistry of the bentonite/cement grout at 80°C.

Total concentration (mmol.L <sup>-1</sup> )	Model 1 Young water 80°C	Model 2 Young water 80°C
pH (OH <sup>-</sup> activity)	9.7 (1.2×10 <sup>-3</sup> )	9.2 (0.4×10 <sup>-3</sup> )
K <sup>+</sup>	45	45
Na <sup>+</sup>	63	62
Mg <sup>2+</sup>	0.0	0.005
Ca <sup>2+</sup>	4	4
Al <sup>3+</sup>	0.3	0.07
H <sub>4</sub> SiO <sub>4</sub>	4	1.6
Cl <sup>-</sup>	25	25
SO <sub>4</sub> <sup>2-</sup>	43	45

## 5.4 Properties of the Toarcian argillite

### 5.4.1 Mineralogical composition

The Upper Toarcian argillite is mainly composed of clay minerals including illite, an illite/smectite mixed layer, kaolinite and chlorite. Minor minerals include quartz, carbonates, such as calcite and dolomite, feldspar and pyrite (*Table 13*). The divalent Ca<sup>2+</sup> and Mg<sup>2+</sup> are the main cations of the exchangeable cation population of the host rock, which is brought by the clayey phase mainly.

### 5.4.2 Cationic exchange and porewater chemistry

The porewater chemistry and cation exchanges have been modeled by Tremosa et al. (2012) with the multi-site cation exchange model. The same model will be applied in the Subtask2.2.

*Table 14* gives the cationic exchange capacity (CEC, 8.6 meq/100g of solid) and of the cationic population of the Toarcian argillite measured at the tunnel height. Calcium is the main exchangeable cation of the argillite.

Argillite porewater is diluted fossilized seawater containing mainly sodium, chlorides and sulfates with a pH of approximately 7.8 (De Windt et al., 1999; Tremosa et al., 2012), as shown in *Table 15*. The partial pressure of CO<sub>2</sub> is about 10<sup>-2.4</sup> atm. It is an important factor when estimating the carbonation of cement. The chloride dissolved concentration remains rather low in the Tournemire case and far from the concentrations that can increase the corrosion (Deissmann et al., 2020).

### 5.4.3 Porosity and diffusion properties

Porosity varies between 7 and 15 % (Tremosa et al., 2012; Wittebroodt et al., 2012). The hydraulic conductivity of the argillite is very low (10<sup>-13</sup> m/s) (De Windt et al., 1999) and again diffusion is the main transport process. The effective diffusion coefficient D<sub>e</sub> associated with neutral tracer (HTO) diffusion perpendicular to the rock stratigraphy is 7.7×10<sup>-12</sup> m<sup>2</sup>/s at 20°C (Motellier et al., 2007) and 2.3×10<sup>-11</sup> m<sup>2</sup>/s at 70°C (Lalan et al., 2019). The effective diffusion coefficient is thus multiplied by a factor 3 for the Toarcian argillite, as found both for the Callovian-Oxfordian (Savoye et al., 2011) and the Opalinus (Van Loon et al., 2005) clayey rocks.

Table 13 – Mineralogical composition of Toarcian argillite at the URL depth (Tremosa et al., 2012).

Minerals [wt.%]	Illite	I/S	Kaolinite	Chlorite	Quartz	Carbonates	Feldspar	Pyrite
	15–30	15–35	10–20	5	10–20	10-15	5	3

Table 14 – Cation exchange properties of reference for the Toarcian argillite at 20°C (Tremosa et al., 2012).

Exchangeable cation population % equivalent	CEC	
	8.6	meq/100g of rock
Na	19	
K	14	
Mg	22	
Ca	45	

Table 15 – Composition of reference for the argillite porewater (Tremosa et al., 2012).

Aqueous species	Total concentration (mmol.L <sup>-1</sup> ) 20°C
pH	7.8
K <sup>+</sup>	0.8
Na <sup>+</sup>	22.6
Mg <sup>2+</sup>	0.8
Ca <sup>2+</sup>	1.5
HCO <sub>3</sub> <sup>-</sup>	4.4
H <sub>4</sub> SiO <sub>4</sub>	0.1
Cl <sup>-</sup>	4.5
SO <sub>4</sub> <sup>2-</sup>	9.5

## 5.5 Synthetic porewaters for the experiments

Based on the modeling results of the previous sections, the possible recipe for the young CEM I synthetic water for the BACUCE experiment is given in Table 16.

The bulk recipe for the BACUCE experiment considering the grout is given in Table 17. The synthetic porewater injected in the in-situ experimental set-up is assumed to consist of 75 % of hydrated bentonite/grout porewater and 25 % of Toarcian argillite porewater. This 3/1 ratio mimicked the flux of the Toarcian porewater within the system. The same composition is used for the experiments made at 20°C and 80°C.

The chemical composition is reported in Table 18 after renormalizing to 1L and taking into account pH adjustment. It is worth noting that bicarbonate HCO<sub>3</sub><sup>-</sup> may create some problem of precipitation. The mixing between the argillite water (pH 7 – 8) and the grout (pH 11) is not in thermodynamic equilibrium

as shown by *Table 19*. The solution is supersaturated versus carbonates (calcite, Mg-calcite) and hydroxide (brucite, maybe M-S-H).

*Table 16 – Possible recipe for the young CEM I synthetic water for the BACUCE experiment at 20°C.*

Total conc.	[mmol.L <sup>-1</sup> ]	[mg.L <sup>-1</sup> ]
NaOH	50	2000
KOH	270	15120
Ca(OH) <sub>2</sub>	1.1	82
<i>+ optional</i>		
Na <sub>2</sub> SO <sub>4</sub>	1.1	156
NaCl	15	878

*Table 17 – Bulk recipe for the synthetic water of the bentonite/cement grout experiment at 20°C (i.e. for rehydrating the boreholes) without bacteria nutriments.*

Materials	Mass
Distilled water	5 L
<i>Salts</i>	
SiO <sub>2</sub>	311 mg
CaCl <sub>2</sub> ·2H <sub>2</sub> O	575 mg
CaCO <sub>3</sub>	206 mg
NaNO <sub>3</sub>	7.5 mg
Na <sub>2</sub> SO <sub>4</sub>	1779 mg
MgSO <sub>4</sub> ·7H <sub>2</sub> O	307 mg
NaHCO <sub>3</sub>	420 mg
NaCl	87.5 mg
KCl	27.5 mg
<i>pH adjusting</i>	
KOH 1M	3.79 mL
NaOH 1M	To reach pH 11

*Table 18 – Composition of the synthetic water of the grout BACUCE experiment (i.e. for rehydrating the boreholes) at 20°C.*

Total conc. [mmol.L <sup>-1</sup> ]	CEM I type	grout type
pH	13.5	11.0
(activity OH <sup>-</sup> )	(0.290)	(0.71×10 <sup>-3</sup> )
K <sup>+</sup>	270	0.83
Na <sup>+</sup>	50	8.3
Mg <sup>2+</sup>	-	0.25
Ca <sup>2+</sup>	1.1	1.19
HCO <sub>3</sub> <sup>-</sup>	-	1.41
H <sub>4</sub> SiO <sub>4</sub>	-	1.04
Cl <sup>-</sup>	-	1.94
SO <sub>4</sub> <sup>2-</sup>	-	2.75

*Table 19 – Saturation indices of the supersaturated phase for the grout-type synthetic water (BACUCE experiment).*

Minerals	Saturation index (20°C)
M-S-H 0.8	2.8
Dolomite (disordered)	2.5
Calcite	1.8
Magnesite	1.5
Brucite	0.5 – 1.8

Take away:

The in situ BACUCE experiments is at the core of the Subtask 2.2 project. It should bring new and relevant information on carbon steel corrosion under representative disposal conditions, in particular for the corrosion in the environment of bentonite/cement grout of rather low alkaline pH. The effect of a temperature of 80°C on the in situ evolution of the two types of steel/cement interface is also very promising. Most of the parameters required to develop a representative reactive transport model have been compiled in a consistent manner. Complementary information has been gained by preliminary modeling of the initial states that has been then used to help defining the synthetic water of the experiments. The model still needs to be improved by better considering the partial hydration of anhydrate components such as blast-furnace. The model will also benefit from the on-going lab experiment on the bentonite/grout evolution at 80°C and the characterization of the mill-scale effect typical of real untreated steels. Eventually, the HYTEC code is able to integrate in a unified model the physico-chemical properties of all the materials, the effect of temperature and the geometric configuration at both the in situ and lab scales. It is a necessary step for further interpreting the experimental in situ results once available, as well as for deconvoluting the coupling of chemical reactions in order to fit kinetic parameters.



## 6. Lab experiment on steel/CEM IIB interactions

*MINES ParisTech and MTA*

This chapter gives a synthetic overview of the material properties and experiments developed in SubTask 2.2 to gain information on the corrosion intensity of the S235JR carbon steel inserted in CEM IIB concrete, materials that are presently considered in the Hungarian disposal concept. The temperature of reference is 80°C for the sake of consistency and comparison with the other experiments of Subtask 2.2.

### 6.1 Experimental set-up

A schematic representation and picture of the experimental set-up with the Boda clay is given in *Figure 18*. The reactor cell as well as the materials within are designed such that the experimental set up represent an axisymmetric geometry. The first Teflon cylinder contains the carbon steel cylinder embedded in the concrete. There is an external Teflon cylinder filled with Boda water to keep water saturation degree circa 100 %. Holes of 0.7 mm in diameter on the first Teflon ensures the connection with the Boda water from the second Teflon cylinder. The Boda groundwater is also used for hydrating the cement.

### 6.2 Properties of the CEM II/B concrete

The filler material is a concrete made of CEM II/B (18 wt.%), silica sand/gravel (55 wt.%), limestone flour (15 wt.%) and water (11 wt.%), as reported in *Table 20*. The concrete is initially hydrated with the synthetic porewater of the Boda claystone. The CEM IIB/S chemistry is based on the study of Lubloy et al. (2016), but will be refined when more accurate data of the MTA experiment is available. For now, we define the CEM IIB/S concrete (32.5 R) as 72.5 wt.% OPC, 24.5 wt.% blast furnace slag, 3 wt.% limestone and 5 wt.% gypsum. *Table 21* gives the oxide contents.

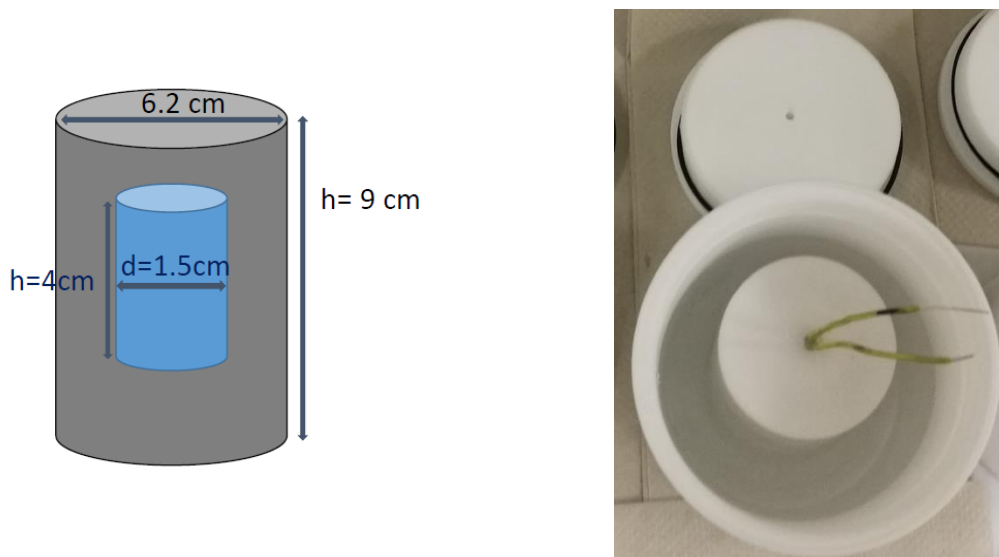


*Figure 18 – Steel/concrete experiment with the Boda clay: dimensions of the concrete cylinder in dark grey and steel cylinder in blue (left), and picture of the set-up (right).*

*Table 20 – Simplified composition of the CEM IIB concrete.*

Materials	Type	Mass [kg/m <sup>3</sup> ]
Additives	Sand (0/4)	921
	Gravel (4/8)	230
Cement	CEM II/B-S (42.5 N)	385
Limestone	Limestone flour	315
H <sub>2</sub> O	Drinking water quality	231
Admixtures	Silica fume	26

The hydrated cement phases and porewater chemistry have not been modeled yet. It will require a kinetic or partial hydration of the blast furnace slag present in CEM IIB. The porewater chemistry will be closed to the CEM I one, e.g. at a high pH of 13 approximately at 20°C.

*Table 21 – Bulk composition of the CEM IIB/S cement (Lubloy et al., 2016).*

Oxide	Content [wt.%]
SiO <sub>2</sub>	23.9
Al <sub>2</sub> O <sub>3</sub>	5.9
Fe <sub>2</sub> O <sub>3</sub>	2.6
CaO	55.3
MgO	4.2
SO <sub>3</sub>	3.0
K <sub>2</sub> O	0.4
Cl	0.002

### 6.3 Low-carbon steel

The steel is a grade of carbon steel (S235JR, S355JR) introduced as cylinder casks. The steel will be assumed as pure Fe(0) in the modeling but the corrosion rate will be set from the corrosion rate of the true steel.

### 6.4 Synthetic Boda claystone porewater

The Boda claystone is a very tight clayey rock with extreme low porosity (0.6-1.4%), nano-size pores, and very low permeability (10<sup>-11</sup> – 10<sup>-13</sup> m/s.). The diffusion is the dominating transport process (Németh et al., 2016; Fedor et al., 2018). The Boda claystone formation is ideal as a potential host rock for research towards the possibilities of high-level waste deposition in a geological formation in Hungary (Fedor et al., 2018).

The main rock-forming minerals of the Boda claystone formation are clay minerals, authigenic albite, detrital quartz, carbonate minerals (calcite, dolomite) and hematite. The clay mineral character of the Boda claystone is fundamentally illitic and some blocks also contain abundant analcime in addition to those minerals (Németh et al., 2016).

Table 22 details the hydrochemistry of the Boda claystone. Chloride content is moderate (23 mmol/l) but should not strongly enhance corrosion.

Table 22 – *Composition of reference for the porewater of the Boda claystone at 20°C.*

Aqueous species	Total concentration (mmol.L <sup>-1</sup> )
pH	8.0 <sup>(1)</sup>
K <sup>+</sup>	0.2
Na <sup>+</sup>	17
Mg <sup>2+</sup>	2.4
Ca <sup>2+</sup>	3.1
HCO <sub>3</sub> <sup>-</sup>	0.6
H <sub>4</sub> SiO <sub>4</sub>	-
Cl <sup>-</sup>	23
SO <sub>4</sub> <sup>2-</sup>	1.9

(1) In equilibrium with atmospheric CO<sub>2</sub>.

Take away:

Subtask 2.2 deals with a steel/cement interface representative of the Hungarian disposal concept, in particular another type of cement than the one used in the BACUCE project. A temperature of 80°C is also considered for the sake of consistency and comparison with the other experiments of Subtask 2.2.

## 7. Conclusion and Way forward

*MINES ParisTech and PSI*

### 7.1 Main conclusion

The thermodynamics of Fe-containing cement phases represents the first main result of the 1<sup>st</sup> year of the Task 2.2. Based on past investigations and preliminary scoping calculations, iron-siliceous-hydrogarnet is the most stable iron bearing cement hydrate phase. The presence of this phase was identified in cement paste hydrated for 10 and 50 years. Thermodynamically iron-siliceous-hydrogarnet is metastable compared to other iron hydroxide phases such as goethite and hematite (which should be switched off in calculations, at least below 80 °C). The presence of this phase keeps the dissolved iron in the pore solution at a low concentration ( $< 10^{-7}$  mol/kg at 25 °C), which decreases with increasing temperature due to the increase in the stability of the solid phase. The low iron concentration and the uptake in C-S-H, will have the effect of retaining the iron close to the cement/metal interface.

The new structurally consistent C-S-H model (Kulik et al., 2018; Miron et al., 2018b) has been extended for the uptake of Fe(III). Necessary endmembers were derived with estimated initial thermodynamic properties. The model contains additional interaction parameters. All parameters were successfully fitted against newly acquired experimental data on the Fe(III) uptake in C-S-H (Mancini et al., 2020a). After additional necessary estimates for the presence of iron and aluminum in C-S-H (not covered in the experiments) the model will be used to assess the impact of the iron in cement and on the stability of other Fe bearing phases.

For codes that cannot use non-ideal solid solution models an example for discretizing the nonideal C-S-H solid solution model is presented. A smart discretization procedure will be necessary for producing the optimal number of discrete phases that satisfactorily approximate the non-ideal solid solution model.

A second major contribution in Task 2.2 is to investigate the kinetics of the steel/cement interactions in the geologic disposal, and more specifically the corrosion rates of carbon steel in low-pH cements as well as in more usual CEM I and CEM IIB cements. A review of the literature has been discussed in the present report. At high pH, the steel is passivated by the deposition of a thin layer of magnetite corresponding to very small corrosion rates. Such beneficial alkaline conditions have been calculated to last for several dozens of thousand years, for instance in the supercontainer concept. It is generally assumed that the passivation of the steel becomes inactive when the alkaline pH decreases below 10.5. However, the corrosion rates under moderately alkaline pH (10.5 – 11.5) are not well characterized and will be obtained by the results of the BACUCE experiment of task 2.2. First results of the lab experiment of the BACUCE project at room temperature have been given in this report. Following the evolution with time of the corrosion rate will be an interesting output of the BACUCE experiment. Eventually, the cement/iron interaction should not lead to any significant consumption of iron by CEM I but it may be different in the case of the bentonite/cement grout due to the montmorillonite exchange capacity that can pump  $Fe^{2+}$  ions.

In addition to the corrosion rate, the effect of pH on corrosion may also modify the nature of the corrosion products at lower pH values. Along the same lines, the postmortem measurement of the porosity evolution at the interface will bring relevant insights for mass transfer and geochemical interactions. It is worth mentioning that CEM-I based paste or concrete, as well as bentonite/cement grout, are assumed to have no reducing capacity, e.g. the capabilities to consume any remaining oxygen within the borehole set-up. It could be interesting to assess the role of iron and iron corrosion products on the redox control of the porewater and the diffusion of dissolved iron in the cement/steel system. The initial state of the steel material can affect the steel/cement interactions. Relevant information will be provided by the experiments on the effect of mill scale on the corrosion rate and corrosion products of low carbon steel in similar conditions as the BACUCE experiments.

Almost all the physical and chemical parameters required for modeling the initial state geomaterials have been documented, partly from a literature review. This set of data covers the various material

studied in Task 2.2, i.e. CEM I paste, CEM II/B concrete, bentonite/cement grout, Toarcian argillite, and the BODA claystone. A third and main objective of the BACUCE experiment is to study the chemistry of cement/bentonite grout and its evolution with temperature. The physico-chemical properties of this low-pH material are still relatively unknown. The postmortem analysis of the solid phases as well as the recovery and analysis of the free water at the end of the test will help to better constrain the mineralogy and porewater chemistry and of the bentonite/cement grout at both 20°C and at the higher temperature of 80°C.

## 7.2 Planned continuation, improvements

There are no experimental data for the uptake of iron in the presence of aluminum and additional properties for the aluminum-iron C-S-H endmember need to be estimated. The model can then be used to assess the impact on the iron retention in cement and the stability of other iron cement hydrates.

Ways to incorporate the effect of the iron uptake in C-S-H to other geochemical modelling codes that do not use solid-solutions will be investigated. For producing the optimal number of discrete phases, a method of discretizing the C-S-H solid solution model as well as a smart discretization procedure is necessary. For phases such as (Al, Fe)-monosulfate and -ettringite that are currently defined in CEMDATA18 as non-ideal solid solutions, the impact of using ideal or non-ideal solid solutions on the modelled aqueous and solid composition will be also assessed.

The literature indicates that the hydrations of slag and silica fume are relatively slow at 20°C (about 1 year or more). It is probably less critical at 80°C but should still be evaluated. Therefore, the implementation of a kinetic approach will be performed in a next step of Subtask 2.2 for both the cement/bentonite grout (BACUCE experiment) and the CEM IIB concrete (MTA experiment). The modeling results will be adjusted on the future experimental data on the both the mineralogical evolution of the materials as well as the chemical analysis of the water reservoir or from the complementary batch experiment currently performed by Subatech within the Task 2 framework. Along the same lines, it is still feasible to simulate the evolution of the chemistry with the L/S ratio from 9 to 1 already acquired in the BACUCE project at 20°C (only L/S = 1 has been modeled so far, the most representative of the true porewater of the hydrated grout). The capability of the bentonite fraction of the grout to pump Fe(II) by sorption (cationic exchange) still needs to be validated.

The iron phases have not been considered in the modeling of the initial state of the cementitious materials yet, since they can generally be neglected in most applications. This is, however, relevant for the present study and will benefit from the review and selection of data on the Fe-cement phases. The discretization of the solid solution mentioned above will be used in this context.

The geochemical modeling of the formation of magnetite, of the stability of maghemite, and of the mean corrosion rate obtained in the lab experiment of BACUCE at 20°C is also under progress.

Eventually, modeling will take all its interest and strength when the first experimental data on the cement/steel interface will be available in the Subtask 2.2. The first data should be the in situ BACUCE experiment at 20°C that started before the beginning of the ACED WP. Possibly, while awaiting these new set of data, some working time can be devoted to complete the reactive transport modeling of the data acquired by IRSN on the dynamic of the corrosion layers at steel/argillite interface at 70°C during the PhD thesis of Chautard (2013). This will be useful for Subtask 2.1, but also partly recyclable for Subtask 2.2 depending whether complex corrosion layers will take place or not.

## 7.3 Missing data or process

There are no experimental data available on the fate of ferrous iron (Fe(II)) in cement phases, except recent experimental data for its uptake in C-S-H (Mancini et al. 2020b). Data on ferrous iron is for the most part restricted to the iron corrosion products (oxide/hydroxide/hydroxychloride phases). Most

metastable corrosion products do not have data on their temperature dependency. However, it is expected that the stable phases will predominantly form with increasing temperature.

Beside the dissolution in the aqueous phase of Fe(II) species from the metallic iron and the subsequent reprecipitation of corrosion product due to the diffusion of reactive species from the environment, the reactive transport model such HYTEC cannot simulate the electrochemical processes yet. A typical example is the implementation of the electric current inside the conductive metallic phase and the spatial decoupling of the cathodic and anodic reactions. It would be worth having a scientific survey of such modeling in Task 3 or in the other work packages of EURAD such as the DONUTS WP.

## 7.4 Information for Tasks 3 and 4

Subtask 2.2 will pass information from its relatively isolated small-scale processes investigated on interface scale to more complex systems at waste package scale (task 3) and disposal scale (task 4).

From the point of view of the experiments, advanced measurements techniques such as Extended X-ray Absorption Fine Structure (EXAFS) are required to better identify the Fe speciation in cement phases and corrosion products (see Vespa et al. 2015). These could complement standard techniques such as X-ray diffraction (XRD) and thermal analysis (DTA, TGA). Solid and pore solution composition should be measured (amounts of elements, Fe, pH, Eh, etc.). The concentration of iron dissolved could indirectly point out the stable solids. Subtask 2.2 will help to calibrate and refine the corrosion rates of steel under slightly alkaline conditions with respect to temperature, the pH and possibly imperfect contacts.

With respect to reactive transport modeling, the advance of chloride ions should be modelled as they play a role in the formation of soluble or less soluble iron bearing phases with an impact on the mobility of iron at the waste package scale. If solutions containing chloride ions reach the cement/steel interface these can lead to an increased corrosion rate also by raising the amount of dissolved iron in solution (as iron chloride species) and transporting it to areas favorable for mineral precipitation. The effect of iron-siliceous-hydrogarnet should be included in the modelling setup. Task 2.2 results will also provide a chemical model of the type of corrosion products and mineralogical evolution of cement materials with respect to temperature and spatial heterogeneity.

**Acknowledgements.** Alexandre Dautères and Diederick Jacques are gratefully acknowledged for their careful and relevant reviews that helped to enhance the consistency and accuracy of the report.

## References

- Aeppli M., Kaegi R., Kretzschmar R., Voegelin A., Hofstetter T.B., Sander M., 2019. Electrochemical Analysis of Changes in Iron Oxide Reducibility during Abiotic Ferrihydrite Transformation into Goethite and Magnetite. *Environ. Sci. Technol.* 53, 3568–3578.
- Andra, 2016. Safety Options Report - Operating Part (DoS-Expl). Report CG-TE-D-NTE-AMOA-SRr0000-5-0060, Andra, France.
- Angst, U.M., Geiker, M.R., Michel, A. et al., 2017. The steel–concrete interface. *Mater Struct* 50, 143. <https://doi.org/10.1617/s11527-017-1010-1>
- Baes, C.F., Mesmer, R.E., 1977. *The Hydrolysis of Cations*. Wiley-Blackwell. <https://doi.org/10.1002/bbpc.19770810252>
- Bagnoud, A., Chourey, K., Hettich, R.L., De Bruijn, I., Andersson, A.F., Leupin, O.X., Schwyn, B., Bernier-Latmani, R., 2016. Reconstructing a hydrogen-driven microbial metabolic network in Opalinus Clay rock, in: *Nature Communications*. Nature Publishing Group, pp. 1–10. <https://doi.org/10.1038/ncomms12770>
- Barbarulo, R., Peycelon, H., Leclercq, S., 2007. Chemical equilibria between C–S–H and ettringite, at 20 and 85 C. *Cement and Concrete Research*, 37 1176–1181.
- Bataillon, C., Bouchon, F., Chainais-Hillairet, C., Fuhrmann, J., Hoarau E., Touzani, R., 2012. Numerical methods for the simulation of a corrosion model with moving oxide boundaries. *Journal of Computational Physics* 231, 6213–6231.
- Berman, R.G., 1990. Mixing properties of Ca-Mg-Fe-Mn garnets. *Am. Mineral.* 75(3-4), 328–344.
- Berman, R.G., Brown, T.H., 1984. A thermodynamic model for multicomponent melts, with application to the system CaO-Al<sub>2</sub>O<sub>3</sub>-SiO<sub>2</sub>. *Geochim. Cosmochim. Acta* 48, 661–678. [https://doi.org/10.1016/0016-7037\(84\)90094-2](https://doi.org/10.1016/0016-7037(84)90094-2)
- Betelu, S., Lerouge, C., Ignatiadis, I., Berger, G., Giffaut, E., 2012. Mechanistic study of pyrite reduction by hydrogen in NaCl 0.1 M at 90 °C using Electrochemical techniques. Book of abstracts. *Clays in natural and engineered barriers for radioactive waste confinement - 5. International meeting*.
- Bildstein, O., Claret, F., Frugier, P., 2019. RTM for Waste Repositories. *Reviews in Mineralogy and Geochemistry* 85, 419–457.
- Blanc, P., Lassin, A., Piantone, P., Azaroual, M., Jacquemet, N., Fabbri, A., Gaucher, E. C., 2012. Thermoddem: A geochemical database focused on low temperature water/rock interactions and waste materials. *Appl. Geochem.* 27, 2107–2116. <https://doi.org/10.1016/j.apgeochem.2012.06.002>
- Bodén, A., Pettersson, S., 2011. Development of rock bolt grout and shotcrete for rock support and corrosion of steel in low-pH cementitious materials. Report SKB R-11-08, SKB, Sweden.
- Boylan, A.A., Perez-Mon, C., Guillard, L., Burzan, N., Loreggian, L., Maisch, M., Kappler, A., Byrne, J.M., Bernier-Latmani, R., 2019. H<sub>2</sub>-fuelled microbial metabolism in Opalinus Clay. *Appl. Clay Sci.* 174, 69–76.
- Bradbury, M.H., Baeyens, B., 2002. Sorption of Eu on Na- and Ca-montmorillonites: Experimental investigations and modelling with cation exchange and surface complexation. *Geochimica et Cosmochimica Acta* 66, 2325–2334.
- Bullard, J.W., Scherer, G.W., Viehland, D., 2016. An ideal solid solution model for C–S–H. *J. Am. Ceram. Soc.* 99, 4137–4145. <https://doi.org/10.1111/jace.14493>
- Carey, J.W., Lichtner, P.C., 2007. Calcium silicate hydrate (C-S-H) solid solution model applied to cement degradation using the continuum reactive transport model FLOTRAN, in: Mobasher, B., Skalny, J. (Eds.), *Transport Properties and Concrete Quality: Materials Science of Concrete*, Special Volume. John Wiley & Sons, Ltd.

- Chautard, C. (2013). Interactions fer/argile en conditions de stockage géologique profond – Impacts d'activités bactériennes et d'hétérogénéités. PhD thesis, Ecole des Mines de Paris, Paris (France).
- Chaves, L.H.G., 2005. The role of green rust in the environment: a review. *Rev. Bras. Eng. Agrícola e Ambient.* 9, 284–288. <https://doi.org/10.1590/s1415-43662005000200021>
- Cloet, V., Pekala, M., Smith, P., Wersin, P., Diomidis, N., 2017. An evaluation of sulphide fluxes in the near field of a HLW repository. Nagra Technical Report NTB 17-04, Nagra Wettingen, Switzerland.
- Cox, J.D., Wagman, D.D., Medvedev, V.A. (Vadim A., 1989. CODATA key values for thermodynamics. Hemisphere Pub. Corp, New York.
- Craeye, B., De Schutter, G., Van Humbeeck, H., Van Cotthem, A., 2009. Early age behaviour of concrete supercontainers for radioactive waste disposal. *Nuclear Engineering and Design* 239, 23–35.
- Cudennec Y., Lecerf A., 2006. The transformation of ferrihydrite into goethite or hematite, revisited. *J. Solid State Chem.* 179, 716–722.
- de Combarieu, G., Barboux, P., Minet, Y., 2007. Iron corrosion in Callovo-Oxfordian argillite: From experiments to thermodynamic/kinetic modelling. *Phys. Chem. Earth* 32, 346–358.
- de Combarieu, G., Schlegel, M. L., Neff, D., Foy, E., Vantelon, D., Barboux, P., Gin, S., 2011. Glass-iron-clay interactions in a radioactive waste geological disposal: An integrated laboratory-scale experiment. *Applied Geochemistry* 26, 65–79.
- Deissmann, G., Haneke, K., Filby, A., Wieggers, R., 2016. Dissolution behaviour of HLW glasses under OPERA repository conditions. Report OPERA-PU-IBR511A.
- Deissmann G., Ait Mouheb N., Martin C., Name N., Jacques, D., Weetjens E., Kursten B., Leivo M., Somervuori, M., Carpen, L., 2020. Experiments and numerical model studies on interfaces. Final version as of xx.xx.xxxx of deliverable D2.5 of the HORIZON 2020 project EURAD. EC Grant agreement no: 847593.
- De Windt, L., Cabrera, J., Boisson, J.Y., 1999. Radioactive waste containment in indurated claystones: comparison between the chemical containment properties of matrix and fractures, in: R. Metcalfe, C.A. Rochelle (Eds.). *Chemical Containment of Waste in the Geosphere*, 157 Geological Society of London Special Publication, 1999, 167–181.
- De Windt, L., Pellegrini, D., van der Lee, J. (2004). Coupled modeling of cement/ claystone interactions and radionuclides migration, *Journal of Contaminant Hydrology* 68, 165–182.
- De Windt, L., Marsal, F., Tinseau, E., Pellegrini, D., 2008. Reactive transport modeling of geochemical interactions at a concrete/argillite interface, Tournemire site (France). *Physics and Chemistry of the Earth* 33, 295–305.
- De Windt, L., Marsal, F., Corvisier, J., Pellegrini, D. (2014). Modeling of oxygen gas diffusion and consumption during the oxic transient in a disposal cell of radioactive waste. *Applied Geochemistry* 41, 115–127.
- De Windt, L., Spycher, N., 2019. Reactive transport models for long-term safety assessment of nuclear waste disposal. *Elements* 15, 99–102.
- Dilnesa, B.Z., 2012. Fe-containing Hydrates and their Fate during Cement Hydration. <https://doi.org/10.5075/EPFL-THESIS-5262>
- Dilnesa, B.Z., Lothenbach, B., Le Saout, G., Renaudin, G., Mesbah, A., Filinchuk, Y., Wichser, A., Wieland, E., 2011. Iron in carbonate containing AFm phases. *Cem. Concr. Res.* 41, 311–323. <https://doi.org/10.1016/j.cemconres.2010.11.017>
- Dilnesa, B.Z., Lothenbach, B., Renaudin, G., Wichser, A., Kulik, D., 2014a. Synthesis and characterization of hydrogarnet  $\text{Ca}_3(\text{Al}_x\text{Fe}_{1-x})_2(\text{SiO}_4)_y(\text{OH})_{4(3-y)}$ . *Cem. Concr. Res.* 59, 96–111. <https://doi.org/10.1016/j.cemconres.2014.02.001>

- Dilnesa, B.Z., Lothenbach, B., Renaudin, G., Wichser, A., Wieland, E., 2012. Stability of monosulfate in the presence of iron. *J. Am. Ceram. Soc.* 95, 3305–3316. <https://doi.org/10.1111/j.1551-2916.2012.05335.x>
- Dilnesa, B.Z., Wieland, E., Lothenbach, B., Dähn, R., Scrivener, K.L., 2014b. Fe-containing phases in hydrated cements. *Cem. Concr. Res.* 58, 45–55. <https://doi.org/10.1016/j.cemconres.2013.12.012>
- Diomidis, N., 2014. Scientific Basis for the Production of Gas due to Corrosion in a Deep Geological Repository. Nagra Work Report NAB 14-21, Nagra, Wettingen, Switzerland.
- Diomidis, N., Cloet, V., Leupin, O.X., Marschall, P., Poller, A., Stein, M., 2016. Production, consumption and transport of gases in deep geological repositories according to the Swiss disposal concept. Nagra Technical Report NTB 16-03, Nagra, Wettingen, Switzerland.
- Divet, L., Randriambololona, R., 1998. Delayed ettringite formation: The effect of temperature and basicity on the interaction of sulphate and C-S-H Phase 1. *Cement and Concrete Research* 28, 357–363.
- Duro, L., Bruno, J., Grivé, M., Montoya, V., Kienzler, B., Altmaier, M., Buckau, G., 2014. Redox processes in the safety case of deep geological repositories of radioactive wastes. Contribution of the European RECOZY Collaborative Project. *Appl. Geochemistry* 49, 206–217. <https://doi.org/10.1016/j.apgeochem.2014.04.013>
- Elakneswaran, Y., Noguchi, N., Matumoto, K., Morinaga, Y., Chabayashi, T., Kato, H., Nawa, T., 2019. Characteristics of ferrite-rich Portland cement: Comparison with ordinary Portland cement. *Front. Mater.* 6, 97. <https://doi.org/10.3389/fmats.2019.00097>
- Erbs, M., 2004. Formation and redox reactions of green rusts under geochemical conditions found in natural soils and sediments. (Doctoral dissertation). ETH Zürich, Zürich, 167 p.
- Faucon, P., Le Bescop, P., Adenot, F., Bonville, P., Jacquinet, J.F., Pineau, F., Felix, B., 1996. Leaching of cement: Study of the surface layer. *Cem. Concr. Res.* 26, 1707–1715. [https://doi.org/10.1016/S0008-8846\(96\)00157-3](https://doi.org/10.1016/S0008-8846(96)00157-3)
- Fedor, F., Máthé, Z., Ács, P., Koroncz, P. 2018. New results of Boda Claystone research: Genesis, mineralogy, geochemistry, petrophysics. Geological Society, London, Special Publications, 482, 75–92, <https://doi.org/10.1144/SP482.13>
- Féron, D., Crusset, D., Gras, J.-M., 2008. Corrosion issues in nuclear waste disposal. *J. Nucl. Mater.* 379, 16–23.
- Frugier, P., Gin, S., Minet, Y., Chave, T., Bonin, B., Godon, N., Lartigue, J.E., Jollivet, P., Ayrat, A., De Windt, L., Santarini, G. (2008). SON68 nuclear glass dissolution kinetics: Current state of knowledge and basis of the new GRAAL model. *Journal of Nuclear Materials* 380, 8–21.
- García Calvo, J.L., Sánchez Moreno, M., Alonso Alonso, M.C., Hidalgo López, A., García Olmo, J., 2013. Study of the Microstructure Evolution of Low-pH Cements Based on Ordinary Portland Cement (OPC) by Mid- and Near-Infrared Spectroscopy, and Their Influence on Corrosion of Steel Reinforcement. *Materials* 6, 2508–2521.
- Giffaut, E., Grivé, M., Blanc, P., Vieillard, P., Colàs, E., Gailhanou, H., Gaboreau, S., Marty, N., Madé, B., Duro, L., 2019. Andra thermodynamic database for performance assessment: ThermoChimie, *Appl. Geochem.* 49, 225–236. doi:10.1016/j.apgeochem.2014.05.007.
- Glynn, P., 2019. Solid-solution solubilities and thermodynamics: Sulfates, carbonates and halides, in: *Sulfate Minerals: Crystallography, Geochemistry, and Environmental Significance*. Walter de Gruyter GmbH, pp. 481–511. <https://doi.org/10.2138/rmg.2000.40.10>
- Grousset, S., Wittebroodt, C., Dauzères, A., Urios, L., 2018. Study of bacterial anoxic corrosion in cementitious environment. RILEM 253-MCI Conference on Microorganisms-Cementitious Materials Interactions, 25-27 June, Toulouse (France).

- Grousset, S., 2019. Impacts des micro-organismes sur la corrosion en milieu alcalin. Rapport IRSN, Fontenay-aux-Roses (France).
- Gruskovnjak A., B. Lothenbach, F. Winnefeld, R. Figi, S.C. Ko, M. Adler, U. Mäder, Hydration mechanisms of super sulphated slag cement, *Cem. Concr. Res.*, 38 (2008) 983-992.
- Helgeson, H.C., Delany, J.M., Nesbitt, H.W., Bird, D.K., 1978. Summary and critique of the thermodynamic properties of rock-forming minerals. *Am. J. Sci.* 278A, 1–229.
- Hummel, W., Berner, U., Curti, E., Pearson, F.J., Thoenen, T., 2002. Nagra/PSI Chemical Thermodynamic Data Base 01/01. *Radiochim. Acta* 90, 805–813. [https://doi.org/10.1524/ract.2002.90.9-11\\_2002.805](https://doi.org/10.1524/ract.2002.90.9-11_2002.805)
- Idiart A., Laviña M., 2019. Final results and main outcomes of the Modelling Task. Deliverable n°D3.07. CEBAMA European Project n° 662147.
- Idiart, A., Laviña, M., Kosakowski, G. et al., 2020. Reactive transport modelling of a low-pH concrete/clay interface. *Applied Geochemistry* 115, 104562.
- Johnson, J.W., Oelkers, E.H., Helgeson, H.C., 1992. SUPCRT92: A software package for calculating the standard molal thermodynamic properties of minerals, gases, aqueous species, and reactions from 1 to 5000 bar and 0 to 1000°C. *Comput. Geosci.* 18, 899–947. [https://doi.org/10.1016/0098-3004\(92\)90029-Q](https://doi.org/10.1016/0098-3004(92)90029-Q)
- Kayali, O., Khan, M.S.H., Sharfuddin Ahmed, M., 2012. The role of hydrotalcite in chloride binding and corrosion protection in concretes with ground granulated blast furnace slag. *Cem. Concr. Compos.* 34, 936–945. <https://doi.org/10.1016/j.cemconcomp.2012.04.009>
- King, F., 2008. Corrosion of carbon steel under anaerobic conditions in a repository for SF and HLW in Opalinus Clay. Nagra Technical Report NTB 08-12, Nagra, Wettingen, Switzerland.
- Knauss, K.G., Wolery, T.J., 1988. The dissolution kinetics of quartz as a function of pH and time at 70 C. *Geochimica et Cosmochimica Acta* 52, 43–53.
- Köhler, S.J., Dufaud, F., Oelkers, E.H., 2003. An experimental study of illite dissolution kinetics as a function of pH from 1.4 to 12.4 and temperature from 5 to 50 C. *Geochimica et Cosmochimica Acta*, 67, 3583–3594.
- Kosakowski, G., Berner, U., Wieland, E., Glaus, M., Degueudre, C., 2014. Geochemical Evolution of the L/ILW Near-field. Nagra Technical Report NTB 14-11, Nagra, Wettingen, Switzerland.
- Kulik, D.A., 2011. Improving the structural consistency of C-S-H solid solution thermodynamic models. *Cem. Concr. Res.* 41, 477–495. <https://doi.org/10.1016/j.cemconres.2011.01.012>
- Kulik, D.A., Kersten, M., 2001. Aqueous solubility diagrams for cementitious waste stabilization systems: II, End-Member stoichiometries of ideal calcium silicate hydrate solid solutions. *J. Am. Ceram. Soc.* 84, 3017–3026. <https://doi.org/10.1111/j.1151-2916.2001.tb01130.x>
- Kulik, D.A., Miron, G.D., Lothenbach, B., 2018. A realistic three-site solid solution model of C-S-H, in: *Goldschmidt Abstracts*, 2018 1364.
- Kulik, D.A., Wagner, T., Dmytrieva, S. V., Kosakowski, G., Hingerl, F.F., Chudnenko, K. V., Berner, U.R., 2013. GEM-Selektor geochemical modeling package: Revised algorithm and GEMS3K numerical kernel for coupled simulation codes. *Comput. Geosci.* <https://doi.org/10.1007/s10596-012-9310-6>
- Kulik, D.A., Wagner, T., Dmytrieva, S. V., Kosakowski, G., Hingerl, F.F., Chudnenko, K. V., Berner, U.R., 2012. GEM-Selektor geochemical modeling package: revised algorithm and GEMS3K numerical kernel for coupled simulation codes. *Comput. Geosci.* 17, 1–24. <https://doi.org/10.1007/s10596-012-9310-6>
- Kunhi Mohamed, A., Moutzouri, P., Berruyer, P., Walder, B.J., Siramanont, J., Harris, M., Negroni, M., Galmarini, S.C., Parker, S.C., Scrivener, K.L., Emsley, L., Bowen, P., 2020. The atomic-level

- structure of cementitious calcium aluminate silicate hydrate. *J. Am. Chem. Soc.* <https://doi.org/10.1021/jacs.0c02988>
- Kunhi Mohamed, A., Parker, S.C., Bowen, P., Galmarini, S., 2018. An atomistic building block description of C-S-H - Towards a realistic C-S-H model. *Cem. Concr. Res.* 107, 221–235. <https://doi.org/10.1016/J.CEMCONRES.2018.01.007>
- Kursten, B., Smailos, E., Azkarate, I., Werme, L., Smart, N., Santarini, G., 2004. COBECOMA: state of art document on the CORrosion BEhaviour of CONtainer MAterials. EC, Luxemburg.
- Kursten, B., Druyts, F. (2015). Assessment of the uniform corrosion behaviour of carbon steel radioactive waste packages with respect to the disposal concept in the geological Dutch Boom Clay formation. Report OPERA-PU-SCK513, Netherlands.
- Labhasetwar, N.K., Shrivastava, O.P., Medikov, Y.Y., 1991. Mössbauer study on iron-exchanged calcium silicate hydrate:  $\text{Ca}_{5-x}\text{Fe}_x\text{Si}_6\text{O}_{18}\text{H}_2 \cdot n\text{H}_2\text{O}$ . *J. Solid State Chem.* 93, 82–87. [https://doi.org/10.1016/0022-4596\(91\)90277-O](https://doi.org/10.1016/0022-4596(91)90277-O)
- Landolt, D., 2007. Corrosion and surface chemistry of metals, *Corrosion and Surface Chemistry of Metals*. EPFL Press. <https://doi.org/10.5860/choice.45-0897>
- Lalan, P., 2016. Influence d'une température de 70 °C sur la géochimie, la microstructure et la diffusion aux interfaces béton / argile : expérimentations en laboratoire, in situ et modélisation. PhD thesis, MINES ParisTech, Paris (France).
- Lalan, P., Dauzères, A., De Windt, L., Bartier, D., Sammaljärvi, J., Barnichon, J.D., Techer, I., Detilleux, V., 2016. Impact of a 70 °C temperature on an ordinary Portland cement paste/claystone interface: An in situ experiment, *Cement and Concrete Research* 83, 164-178.
- Lalan, P., Dauzères, A., De Windt, L., Sammaljärvi, J., Bartier, D., Techer, I., Detilleux, V., Siitari-Kauppi, M., 2019. Mineralogical and microstructural evolution of Portland cement paste/argillite interfaces at 70 °C – Considerations for diffusion and porosity properties. *Cement and Concrete Research* 115, 414–425.
- Lemire, R.J., Berner, U., Musikas, C., Palmer, D.A., Taylor, P., Tochiyama, O., 2013. Chemical thermodynamics of iron Part 1. *Chem. Thermodyn.* 13a, 1–1082. <https://doi.org/NEA No. 6355>
- Leupin, O.X., Bernier-Latmani, R., Bagnoud, A., Moors, H., Leys, N., Wouters, K., Stroes-Gascoyne, S., 2017. Fifteen years of microbiological investigation in Opalinus Clay at the Mont Terri rock laboratory (Switzerland). *Swiss J. Geosci.* 110, 343–354. <https://doi.org/10.1007/s00015-016-0255-y>
- Lichtner, P.C., Carey, J.W., 2006. Incorporating solid solutions in reactive transport equations using a kinetic discrete-composition approach. *Geochim. Cosmochim. Acta* 70, 1356–1378. <https://doi.org/10.1016/j.gca.2005.11.028>
- Lothenbach, B., Kulik, D.A., Matschei, T., Balonis, M., Baquerizo, L., Dilnesa, B., Miron, G.D., Myers, R.J., 2019. Cemdata18: A chemical thermodynamic database for hydrated Portland cements and alkali-activated materials. *Cem. Concr. Res.* 115, 472–506. <https://doi.org/10.1016/j.cemconres.2018.04.018>
- Lothenbach, B., Gruskovnjak, A., 2007. Hydration of alkali-activated slag: thermodynamic modelling, *Adv. Cem. Res.*, 19, 81-92.
- Lothenbach, B., Matschei, T., Möschner, G., Glasser, F.P., 2008. Thermodynamic modelling of the effect of temperature on the hydration and porosity of Portland cement. *Cem. Concr. Res.* 38, 1–18. <https://doi.org/10.1016/j.cemconres.2007.08.017>
- Lothenbach, B., Nonat, A., 2015. Calcium silicate hydrates: Solid and liquid phase composition. *Cem. Concr. Res.* 78, 57–70. <https://doi.org/10.1016/J.CEMCONRES.2015.03.019>

- Lothenbach, B., Winnefeld, F., 2006. Thermodynamic modelling of the hydration of Portland cement. *Cem. Concr. Res.* 36, 209–226. <https://doi.org/10.1016/j.cemconres.2005.03.001>
- Lubloy, E., Kopecsko, K., Balazs, G.L., Szilagyi, I.M., Madarasz, J., 2016. Improved fire resistance by using slag cements. *J. Therm. Anal. Calorim.* 125, 271–279. DOI 10.1007/s10973-016-5392-z
- Mäder, U., Jenni, A., Lerouge, C., Gaboreau, S., Miyoshi, S., Kimura, Y., Cloet, V., Fukaya, M., Claret, F., Otake, T., Shibata, M., Lothenbach, B., 2017. 5-year chemico-physical evolution of concrete–claystone interfaces, Mont Terri rock laboratory (Switzerland). *Swiss J. Geosci.* 110, 307–327. <https://doi.org/10.1007/s00015-016-0240-5>
- Mahallati, E., Saremi, M., 2006. An assessment on the mill scale effects on the electrochemical characteristics of steel bars in concrete under DC-polarization. *Cement and Concrete Research* 36, 1324-1329. <https://doi.org/10.1016/j.cemconres.2006.03.015>
- Mammoliti, L.T, Brown, L.C, Hansson, C.M, Hope, B.B., 1996. The influence of surface finish of reinforcing steel and pH of the test solution on the chloride threshold concentration for corrosion initiation in synthetic pore solutions. *Cement and Concrete Research* 26, 545–550.
- Mancini, A., Wieland, E., Geng, G., Dähn, R., Skibsted, J., Wehrli, B., Lothenbach, B., 2020. Fe(III) uptake by calcium silicate hydrates. *Appl. Geochemistry* 113, 104460. <https://doi.org/10.1016/j.apgeochem.2019.104460>
- Mancini, A., E. Wieland, G. Geng, B. Lothenbach, B. Wehrli, R. Dähn, XAFS spectroscopy and wet chemical studies on Fe(II) interaction with cement phases. *Cem. Concr. Res.* (2020) (submitted).
- Marques Fernandes, M., Baeyens, B., Dähn, R., Scheinost, A.C., Bradbury, M.H., 2012. U(VI) Sorption on Montmorillonite in the Absence and Presence of Carbonate: A Macroscopic and Microscopic Study. *Geochimica et Cosmochimica Acta* 93, 262–277.
- Marty, N.C.M., Bildstein, O., Blanc, P. *et al.* (2015). Benchmarks for multicomponent reactive transport across a cement/clay interface. *Comput Geosci* 19, 635–653.
- Michau, N., Bourbon, X., 2016. Coulis cimentaire pour remplissage d'un espace annulaire autour d'une alvéole de stockage de déchets radioactifs creusée dans un milieu argileux. Brevet FR 3 031 103 - A1, INPI, France.
- Miron, G.D., Kulik, D.A., Dmytrieva, S. V., Wagner, T., 2015. GEMSFITS: Code package for optimization of geochemical model parameters and inverse modeling. *Appl. Geochemistry* 55, 28–45. <https://doi.org/10.1016/J.APGEOCHEM.2014.10.013>
- Miron, G.D., Kulik, D.A., Lothenbach, B., 2018a. A PHREEQC version of CEMDATA'18 generated using ThermoMatch, in: *Calcium-Silicate Hydrates Containing Aluminium: C-A-S-H II*. Dübendorf, Switzerland.
- Miron, G.D., Kulik, D.A., Lothenbach, B., 2018b. Parameterization of a new C-S-H solid solution model for alkali uptake. *Goldschmidt Abstr.* 2018 1778.
- Missana, T., García-Gutiérrez, M., Mingarro, M., Alonso, U., 2018. Comparison between cesium and sodium retention on calcium silicate hydrate (C–S–H) phases. *Appl. Geochemistry* 98, 36–44. <https://doi.org/10.1016/j.apgeochem.2018.09.007>
- Möschner, G., B. Lothenbach, J. Rose, A. Ulrich, R. Figi, R. Kretzschmar, 2008. Solubility of Fe-ettringite ( $\text{Ca}_6[\text{Fe}(\text{OH})_6]_2(\text{SO}_4)_3 \cdot 26\text{H}_2\text{O}$ ). *Geochim. Cosmochim. Acta* 72, 1-18.
- Möschner, G., Lothenbach, B., Winnefeld, F., Ulrich, A., Figi, R., Kretzschmar, R., 2009. Solid solution between Al-ettringite and Fe-ettringite ( $\text{Ca}_6[\text{Al}_{1-x}\text{Fe}_x(\text{OH})_6]_2(\text{SO}_4)_3 \cdot 26\text{H}_2\text{O}$ ). *Cem. Concr. Res.* 39, 482–489. <https://doi.org/10.1016/j.cemconres.2009.03.001>

- Motellier, S., Devol-Brown, I., Savoye, S., Thoby, D., Alberto, J.C., 2007. Evaluation of tritiated water diffusion through the Toarcian clayey formation of the Tournemire experimental site (France). *J. Contam. Hydrol.* 94, 99–108.
- Myers, R.J., Bernal, S.A., Provis, J.L., 2014. A thermodynamic model for C-(N-)A-S-H gel: CNASH\_ss. Derivation and validation. *Cem. Concr. Res.* 66, 27–47. <https://doi.org/10.1016/J.CEMCONRES.2014.07.005>
- Necib, S., Linard, Y., Crusset, D., Michau, N., Dumas, S., Burger, E., Romaine, A., Schlegel, M.L., 2016. Corrosion at the carbon steel–clay borehole water and gas interfaces at 85 °C under anoxic
- Neeft, E., Weetjens, E., Vokal, A., Leivo, M., Cochapin, B., Martin, C., Munier, I., Deissmann, G., Montoya, V., Poskas, P., Grigaliuniene, D., Narkuniene, A., Garcia, E., Samper, J., Montenegro, L., Mon, A., 2019. Treatment of chemical evolution in National Programmes, D 2.4 of the HORIZON 2020 project EURAD. EC Grant agreement no: 847593.
- Neeft E., Jacques D., Deissmann G., 2020. State of the art of the assessment of the chemical evolution of ILW and HLW disposal cells. D2.1 of the HORIZON 2020 project EURAD. EC Grant agreement no: 847593.
- Nemer, M.B., Xiong, Y., Ismail, A.E., Jang, J.H., 2011. Solubility of  $\text{Fe}_2(\text{OH})_3\text{Cl}$  (pure-iron end-member of hibbingite) in NaCl and  $\text{Na}_2\text{SO}_4$  brines. *Chem. Geol.* 280, 26–32. <https://doi.org/10.1016/j.chemgeo.2010.10.003>
- Németh, T., Máthé, Z., Pekker, P., Dódony, I., Kovács-Kis, V., Sipos, P., Cora, I., Kovács, I., 2016. Clay mineralogy of the Boda Claystone Formation (Mecsek Mts., SW Hungary). *Open Geosciences* 8, 259–274.
- Nordstrom, D.K., Plummer, L.N., Langmuir, D., Busenberg, E., May, H.M., Jones, B.F., Parkhurst, D.L., 1990. Revised Chemical Equilibrium Data for Major Water—Mineral Reactions and Their Limitations. pp. 398–413. <https://doi.org/10.1021/bk-1990-0416.ch031>
- Odorowski, M., Jégou, C., De Windt, L., Broudic, V., Jouan, G., Peugeot, S., Martin, C., 2017. Effect of metallic iron on the oxidative dissolution of  $\text{UO}_2$  doped with a radioactive alpha emitter in synthetic Callovian-Oxfordian groundwater. *Geochim. Cosmochim. Acta* 219, 1–21. <https://doi.org/10.1016/j.gca.2017.08.043>
- Page, C., Short, N., El Tarras, A., 1981. Diffusion of chloride ions in hardened cement pastes. *Cement and Concrete Research* 11, 395–406.
- Palandri, J.L., Kharaka, Y.K., 2004. A compilation of rate parameters of water-mineral interaction kinetics for application to geochemical modeling. Open file report 2004-1068, U.S. Geological Survey.
- Papillon, F., Jullien, M., Bataillon, C., 2003. Carbon steel behaviour in compacted clay: Two long term tests for corrosion prediction. International workshop 'Prediction of Long Term Corrosion Behaviour in Nuclear Waste Systems'; Cadarache (France) p. 439-454.
- Parkhurst, D.L., Appelo, C. a. J., 2013. Description of Input and Examples for PHREEQC Version 3 — A Computer Program for Speciation, Batch-Reaction, One-Dimensional Transport, and Inverse Geochemical Calculations. U.S. Geological Survey Techniques and Methods, book 6, chapter A43, 497 p., Techniques and Methods, book 6, chapter A43. U.S. Geological Survey.
- Pearson, F.J., Berner, U., 1991. Nagra Thermochemical Data Base I. Core Data. Nagra Technical Report NTB 91-17. Nagra, Wetingen, Switzerland.
- Pearson, F.J., Berner, U., Hummel, W., 1992. Nagra Thermochemical Data Base II. Supplemental Data 05/92. Nagra Technical Report NTB 91-18. Nagra, Wetingen, Switzerland.
- Poursae, A., 2016. Corrosion of steel in concrete structures, in: *Corrosion of Steel in Concrete Structures*. Elsevier Inc., pp. 19–33. <https://doi.org/10.1016/B978-1-78242-381-2.00002-X>

- Refait, P., Memet, J.B., Bon, C., Sabot, R., Génin, J.M.R., 2003. Formation of the Fe(II)–Fe(III) hydroxysulphate green rust during marine corrosion of steel. *Corros. Sci.* 45, 833–845. [https://doi.org/10.1016/S0010-938X\(02\)00184-1](https://doi.org/10.1016/S0010-938X(02)00184-1)
- Réguer, S., Mirambet, F., Rémazeilles, C., Vantelon, D., Kergourlay, F., Neff, D., Dillmann, P., 2015. Iron corrosion in archaeological context: Structural refinement of the ferrous hydroxychloride  $\beta$  Fe<sub>2</sub>(OH)<sub>3</sub>Cl. *Corros. Sci.* 100, 589–598. <https://doi.org/10.1016/j.corsci.2015.08.035>
- Rémazeilles, C., Refait, P., 2007. On the formation of  $\beta$ -FeOOH (akaganéite) in chloride-containing environments. *Corros. Sci.* 49, 844–857. <https://doi.org/10.1016/j.corsci.2006.06.003>
- Robie, R., Hemingway, B.S., 1995. *Thermodynamic Properties of Minerals and Related Substances at 298.15K and 1 Bar*. U.S. Geol. Surv. Bull.
- Rozov, K.B., Berner, U., Kulik, D.A., Diamond, L.W., 2011. Solubility and thermodynamic properties of carbonate-bearing hydrotalcite-pyroaurite solid solutions with a 3:1 Mg/(Al+Fe) mole ratio. *Clays Clay Miner.* 59, 215–232. <https://doi.org/10.1346/CCMN.2011.0590301>
- Sagoe-Crentsil, K.K., Glasser, F.P., 1993. “Green rust”, iron solubility and the role of chloride in the corrosion of steel at high pH. *Cem. Concr. Res.* 23, 785–791. [https://doi.org/10.1016/0008-8846\(93\)90032-5](https://doi.org/10.1016/0008-8846(93)90032-5)
- Saheb, M., D. Neff, P. Dillmann, H. Matthiesen, E. Foy, 2008. Long-term corrosion behaviour of low-carbon steel in anoxic environment: characterisation of archaeological artefacts. *J. Nucl. Mater.* 379, 118-123.
- Saheb, M., Gallien, J.P., Descostes, M., Raimbault, L., Perez, A., Neff, D., Marsal, F., Pellegrini, D., Dillmann, P., 2014. Influence of an aerated/anoxic transient phase on the long-term corrosion of iron. *Corros. Sci.* 86, 71–80. <https://doi.org/10.1016/j.corsci.2014.04.040>
- Savoie, S., Goutelard, F., Beaucaire, C., Charles, Y., Fayette, A., Herbette, M., Larabi, Y., Coelho, D., 2011. Effect of temperature on the containment properties of argillaceous rocks: The case study of Callovo–Oxfordian claystones. *Journal of Contaminant Hydrology* 125, 102–112.
- Shabalín, B.H., Lavrynenko, O.M., Pavlenko, O.Y., 2019. Development of the nano-mineral phases at the steel-bentonite interface in time of the evolution of geological repository for radioactive waste, in: *Springer Proceedings in Physics*. Springer Science and Business Media, LLC, pp. 29–44. [https://doi.org/10.1007/978-3-030-17759-1\\_2](https://doi.org/10.1007/978-3-030-17759-1_2)
- Smart, N.R., Blackwood, D.J., Marsh, G.P., Naish, C.C., O'Brien, T.M., Rance, A.P., Thomas, M.I., 2004. *The Anaerobic Corrosion of Carbon and Stainless Steels in Simulated Cementitious Repository Environments: A Summary Review of Nirex Research*. Report AEAT/ERRA-0313 produced for United Kingdom Nirex Limited. Harwell, UK.
- Smart, N.R., Rance, A.P., Curlson, L., Werme, L.O., 2006. Further studies of the anaerobic corrosion of steel in bentonite, in: *Materials Research Society Symposium Proceedings*. Cambridge University Press, pp. 813–820. <https://doi.org/10.1557/proc-932-32.1>
- Smart, N.R., 2009. Corrosion behavior of carbon steel radioactive waste packages: A summary review of Swedish and U.K. Research. *Corrosion*. <https://doi.org/10.5006/1.3319128>
- Smart, N.R., Reddy, B., Rance, A.P., Nixon, D.J., Diomidis, N., 2017a. The anaerobic corrosion of carbon steel in saturated compacted bentonite in the Swiss repository concept. *Corros. Eng. Sci. Technol.* 52, 113–126. <https://doi.org/10.1080/1478422X.2017.1316088>
- Smart, N.R., Rance, A.P., Nixon, D.J., Fennell, P.A.H., Reddy, B., Kursten, B., 2017b. Summary of studies on the anaerobic corrosion of carbon steel in alkaline media in support of the Belgian supercontainer concept. *Corrosion Engineering, Science and Technology* 52:sup1, 217–226.
- Swanton, S.W., Baston, G.M.N., Smart N.R., 2015. Carbon-14 Source Term CAST – Rates of steel corrosion and carbon-14 release from irradiated steels – state of the art review (D2.1).

- Tanger, J.C., Helgeson, H.C., 1988. Calculation of the thermodynamic and transport properties of aqueous species at high pressures and temperatures; revised equations of state for the standard partial molal properties of ions and electrolytes. *Am. J. Sci.* 288, 19–98. <https://doi.org/10.2475/ajs.288.1.19>
- Taniguchi, N., Kawasaki, M., Naito, M., 2010. Corrosion Behavior of Carbon Steel in Compacted Bentonite Saturated with Simulated Groundwater under Anaerobic Condition. *Zairyo-to-Kankyo* 59, 418–429. <https://doi.org/10.3323/jcorr.59.418>
- Thoenen, T., Hummel, W., Berner, U.R., Curti, E., 2014. The PSI/Nagra Chemical Thermodynamic Database 12 / 07 417. PSI Report Nr. 14-04, Paul Scherrer Institut, Villigen PSI, Switzerland.
- Tits, J., Fujita, T., Harfouche, M., Dähn, R., Tsukamoto, M., Wieland, E., 2014. Radionuclide uptake by calcium silicate hydrates: Case studies with Th(IV) and U(VI). *Nucl. Energy Saf. Res. Dep. Lab. Waste Manag.*
- Tits, J., Stumpf, T., Rabung, T., Wieland, E., Fanghänel, T., 2003. Uptake of Cm(III) and Eu(III) by calcium silicate hydrates: A solution chemistry and time-resolved laser fluorescence spectroscopy study. *Environ. Sci. Technol.* 37, 3568–3573. <https://doi.org/10.1021/es030020b>
- Tremosa, J., Arcos, D., Matray, J.M., Bensenouci, F., Gaucher, E.C., Tournassat, C., Hadi, J., 2012. Geochemical characterization and modelling of the Toarcian/Domerian porewater at the Tournemire underground research laboratory. *Appl. Geochem.* 27, 1417–1431.
- Truche, L., Berger, G., Destigneville, C., Guillaume, D., Giffaut, E., 2010. Kinetics of pyrite to pyrrhotite reduction by hydrogen in calcite buffered solutions between 90 and 180°C: Implications for nuclear waste disposal. *Geochim. Cosmochim. Acta* 74, 2894–2914. <https://doi.org/10.1016/j.gca.2010.02.027>
- Truche, L., Berger, G., Destigneville, C., Pages, A., Guillaume, D., Giffaut, E., Jacquot, E., 2009. Experimental reduction of aqueous sulphate by hydrogen under hydrothermal conditions: Implication for the nuclear waste storage. *Geochim. Cosmochim. Acta* 73, 4824–4835. <https://doi.org/10.1016/j.gca.2009.05.043>
- Truche, L., Jodin-Caumon, M.C., Lerouge, C., Berger, G., Mosser-Ruck, R., Giffaut, E., Michau, N., 2013. Sulphide mineral reactions in clay-rich rock induced by high hydrogen pressure. Application to disturbed or natural settings up to 250°C and 30bar. *Chem. Geol.* 351, 217–228. <https://doi.org/10.1016/j.chemgeo.2013.05.025>
- van der Lee, J., De Windt, L., Lagneau, Goblet, P., 2003. Module-oriented modeling of reactive transport with HYTEC. *Computers and Geosciences* 29, 265–275.
- Van Loon, L. R., Müller, W., Iijima, K., 2005. Activation energies of the self-diffusion of HTO, <sup>22</sup>Na<sup>+</sup> and <sup>36</sup>Cl<sup>-</sup> in a highly compacted argillaceous rock (Opalinus Clay). *Applied Geochemistry* 20, 961–972.
- Vespa, M., Wieland, E., Dähn, R., Lothenbach, B., 2015. Identification of the Thermodynamically Stable Fe-Containing Phase in Aged Cement Pastes. *J. Am. Ceram. Soc.* 98, 2286–2294. <https://doi.org/10.1111/jace.13542>
- Wagman, D.D., Evans, W.H., Parker, V.B., Schumm, R.H., Halow, I., Bailey, S.M., Churney, K.L., Nuttall, R.L., 1982. The NBS Tables of Chemical Thermodynamic Properties. *J. Phys. Chem. Ref. Data.*
- Wagner, T., Kulik, D.A., Hingerl, F.F., Dmytrievava, S. V., 2012. Gem-selektor geochemical modeling package: TSolMod library and data interface for multicomponent phase models. *Can. Mineral.* <https://doi.org/10.3749/canmin.50.5.1173>
- Walker, C.S., Sutou, S., Oda, C., Mihara, M., Honda, A., 2016. Calcium silicate hydrate (C-S-H) gel solubility data and a discrete solid phase model at 25 °C based on two binary non-ideal solid solutions. *Cem. Concr. Res.* 79, 1–30. <https://doi.org/10.1016/J.CEMCONRES.2015.07.006>

- Weetjens, E., Marivoet J., Govaerts, J., 2012. Preparatory Safety Assessment. Report SCK•CEN-ER-215, SCK-CEN, Belgium.
- Wittebroodt, C., Savoye, S., Frasca, B., Gouze, P., Michelot, J.L., 2012. Diffusion of HTO, <sup>36</sup>Cl<sup>-</sup> and <sup>125</sup>I<sup>-</sup> in Upper Toarcian argillite samples from Tournemire: effects of initial iodide concentration and ionic strength. *Appl. Geochem.* 27, 1432–1441.
- Yu, L., Weetjens, E., 2012. Estimation of the gas source term for spent fuel, vitrified high-level waste, compacted waste and MOSAIK waste. Report SCK•CEN-ER-162, SCK-CEN, Belgium.
- Zhao, Y., Jin, W., 2016. Steel Corrosion in Concrete, in: *Steel Corrosion-Induced Concrete Cracking*. Elsevier, pp. 19–29. <https://doi.org/10.1016/b978-0-12-809197-5.00002-5>